Aerodynamic Drag on Deformable and Active Structures in High Reynolds Number Conditions

by

Mark Andrew Guttag

Submitted to the Department of Mechanical Engineering
in partial fulfillment of the requirements for the degree of

Doctor of Philosophy

at the

MASSACHUSETTS INSTITUTE OF TECHNOLOGY

February 2018

© Massachusetts Institute of Technology 2018. All rights reserved.

Signature redacted

Author .....
Department of Mechanical Engineering
December 31, 2017

Signature redacted

Certified by .....
Pedro M. Reis
Professor of Mechanical Engineering École Polytechnique Fédérale de Lausanne (EPFL), Switzerland and Visiting Associate Professor of Civil and Environmental Engineering, Massachusetts Institute of Technology
Thesis Supervisor

Signature redacted

Accepted by .....
Rohan Abeyaratne
Chairman, Committee on Graduate Students

ARCHIVES
MASSACHUSETTS INSTITUTE OF TECHNOLOGY
FEB 09 2018
LIBRARIES

Aerodynamic Drag on Deformable and Active Structures in High Reynolds Number Conditions

by

Mark Andrew Guttag

Submitted to the Department of Mechanical Engineering
on December 31, 2017, in partial fulfillment of the
requirements for the degree of
Doctor of Philosophy

Abstract

We explore the effect of topography on the aerodynamic behavior of deformable structures, at high Reynolds numbers. We first introduce a novel mechanism to control the aerodynamic drag on cylinders, in the critical Reynolds number regime. We created both axially grooved and dimpled specimens, comprised of latex membranes stretched over rigid acrylic skeletons. By decreasing the internal pressure of the specimens, the latex stretched inward thus changing the shape of the surface. Using a combination of finite element simulations and precision mechanical experiments, we characterized the relationship between the mechanical deformation in the membrane and pneumatic loading. Wind tunnel experiments were used to explore how changing several geometric parameters, of both grooved and dimpled cylinders, affected the aerodynamic performance. We also used the tunable nature of the specimens to automatically control the dependence of the drag coefficient on the Reynolds number. Additionally, we studied the effect of holes in thin flexible strips at high Reynolds numbers. In this investigation, instead of controlling the deformation of the specimens, we modified the initial geometry by cutting holes in strips and examined the deformation under uniform aerodynamic loading. We used a combined experimental and numerical approach to study the effect of perforation on the drag coefficient. The work presented in this thesis, represents an important first step towards utilizing deformation to control the aerodynamic performance of structures.

Thesis Supervisor: Pedro M. Reis
Title: Professor of Mechanical Engineering École Polytechnique Fédérale de Lausanne (EPFL), Switzerland and Visiting Associate Professor of Civil and Environmental Engineering, Massachusetts Institute of Technology

Acknowledgments

The work completed in this thesis could not have been completed alone, and I had a tremendous amount of help and support from a number of people.

First, I would like to thank my adviser, Pedro Reis. At points early on in my PhD it seemed like nothing was going right, but your constant encouragement and guidance allowed me to push on and complete this work. You have been an amazing adviser and friend, and are always a pleasure to work with.

Second, I would like to thank Mary Boyce who was my adviser for my masters. Mary, from the moment I set foot on MIT's campus you made me feel like this was the right place for me. You helped me realized how much fun academic research could be and led me to become a better scientist and engineer.

I would also like to thank the other members of my committee; Mark Drela, Peko Hosoi and Xuanhe Zhao. Since our first committee meeting, your feedback has been invaluable and integral to the completion of this work.

Many members of the EGS.Lab provided help at various stages of this work. In particular, the work presented in Chapter 5 was done in close collaboration with Hussain Karimi and Claudio Falcón.

Finally, I would like to thank my family; Mom, Dad, Addie, Michael, Andrea and David. My entire life you have all pushed me to be the best I can be in every endeavor. I feel incredibly blessed to have you all in my life, and I know that you are all there for me when I need you.

I especially want to thank my Mom and Dad for everything you've done to get me to this stage in my life. Your passion for education is the reason that I pursued a PhD. Mom, without you pushing me to join the Science Olympiad team in high school I might have never become an engineer. And Dad, I feel incredibly lucky to have had you as an extra adviser at MIT, and I always value your sage advice.

THIS PAGE INTENTIONALLY LEFT BLANK

Contents

1 Introduction and Literature Review **9**

1.1 Aerodynamic drag on bluff bodies 12

1.2 Drag reduction strategies 17

1.3 The effect of dimples on drag 22

1.4 Drag on grooved cylinders 25

1.5 Flexible structures 29

1.6 Effect of Porosity in Rigid Structures 33

1.7 Outline of Thesis 34

2 Aerodynamic drag on deformable grooved cylinders **37**

2.1 Motivation 38

2.2 Wind tunnel experimental setup and sample fabrication 41

2.3 Material characterization of the latex 44

2.4 Mechanics of deformation of the surface 48

2.5 Aerodynamic drag characterization with wind tunnel experiments . . 51

2.6 Conclusion 59

3 Aerodynamic drag on deformable dimpled cylinders: a parameter study **61**

3.1 Motivation 62

3.2 Design, fabrication and assemblage of the experimental specimens . . 63

3.3 Mechanics of deformation of the dimples during pneumatic actuation 66

3.4 Wind tunnel experiments on fixed dimpled specimens 71

3.5 Conclusions 90

4 Programmable aerodynamic drag control on dimpled cylinders 93

4.1 Minimizing drag by actively changing the dimple depth 94

4.2 Programmable drag by actively changing the dimple depth 96

4.3 Limitations on the active control mechanism 100

4.4 Conclusions 103

5 Aeroelastic deformation of a perforated strip 105

5.1 Introduction 106

5.2 Procedure of wind tunnel experiments to test perforated flexible strips 107

5.3 Details of the numerical model 111

5.4 Validation of the numerical model against experiments 116

5.5 Design and characterization of the strips 119

5.6 Drag coefficient of the perforated elastic strips 124

5.7 Results of experiments in the vertical configuration 128

5.8 Discussion of results 131

5.9 Conclusion 133

6 Conclusion 135

6.1 Summary of Findings 135

6.2 Limitations and Future Work 138

6.3 Final Remarks 140

Chapter 1

Introduction and Literature Review

Any solid structure placed into a moving fluid (or a structure moving through a stationary fluid) will experience forces exerted by the fluid. If the fluid is air (or another gas) these forces are known as aerodynamic forces, and are typically decomposed into two main components: lift and drag. Lift forces are perpendicular to the direction of relative motion, whereas drag forces are in the direction of fluid motion.

This thesis will focus on aerodynamic drag forces. Specifically, we will present results of experimental and numerical work performed to measure the effect of varying the geometry of bodies, either actively or passively, on the drag force. We utilize cylindrical bodies with variable surface shapes to modify the drag, and use this mechanism to actively control the aerodynamic performance. Additionally, we study the effect of adding porosity to flexible structures on their drag coefficient.

Depending on the context, aerodynamic forces can be either beneficial or detrimental, and play an important role in nature and many engineering applications. In nature, plants have evolved to make use of aerodynamic forces for different purposes. While some plants rely on insects and birds to drive the pollination process, a multitude of other plants make use of wind pollination, also known as anemophily, to distribute pollen [1, 2, 3, 4]. In anemophilous plants, pollen can be carried up to 100 km by the wind before pollination occurs [5]. To make efficient use of the wind to

distribute their seeds, anemophilous plants tend to have small pollen grains ($20 - 60$ microns in diameter) which can be easily carried by the wind [4]. The pollen grains of many anemophiles, have air filled cavities to increase the buoyancy and thus improve the efficiency of pollen distribution [6].

In addition to its contributions to the reproductive process, the wind also plays an important role in the growth of plants. Despite the Reynolds number on a leaf being relatively low (generally $Re \leq 10^4$), the boundary layer at the surface of leaves is generally turbulent throughout [7]. The turbulent boundary layer enhances the gaseous exchanges through the surface of the leaves necessary for photosynthesis to occur [8]. In addition to this direct influence, the wind can also indirectly influence the photosynthetic cycle [9, 10]. The motion caused by wind affects the amount of light that reaches the leaves inside of the canopy, which is a critical factor in photosynthesis [9, 10].

While aerodynamic forces may benefit plants in their reproduction and growth, the wind can also have detrimental effects on plants. The lateral drag forces induced by high winds can be large and potentially damaging to plants. In order to resist these side forces and prevent harm, plants have evolved different mechanisms including massive trunks [11], expansive root systems [11], complex surface textures [12] and even the ability to reconfigure their shape [13].

While evolution occurs over generations, on a shorter time scale the forces exerted on plants by the wind can affect the growth of individual plants. The response of plants to mechanical loading is known as thigmomorphogenesis [8]. A mechanically stimulated plant will grow a shorter and stockier stem, compared to one that has not been stimulated [14]. This effect was studied in tomato plants, where it was found that the entire plant would stop growing in response to local strains in the stem [15]. Like momentary stimulation, exposure to regular loading throughout their lifetime can also effect plants. For example, the branches of trees exposed steady to winds are thicker than those that are not [16].

Just as in plants, animals have evolved to make use of aerodynamic forces. The ability to fly is necessary for many animals to survive, and the interaction between

the wings and air generates the lift forces required to sustain flight. The mechanics of flapping flight have been studied extensively [17,18,19]. Small animals can fly over a range of speeds and are capable of hovering, whereas large birds usually only fly at a narrow range of speeds and require space for takeoff [20]. For winged flight, higher speeds generally produce more lift, thus it is thought that larger birds are incapable of hovering or flying at very low speeds, because of the higher lift forces required to counteract gravitational forces [20].

As in nature, aerodynamic forces can be helpful or harmful in man-made applications. The canonical example of an application that harnesses aerodynamic forces is airplanes. At sufficiently high speed, the flow over the wings produces lift forces equal to the weight of the plane, allowing it to fly. To reduce their speed for landing, airplanes utilize air brakes that increase drag. Similarly to air brakes, parachutes harness drag forces to reduce speed [21].

In cars, aerodynamic forces also play an important role. Drag forces exerted on a moving vehicle cause a reduction in fuel efficiency, and lift forces oriented upward degrade their maneuverability [22,23]. When lift forces are oriented downward, vehicle performance can be increased by improving tire adhesion [24]. This mechanism is exploited in race cars through the addition of structural features like small wings, or by modifying the geometry of the vehicle body [24].

While aerial and ground vehicles generally use their own motion to generate aerodynamic forces, wind loading on stationary structures must often be accounted for during the design process. For example, the primary concern in the design of a bridge is the ability to withstand heavy vertical loads without collapsing. However, if the wind force is not considered, catastrophic failure can occur because of wind induced self-excitation [25]. Likewise, the designs of modern skyscrapers must also account for aerodynamic forces. For example, in the design of the Burj Khalifa (the tallest building in the world at the time of writing), complex modeling and experimentation was done to help inform the final shape of the building to minimize the detrimental effects of wind on the building [26,27]. Ultimately, through a combination of aerodynamic and structural design, on a windy day the top floor of the 828 m tall building

only sways about 1.5 m [28].

The research presented in this thesis is inspired by observations from both natural and man-made products. For example, inspired by the Saguaro cactus, we will investigate the drag forces on longitudinally grooved cylinders (Chapter 2). We shall design and fabricate specimens with tunable topography to study the effect of different groove geometries. Inspired by the drag reduction caused by dimples on golf balls, we study the effect of dimples on the aerodynamic performance of cylinders (Chapter 3). We will examine how modifying the depth, size and array of dimples can influence the drag on cylinders. The novel active specimens used for this work allow for the continuous transformation of the surface topography and thus a more thorough exploration of the effect of different geometries on drag. In addition, we will utilize the tunable nature of both the grooved and dimpled cylinders to control the aerodynamic performance, specifically the relationship between the drag coefficient and the Reynolds number (Chapter 2, 4). Finally, we will study the combined effect of flexibility and porosity on the drag of structures using a combined numerical and experimental approach (Chapter 5).

1.1 Aerodynamic drag on bluff bodies

There are two main contributions to the drag force on a solid object placed in a fluid flow: friction drag (sometimes referred to as skin friction) and form drag (also known as pressure drag). Friction drag arises from tangential viscous forces and form drag arises from normal pressure forces over the surface of the structure [29]. Throughout this thesis, we will focus on *bluff bodies* which have separated flow over a significant portion of the surface [30]. By contrast, *streamlined bodies* generally have attached flow on most of the surface. Flow separation is a phenomenon characterized by the boundary layer breaking away from the surface of the structure because of an adverse pressure gradient [31]. Bluff bodies are ubiquitous, and examples range from high-rise buildings [26] to automobiles [32] and even cyclists [33].

When studying the drag on objects, a parameter known as the drag coefficient is

used to quantify the magnitude of the drag force. The drag coefficient is a dimensionless number that takes into account both the friction and form drag on the object, and is defined as

$$C_{\mathrm{d}} = \frac{F_{\mathrm{d}}}{\frac{1}{2}\rho U^2 A} \tag{1.1}$$

where F_{d} is the total drag force, ρ is the density of the fluid, U is the relative velocity of the fluid and A is a reference area. Depending on the type of object, the reference area has different conventions. Typically, for bluff bodies, the frontal area (the 2D projection of the body as seen from the stream) is used [31]. The drag coefficient of an object is not a constant; it is a function of the Reynolds number, defined as

$$Re = \frac{\rho U L}{\mu} \tag{1.2}$$

where L is a characteristic length of the object, and μ is the dynamic viscosity of the fluid. For cylinders, the characteristic length is typically the diameter. Fig. 1-1 shows the drag coefficient of a smooth cylinder as a function of the Reynolds number [29, 34, 35, 36, 37, 38].

As a characteristic example, to describe the flow field around bluff bodies, we will focus on cylindrical geometries in this introductory chapter. This is also the geometry that we will work with in Chapters 2 – 4. Depending on the Reynolds number, the flow has different characteristics. For very low Reynolds number ($Re \lesssim 4$) the flow stays attached to the surface as shown in the schematic diagram of Fig. 1-2(a). In this regime, the drag is very high and is caused entirely by skin friction [39]. As the Reynolds number increases ($4 \lesssim Re \lesssim 40$) eddies form on the rear of the cylinder and remain attached to the body as shown in Fig. 1-2(b). In these relatively low Reynolds number regimes, the drag still arises primarily from skin friction [29]. Further increasing the Reynolds number ($40 \lesssim Re \lesssim 400$), the wake becomes unstable and vortices are alternately shed [29]. Initially, the vortices, known as the "von Kármán vortex street," are not steady in this regime. However, the vortices become turbulent and organized when the Reynolds number is increased [29, 40]. This regime

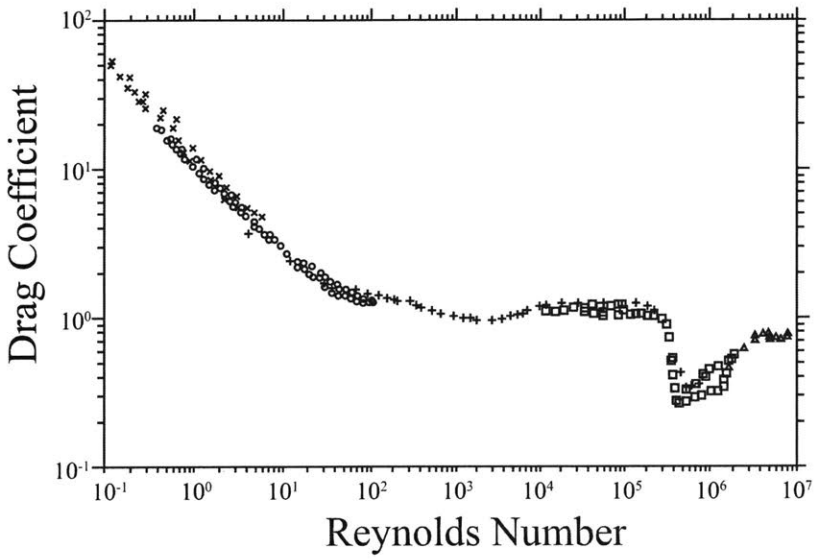


Figure 1-1: The variation of the drag coefficient of a smooth cylinder with the Reynolds number. The different symbols represent data from Wieselsberger [34], Delany and Sorenson [35], Finn [36], Tritton [37] and Roshko [38]. This figure was adapted from Panton [29].

is schematically shown in Fig. 1-2(c, d). At even higher values of Reynolds number (typically $Re \gtrsim 100$) the drag primarily consists of pressure drag, and the contribution of skin friction is small.

In the lower Reynolds number regime ($Re \lesssim 400$), the drag coefficient is a monotonically decreasing function of Reynolds number and scales as $C_\mathrm{d} \sim Re^{-1}$. However, in the range of $400 \lesssim Re \lesssim 3 \times 10^5$ the drag coefficient is nearly constant at a value of about $C_\mathrm{d} = 1.2$. As the Reynolds number is increased past $Re \approx 3 \times 10^5$, there is a steep drop, followed by a quick recovery of the drag coefficient and ultimately a plateau at very high Reynolds number. Using the nomenclature presented by Achenbach in his seminal work on rough cylinders [41], we define the regimes prior to the drop in C_d, the decrease of C_d, the increase of C_d and the plateau as the *subcritical*, *critical*, *supercritical*, and *transcritical* regimes, respectively. This dependence of C_d on Re, is known as the drag crisis, and is shown schematically in Fig. 1-3.

The drag crisis occurs only at high Reynolds numbers, and for cylinders can be observed roughly in the range $Re = 10^4 \sim 10^7$, as shown in Fig. 1-1. In the

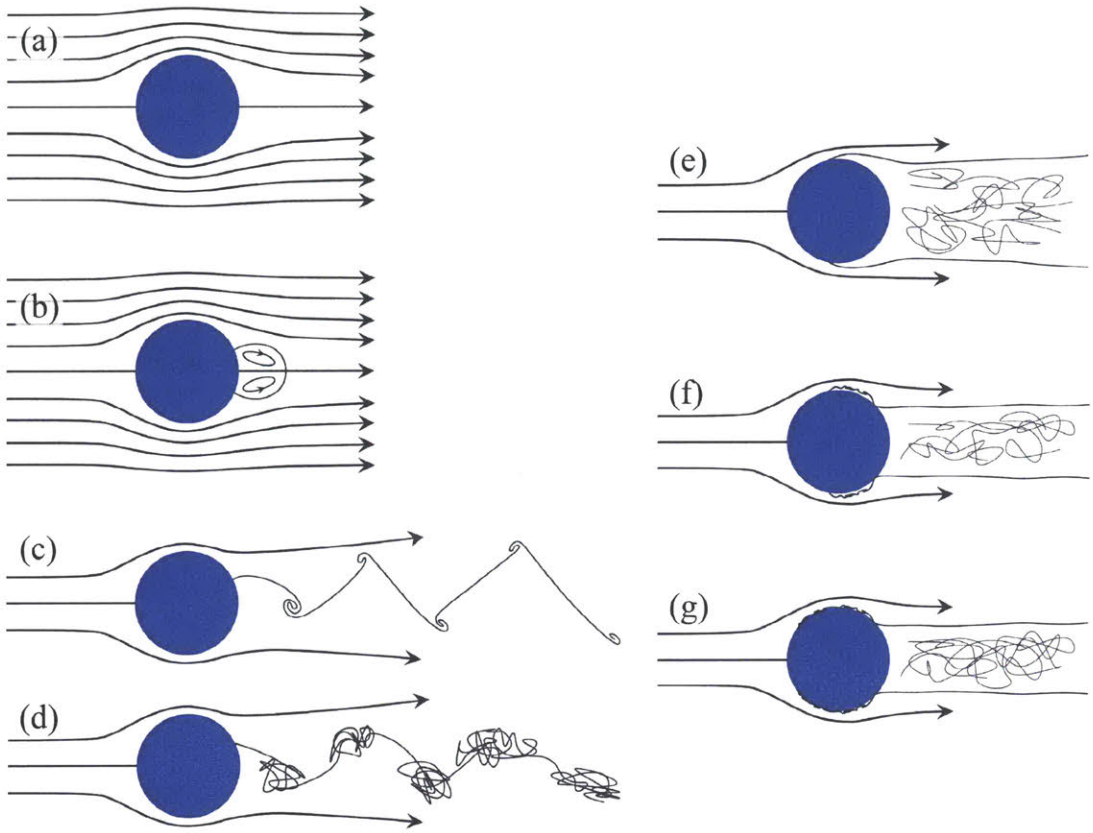


Figure 1-2: Schematic diagrams of the flow around a cylinder in different Reynolds number Regimes. (a) $Re \lesssim 4$: fully attached flow. (b) $4 \lesssim Re \lesssim 40$: attached eddies on the rear of the cylinder. (c, d) $40 \lesssim Re \lesssim 400$ alternating vortex shedding of initially non-turbulent vortices (c) then at higher Re the vortices are turbulent (d). (e) $400 \lesssim Re \lesssim 3 \times 10^5$ laminar boundary layer separation causing a large turbulent wake. (f) $3 \times 10^5 \lesssim Re \lesssim 1.5 \times 10^6$ laminar separation and turbulent reattachment delays separation. (g) $Re \gtrsim 1.5 \times 10^6$ the boundary layer transitions to turbulence before separation. The exact values of the Re of each regime can vary slightly. The values for the transitions between the various regimes were adapted from Panton [29].

subcritical regime, the flow produces a laminar boundary layer that separates on the surface of the cylinder just before the center line (at about 80° measured from the stagnation point [29, 41]). After the flow separates, it produces a large turbulent wake as shown in Fig. 1-2(e). In the critical regime, the laminar boundary layer still separates early on the cylinder, but then reattaches as a turbulent boundary layer, creating a region known as the separation bubble [41, 42]. The turbulent boundary

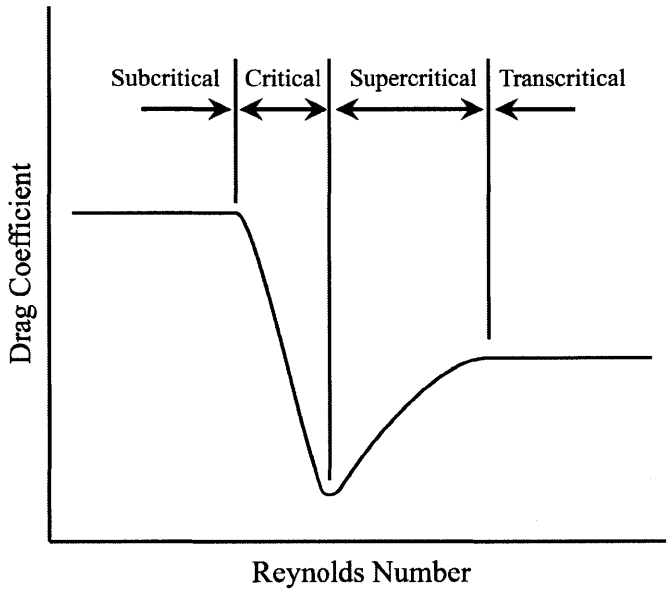


Figure 1-3: Schematic diagram of the functional dependence of the drag coefficient on the Reynolds number around the drag crisis. For cylinders, the Reynolds numbers shown here schematically fall approximately in the range $Re = 10^4 \sim 10^7$, as shown in Fig. 1-1. This figure was adapted from Achenbach [41].

layer remains attached to the surface of the cylinder for much longer, and separates around 120°, measured from the stagnation point [29]. This produces a much smaller wake region than the subcritical regime, thus causing a reduction in drag. Fig. 1-2(f) shows a schematic of this phenomenon with a greatly exaggerated separation bubble. In the supercritical regime, the boundary layer transitions directly from laminar to turbulent before the flow separates, and separation occurs on the rear of the cylinder, as shown in Fig. 1-2(g) [38, 41]. As the Reynolds number increases, the boundary layer transitions to turbulence earlier on the surface [29]. In the transcritical regime, the boundary layer is turbulent everywhere on the surface of the cylinder, except very close to the stagnation point, and the drag coefficient stabilizes [41].

In this thesis, Chapters 2, 3 and 4 focus on the drag on cylinders at Reynolds numbers around the drag crisis. In this work, we did not perform any flow visualization experiments. While we did not directly study the flow field, the underlying principles presented in this section hold. By modifying surface topography of the cylinders, we show that it is possible to manipulate the dependence of the drag coefficient on the

Reynolds number.

1.2 Drag reduction strategies

There has been considerable research on methods to modify the flow around bluff bodies. One major point of focus has been strategies to reduce the drag forces on structures [32, 41, 43, 44, 45, 46, 47]. This type of research has numerous engineering applications where drag forces are important, ranging from the automotive industry where reducing drag can improve fuel efficiency, to the sports industry where optimizing a dimple pattern can improve the performance of golf balls [48].

We will classify drag reduction strategies into two categories: *active* and *passive*. Active strategies require an input of power to the system in order to modify the drag characteristics, while passive strategies require no power input and generally rely on modifications to the initial geometry of the system.

There are many examples of active drag reduction strategies that utilize various mechanisms. They can either interact with the boundary layer on the surface of the body, or they can directly affect the wake [32]. Methods that interact with the boundary layer generally are intended to delay the separation point by enhancing the momentum of the fluid in the boundary layer [32]. In contrast, direct-wake control effects the flow field in the wake, often by directly affecting how the vortices interact [32].

One heavily studied active drag reduction strategy is the use of oscillatory motion [43, 44, 49, 50, 51]. The oscillation of cylinders is intended to alter the structure and frequency of the vortex shedding into the wake. It had been shown that for translational oscillations, vortex shedding in the wake locks in phase with the applied periodic forcing causing the vortex shedding to strengthen, thus increasing the mean drag force on cylinders [50, 51]. However, rotary oscillation has been shown to be capable of reducing drag forces [43, 44, 49]. In particular, at $Re = 15,000$, for a cylinder undergoing sinusoidal angular oscillation a drag reduction of up to 80% was observed along with a lock-in of the vortex shedding frequency with the forcing frequency [43].

Figs. 1-4(a) and (b) show flow visualization results of the wake of a stationary (a) and rotary oscillating cylinder (b), respectively [43]. The much narrower wake in the rotary oscillation leads to a significantly lower drag [43].

Other active strategies to reduce drag utilize time-periodic blowing and suction at the surface of bodies [32,45,46]. In one study, experiments were performed on a sphere with an axisymmetric slit in the surface just upwind of the separation point [45]. Using a speaker, a time periodic signal with a frequency higher than the natural shedding frequency induced alternating blowing and suction at the surface [45]. When the specimen was exposed to uniform flow in the subcritical regime ($Re = 6 \times 10^4 \sim 2 \times 10^5$), a drag reduction of nearly 50% was attained [45]. Using flow visualization techniques and surface pressure measurements, it was discovered that the drag reduction was caused by an introduction of a flow phenomenon similar to the separation bubble, which delayed the final separation [45]. The presence of the separation bubble indicates a mechanism of drag reduction very similar to the one that causes the drag crisis of a smooth cylinder described in Section 1.1 [45].

A similar strategy making use of time-periodic blowing and suction has been employed to reduce the drag on cylinders at lower Reynolds numbers ($Re = 47 \sim 3900$) [46]. In this numerical study, spatially distributed and time periodic blowing and suction was applied on the upper and lower surfaces of the cylinder as shown in Fig. 1-4(c) [32, 46]. A drag reduction of up to 25% was found at the upper range of Reynolds number explored ($Re = 3900$) [46]. This method of drag reduction directly affected the vortex shedding rather than altering the separation point. Thus it is applicable to geometries with fixed separation points, and was shown to effectively reduce the drag on a 2D model vehicle with a blunt trailing edge [32, 52].

Another active method that directly interacts with the wake in order to reduce drag, is known as base bleed [32, 47, 53, 54]. Base bleed is similar to the blowing and suction concepts presented above, however a steady flow of fluid is injected directly into the wake from the rear of the body, as shown in Fig. 1-4(d) [47]. The bleed flow interferes with the vortex formation, weakening the vortices and increases the base pressure at the rear of the body, thus decreasing the drag [32, 47]. While base bleed

does effectively reduce drag it also requires a constant input of power to produce the bleed flow.

A common passive method to reduce the drag using direct wake interaction, is known a splitter plate [32, 55, 56, 57, 58]. A splitter plate is a plate that is placed behind the body, in the center of the wake, and alters the interaction of the top and bottom shear layers. Like base bleed, splitter plates weaken the vortices and increase the base pressure at the rear of the body [32].

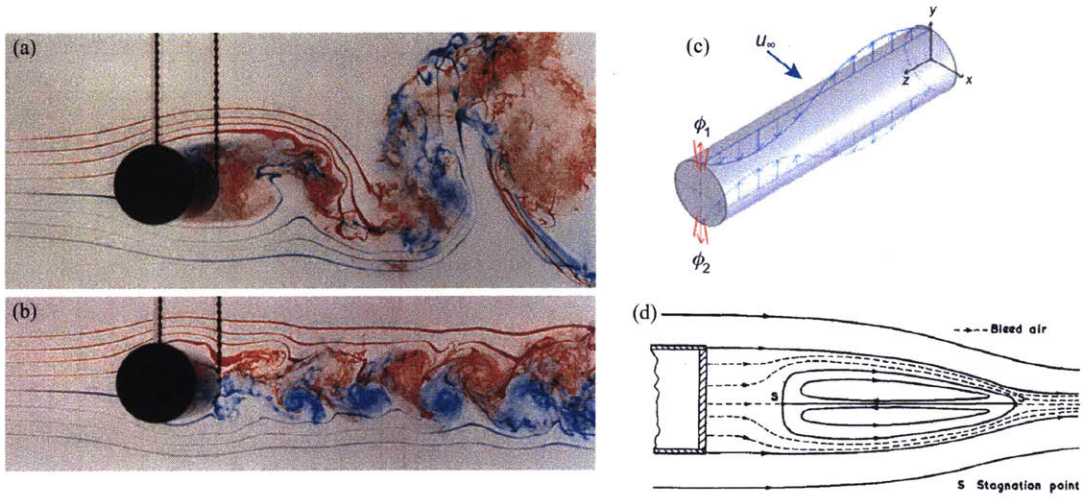


Figure 1-4: Methods of active drag reduction. (a, b) Visualization of the flow behind a cylinder without (a) and with (b) high frequency rotary oscillation [43]. Images adapted from Tokumaru and Dimotakis [43]. (c) Schematic diagram of distributed forcing using blowing and suction on the surface of a cylinder [32]. Image adapted from Choi *et al.* [32]. (d) Schematic diagram of the flow resulting from base bleed in the wake [47]. Image adapted from Bearman [47].

While splitter plates are a passive drag reduction technique that utilizes the method of direct interaction with the wake, many passive drag reduction strategies alter the boundary layer flow to delay separation. In order to delay separation, the adverse pressure gradient must be overcome by increasing the momentum in the boundary layer [32]. On bluff bodies, this can be achieved by either laminar separation and turbulent reattachment of the flow, or through direct transition of the boundary layer from laminar to turbulent before separation [32]. Recall from Section 1.1 that

both these methods occur naturally on bluff bodies around the drag crisis. The separation bubble occurs in the critical regime [41,42], and direct transition to turbulence occurs in the supercritical and transcritical regimes [38,41]. For boundary layer interactions to effectively reduce the drag, the Reynolds number must be large enough to induce a boundary layer instability, yet small enough to be below the Re at which the separation bubble naturally occurs [32]. This means that boundary layer control methods are applicable in the subcritical regime [32].

Regarding passive drag reduction strategies, surface roughness is the classic example that affects the boundary layer. The effect of surface roughness has been thoroughly studied in numerous geometries [41,59,60,61,62,63]. Achenbach, in his seminal papers on the effect of surface roughness on cylinders [41] and spheres [59], found that adding sand grains to a bluff body can significantly reduce the drag in the subcritical regime. For roughened spheres and cylinders he was able to reduce the drag by a factor of 5 [59] and 2 [41], respectively. He found that bluff bodies with surface roughness exhibit a rapid decline in the drag coefficient with increasing Reynolds number until reaching a minimum, at which point the drag quickly increases until reaching a plateau as shown in Fig. 1-5. Achenbach also showed that, by increasing the scale of surface roughness, the critical Reynolds number (i.e. the Re at which the drag coefficient was minimized) decreased and the minimum C_d increased [41,59].

Examining the local pressure and skin friction distributions on the surface of the cylinders, Achenbach determined that the steep decline in drag coefficient was accompanied by the presence of a separation bubble [41]. In the supercritical regime, the boundary layer directly transitioned from laminar to turbulent before separation occurs [41]. The similarities between the rough and smooth cylinders in both the functional dependence of C_d on Re (albeit shifted), shown in Fig. 1-5, and the flow characteristics clearly indicate that the introduction of surface roughness causes a change in the behavior of the drag crisis [41,59,60,61].

In many studies, the surface roughness was created through the adhesion of grains to the surface in an unorganized pattern [41,59,64]. However, many studies have used organized patterns on the surface to achieve drag reduction [32,65]. One such example

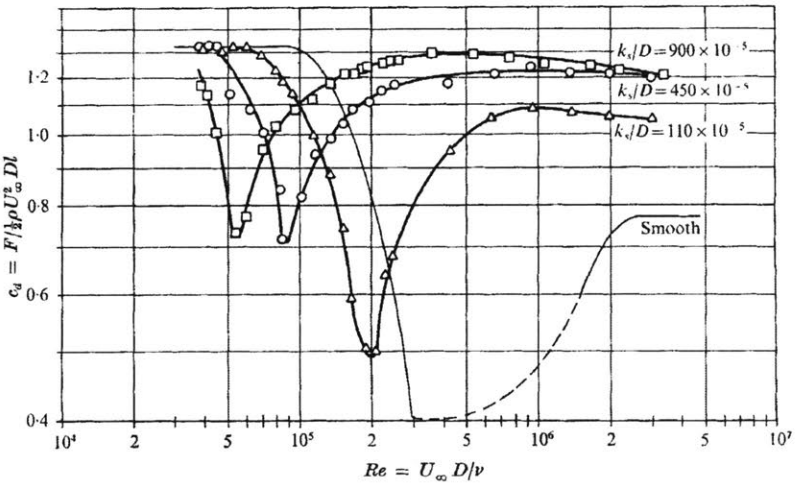


Figure 1-5: The dependence of drag coefficient on the Reynolds number for rough cylinders with different levels of roughness. Image adapted from Achenbach [41].

is the use of vortex generators [32, 65, 66]. Vortex generators are devices, with height on the order of the boundary layer thickness, placed on the surface of structures before the separation point [32]. They produce vortices in the boundary layer which increase the lateral mixing in the boundary layer thus delaying separation [32, 65, 66].

In addition to vortex generators, the drag reduction capabilities of many other organized surface modifications have been studied [48, 61, 64, 67, 68]. One study examined the difference in drag on circular cylinders with patterned surfaces and uniformly roughened surfaces [64]. They created a grid-like pattern on the surface with a roughness coefficient (*i.e.* the physical scale of the roughness) the same as that as a surface with uniform roughness and performed experiments to determine the drag coefficient [64]. They found that in the transcritical regime, the drag coefficient of the patterned surfaces was lower than that of the roughened surface [64]. This result is similar to that of many studies on dimpled bluff bodies, which is the focus of the next section.

1.3 The effect of dimples on drag

Golf balls are the canonical example of dimpled surfaces used for drag reduction. From the inception of the game of golf, there has been a desire to maximize the length a ball will travel. After the introduction of a soft remoldable ball known as the "Gutta-percha" ball in 1845, it was found that balls with marked up surfaces actually flew farther than smooth balls [48]. The first patent for the use of dimples on a golf ball was based on this observation [69]. In the years since the introduction of dimples on golf balls, there have been a significant number of studies on utilizing dimples to reduce drag or control the flow on surfaces [32, 48, 61, 67, 68, 70, 71, 72].

One early study by Bearman and Harvey [48] on the aerodynamics of golf balls, involved performing wind tunnel experiments on golf balls with a dimple depth to sphere diameter ratio of $d/D = 9 \times 10^{-3}$. They compared the results from wind tunnel tests on golf balls, to those of both smooth spheres and rough spheres [48, 59, 73]. In previous works on both smooth and uniformly roughened spheres, after the drag coefficient reached a minimum, a steep increase and subsequent plateau of C_d were observed in the supercritical and transcritical regimes [59, 73]. In golf balls it was found that the dimples induced an earlier drag crisis, and after the initial drop in C_d the steep increase in C_d generally associated with the supercritical regime did not occur [48]. Instead, after the critical regime C_d did not increase significantly and instead only increased slightly with Re as shown in Fig. 1-6a.

More recently, the mechanism for this drag reduction and subsequent nearly constant drag coefficient has been studied by Choi *et al.* [67]. They performed wind tunnel experiments on dimpled spheres with a dimple depth to sphere diameter ratio of $d/D = 4 \times 10^{-3}$, in which they studied velocity of the flow above the surface using a hot-wire probe [67]. Fig. 1-6(b) shows a schematic of the mechanism responsible for the drag reduction [67]. The flow separates at the front of the dimples, and reattaches at the back, causing a separation bubble similar to that observed in the critical regime on a smooth sphere [32, 67]. After the flow has reattached, the increased momentum in the boundary layer generated by the separation bubble delays the final separa-

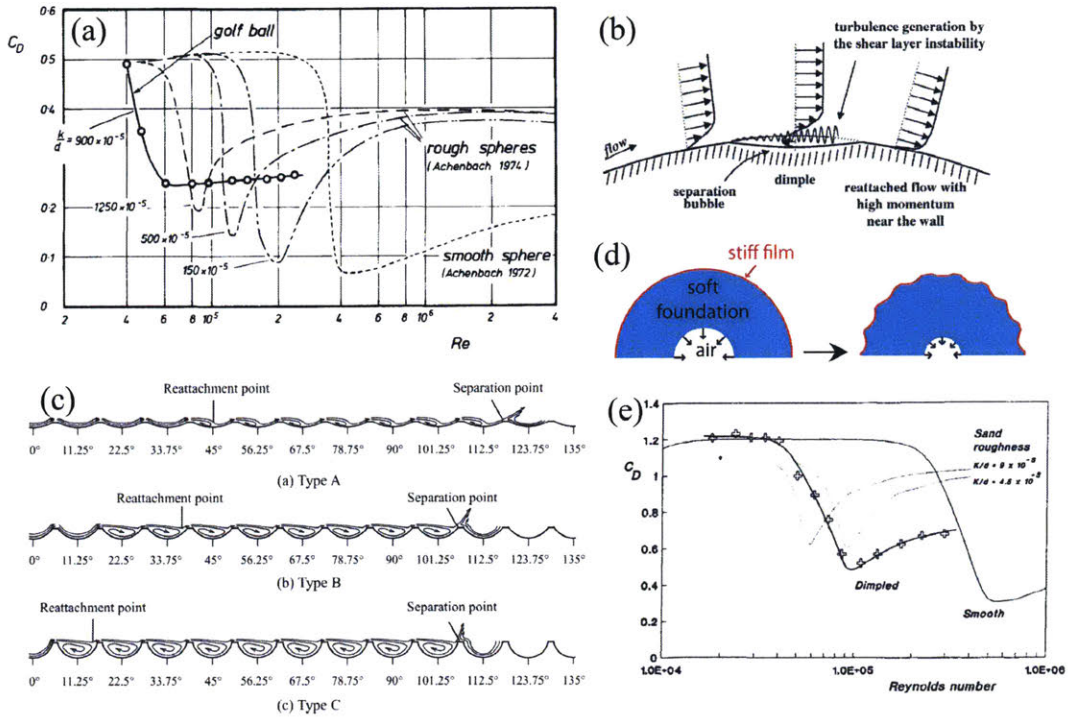


Figure 1-6: Aerodynamics of dimpled surfaces. (a) The dependence of drag coefficient on the Reynolds number for golf balls compared to smooth and uniformly roughened spheres. This figure was adapted from Bearman and Harvey [48]. (b) Schematic diagram of separation bubble formed in the dimples. This image was adapted from Choi *et al.* [67]. (c) Diagram showing the differences in the flow, particular the separation and reattachment points on dimpled spheres with different dimple depths. This image was adapted from Aoki *et al.* [74]. (d) Schematic of the wrinkling mechanism used to produce hemispherical specimens with tunable dimple depths. This image was adapted from Terwagne *et al.* [75]. (e) Comparison of the functional dependence of the drag coefficient on the Reynolds number for smooth, sand roughened and dimpled cylinders. This image was adapted from Bearman and Harvey [68].

tion point [67]. After the drop in C_d, the initial separation does not always occur at the same location (increasing the Re causes the initial separation to occur closer to the front of the body) [67]. However, in this Reynolds number regime, the flow always reattaches within the dimples and has the same final separation point [67]. The continuing presence of the separation bubbles, even after the initial drop in C_d, is different from the case of roughened surfaces. For roughened surfaces, after the

critical Reynolds number the boundary layer directly transitioned to turbulence and the drag coefficient increases significantly [41]. In the subcritical regime, the increase in momentum caused by the separation bubbles in the earlier dimples is not high enough to overcome the adverse pressure gradient and delay the main separation, thus the C_d is still high (for spheres $C_d = 0.5$) [67].

A further study, by Aoki *et al.* [74], on the mechanism for drag reduction on a dimpled sphere, examined the effect of changing the dimple depth. In this study the flow patterns were measured experimentally for dimpled spheres with various dimple depths ($d/D = \{7.9, 15.1, 18.8\} \times 10^{-3}$), and the results were compared to those of Choi *et al.* [67]. Their findings were similar to those of surface roughness: increasing the depth of the dimples caused the critical Reynolds number to decrease, and the minimum drag coefficient to increase [74]. Moreover, Aoki *et al.* [74] observed that, for each specimen, the C_d increased slightly with Re above the critical Reynolds number, and the rate of increase was higher for the deeper dimples. Just as in the previous study by Choi *et al.* [67], they observed separation bubbles forming in the dimples [74]. They discovered the deeper dimples formed separation bubbles further upstream and the reattachment point shifted to the end of the dimple, which lead to the main separation point shifting further upstream as shown in Fig. 1-6(c) [74]. The separation occurring closer to the front of the body explains the higher C_d for the specimens with deeper dimples [74].

Another study that examined the effect of the dimple depth utilized the wrinkling instability to create specimens with dimples that could change their depth [75]. Dimples were formed by depressurizing the cavity of hollow hemispherical specimens comprised of a soft foundation and a stiff outer film as shown in Fig. 1-6(d) [75]. Combining two hemispherical specimens, wind tunnel experiments were performed on a spherical body with dimples whose depths could be tuned by varying the pressure in the cavity [75]. The results from the wind tunnel tests were consistent with previous results; increasing the dimple depth induced an earlier drag crisis and a higher minimum drag coefficient [74, 75]. Therefore, at high Re a shallower dimpled specimen may have a lower C_d than a deeper dimpled one. However, at a lower Re,

the opposite may be true. As a result of this behavior there is no universal optimal dimple depth for all Reynolds numbers.

While spheres are the most commonly tested geometry with dimples, because of the direct application in golf balls, other geometries such as cylinders have also been studied [68, 76, 77]. For dimpled cylinders with dimple depth to cylinder diameter ratio $d/D = 9.1 \times 10^{-3}$ the drag crisis is again found to occur earlier than for a smooth cylinder [68]. Above the critical Reynolds number, the drag coefficient does not increase as much as for the sand roughened cylinder with similar scaled roughness, as shown in Fig. 1-6(e) [68].

In Chapter 3, we shall expand on the existing literature on the drag on circular cylinders with dimples, by systematically varying the dimple depth. Additionally, we explore the effect on the drag profile of other parameters including the radius and arrangement of dimples. This exploration is done using specimens with the ability to actively change depth, allowing us to span a wide range of dimple depths with a single specimen. In Chapter 4 we utilize the active nature of the dimples to tune the dependence of C_d on Re.

1.4 Drag on grooved cylinders

Similarly to dimples, modifying the surface of bluff bodies to include grooves can reduce drag [12, 78, 79, 80, 81, 82, 83, 84, 85]. While many of the studies on dimples were inspired by the dimples on golf balls, numerous studies using longitudinal grooves have been inspired by the Saguaro cactus (*Carnegiea gigantea*). The Saguaro cactus, shown in Fig. 1-7(a), is essentially a large cylindrical structure with axial grooves that is able to withstand high wind speeds without toppling over [86]. It has been proposed that the grooves reduce the drag forces on the cactus, and this hypothesis has lead to many subsequent studies [12, 79].

In a set of studies inspired by the Saguaro cactus, Talley *et al.* [12, 78] reported experiments that compare cylinders with different surface shapes (smooth, rough, and cactus-shaped grooves) at high Reynolds numbers ($2 \leq Re\,[\times 10^4] \leq 20$). In these

studies, specimens with v-shaped grooves were machined with a depth to cylinder diameter ratios $d/D = \{35, 70, 105\} \times 10^{-3}$. Within the tested range of Re, the grooved cylinders showed a monotonic increase in C_d with Re, until asymptoting at values in the range $1.04 \leq C_\mathrm{d} \leq 1.13$, depending on the groove depth (the deepest

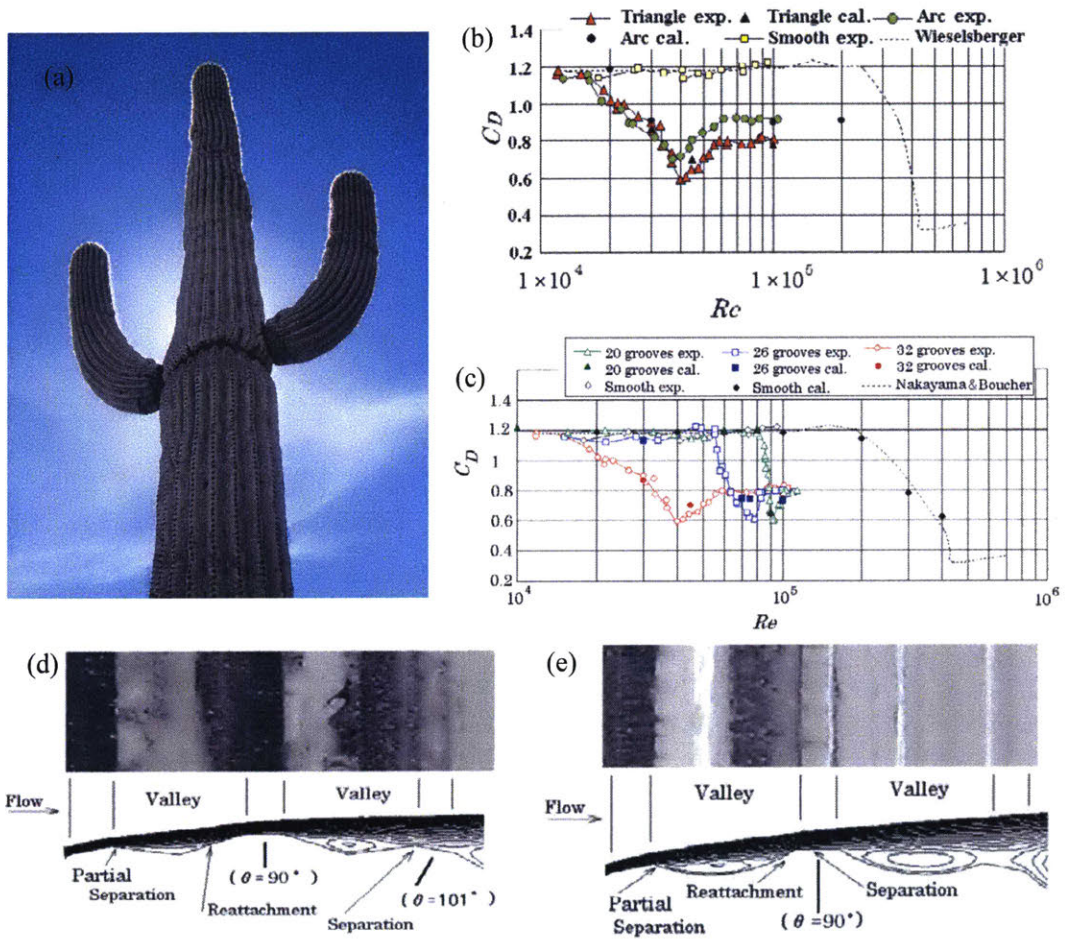


Figure 1-7: Cactus inspired aerodynamic research. (a) Representative photograph of a Saguaro cactus (Scottsdale, Arizona) [87]. (b) Comparison of the dependence of the drag coefficient on the Reynolds number for cylinders with triangular and arc-shaped grooves. This image was adapted from Yamagishi and Oki [83]. (c) Comparison of the dependence of the drag coefficient on the Reynolds number for cylinders with different numbers of grooves. This image was adapted from Yamagishi and Oki [84]. (d – e) Flow visualization using the surface oil-film technique and numerical results to determine the separation points on cylinders with triangular (d) and arc-shaped (e) grooves. These images were adapted from Yamagishi and Oki [83].

grooves providing the lowest C_d). This monotonic increase of C_d indicates that all specimens studied in these experiments were already in the supercritical and transcritical flow regimes (*i.e*, the critical Reynolds number was below the explored range of Re; $Re^* < 2 \times 10^4$) [12,78].

A subsequent experimental and numerical study by Yamagishi and Oki [83] examined the effect of the shape of grooves on C_d over a range of Reynolds numbers ($Re \approx 1 \times 10^4$ to 1×10^5). Their experiments used specimens comprised of aluminum cylinders with 32 longitudinal grooves machined into the surface. They examined both triangular and arc-shaped groove geometries with a depth to diameter ratio of $d/D = 10.4 \times 10^{-3}$ [83]. In their experiments Yamagishi and Oki found that both the triangular and arc-shaped grooves induced the drag crisis at the same Re, but the triangular-grooved cylinders exhibited a lower minimum drag coefficient and lower C_d in the supercritcal and transcritical regimes [83], as shown in Fig. 1-7(b). Combining experimental results using the oil-film technique and numerical results at $Re = 1 \times 10^5$ (both shown in Fig. 1-7(d) and (e)), they observed a separation bubble forming in the grooves similar to that found in dimples [83]. For both groove shapes, the flow reattached within the grooves, however it reattached further upstream in the triangular grooves [83]. This lead to the main separation point being farther down stream for the triangular grooves (as shown in Fig. 1-7(d) and (e)) and thus a lower C_d in the transcritical regime [83].

Another more recent study focused experiments on cylinders with catenary shaped grooves around the critical Reynolds number regime ($Re = 2 \times 10^4 \sim 1.2 \times 10^5$) [85]. In this study, experiments were performed with cylinders of varying groove geometries. Specimens were tested with groove depth to cylinder diameter ratios of $d/D = 1.7 \times 10^{-3}$ and 3.3×10^{-3} and groove width to diameter ratios of $w/D = 5.7 \times 10^{-2}$, 9×10^{-2} and 14×10^{-2} [85]. The sharpness of the grooves (i.e. how round they were) was changed by varying the shape factor in the catenary equation that defined the groove shape [85]. It was found that increasing the ratio, A^*, between the area of all the grooves and the area of the cylinder, decreased the critical Reynolds number, and increased the minimum drag coefficient [85]. This finding was robust, independently

of whether A^* was modified by changing the groove depth, groove width, or shape factor [85].

Another study, by Kimura and Tsutahara [82], examined the effect of the location and depth of a single circular arc-groove ($d/D = \{17, 12, 7\} \times 10^{-3}$). Studying the fluid flow, they found that for the deeper grooves there was recirculating flow (i.e. a separation bubble) in the grooves and a delayed separation. However for the shallowest groove, there was no recirculation detected, and the separation was only delayed slightly [82]. They also found that regardless of the the groove depth, the optimal location for the grooves to delay separation was 80° relative to the stagnation point [82].

In addition to exploring groove depth and shape, the effect of the number of grooves has also been explored [84, 85]. In a combined experimental and numerical study by Yamagishi and Oki [84], cylinders with 20, 26 and 32 triangular grooves were tested. In this study the width and depth of the grooves were fixed ($d/D = 10.4 \times 10^{-3}$ and $w/D = 7.5 \times 10^{-2}$), meaning that the spacing between the grooves was varied [84]. They found that increasing the number of grooves decreased the critical Reynolds number and made the drag crisis more gradual as shown in Fig. 1-7(c) [84]. A separate study varied the number of grooves by varying the width of the grooves ($w/D = 5.7 \times 10^{-2}$, 9×10^{-2} and 14×10^{-2}) and maintaining a constant spacing between them [85]. In this study, increasing the number of grooves was found to increase the critical Reynolds number [85].

From these existing studies, it is clear that different groove patterns effect the aerodynamic performance of cylinders. However, the parameter space explored experimentally has been limited by the cost, both fiscal and temporal, of manufacturing different grooved specimens for each configuration. Additionally, a grooved specimen has a narrow range of Reynolds number for which it has low drag, and for all other Re the C_d is higher. In Chapter 2, we will present the results of wind tunnel experiments performed using cylindrical specimens with grooved surfaces that can actively change shape. The advantage of testing active specimens is twofold. First, we are able to study a wide range of groove depths with a single specimen. Second, we will show

that it is possible to actively change the surface shape so that the drag coefficient can minimized over a range of Reynolds numbers.

1.5 Flexible structures

So far, we have focused on fixed structures that are not deformed by fluid flow. However, many flexible bodies can be readily deformed by aerodynamic or hydrodynamic loading. The class of problems relating to the interaction of deformable structures and a fluid moving relative to one another are known as fluid-structure interactions (FSI), and have been a topic of intense research [88, 89]. To name just a few representative examples, FSI is prevalent in wide ranging areas including drag reduction in fish locomotion [90], high-speed printing on paper [91], aerodynamic instability of bridges [92, 93, 94, 95, 96], energy harvesting in wind-loaded flexible structures [97, 98, 99], the modeling of parachutes [100], the waving of flags and banners [101, 102, 103] and the dynamics of wind-loaded flexible wings [104, 105, 106].

In this section, we will focus on FSI problems related to continuous flexible structures. The reconfiguration of plant leaves under wind loading is a representative and instructive example of such an FSI problem. The self-adaptation of the shape of the leaf at different flow conditions relaxes the state of stress in the plant and reduces the possibility of damage such as uprooting [107]. The effect of wind loading can be quantified by measuring the drag force, F_d, acting on the plant leaves. As presented in Section 1.1, drag forces can be written as $F_\mathrm{d} = \frac{1}{2}\rho U^2 L^2 C_\mathrm{d}$, where U is the mean speed of the flow, L is the typical length scale of the body, ρ is the density of the fluid and C_d is the drag coefficient. Generally, C_d is a function of the Reynolds number, and the functional dependence is not known *a priori*. However, as discussed in Section 1.1, for bluff bodies at moderate to high Reynolds numbers, C_d is nearly a constant, and thus the drag force scales as $F_\mathrm{d} \propto U^2$ [13].

In a series of studies on leaves and other flexible objects exposed to a steady flow [13, 108], it has been shown that the possibility of reconfiguration (as shown in Fig. 1-8(a)) can lead to drag reduction such that the exponent with which drag scales

on U is reduced from the classic quadratic behavior; *i.e.* $F_d \propto U^{2+\mathcal{V}}$ where $\mathcal{V} < 0$. This exponent is commonly referred to as the Vogel exponent. Different types of plants have been shown to be associated with different values of $\mathcal{V}$, in the range of $-1.3 < \mathcal{V} < -0.1$. The higher values of $\mathcal{V}$ occurred for tree branches, which is to be expected since they are closer to static bluff bodies [13].

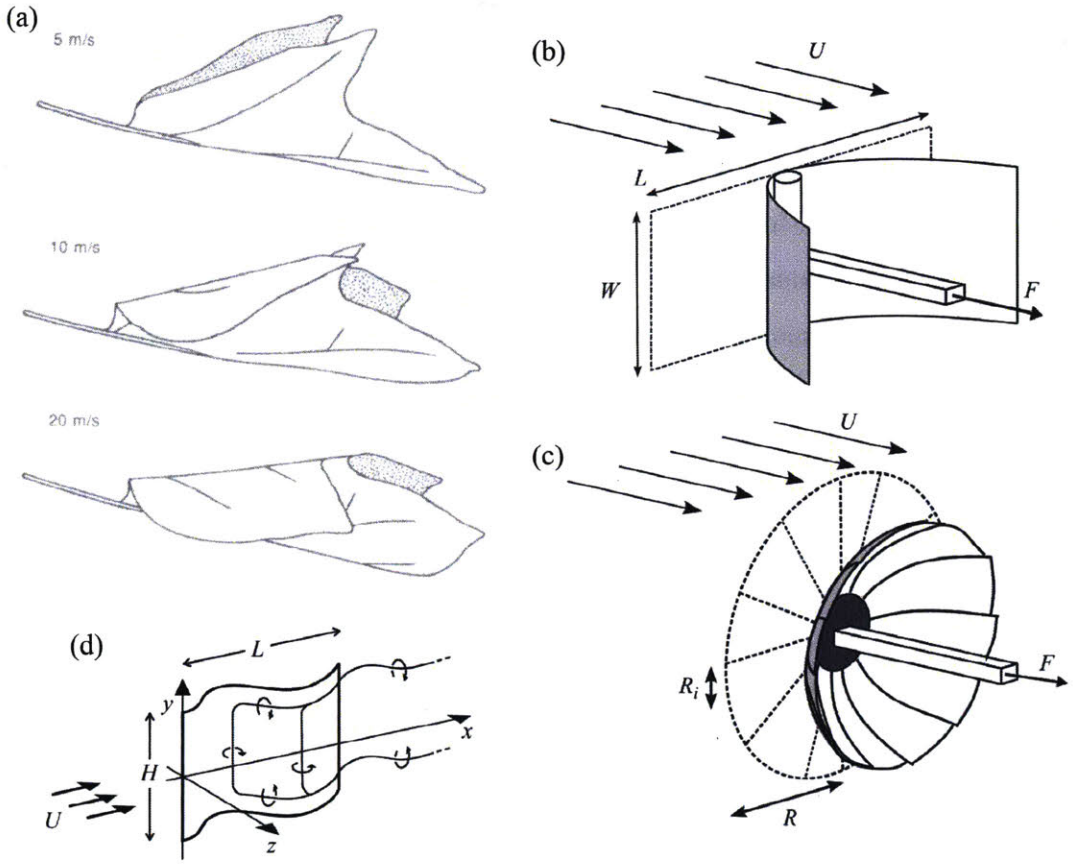


Figure 1-8: Flexible structures in flow. (a) Reconfiguration of a tulip tree leaf at different wind speeds adapted from Vogel [108]. (b and c) Schematic diagram of experiments to determined the Vogel exponent in different geometries. These images were adapted from Gosselin *et al.* [109]. (d) Schematic diagram of the flapping flag configuration commonly used to study flutter. This image was adapted from Eloy *et al.* [102].

In order to explain the appearance of Vogel exponents as a way to understand drag reduction caused by the reconfiguration of flexible bodies, several reduced mod-

els for loading configurations have been proposed. In these models the complex fluid-structure interaction that reconfigures the shape of the flexible body is modeled by a reduced loading force [110, 111, 112, 113]. Pioneering approaches to this problem first used dimensional analysis to determine the theoretical Vogel exponent for bending of flexible beams and plates, found $\mathcal{V} = -2/3$, which is in reasonably good agreement with experiments [107]. A similar argument has been used to predict $\mathcal{V}$ for flexible structures in the asymptotic regime of large deformations with respect to the typical length scale of the flexible body. Gosselin *et al.* [109] coupled a simple model with experiments to determine the relation of the Cauchy number, C_y (defined as the ratio of the force attributable to fluid loading on the plate to the bending rigidity of the plate per unit of length), to the Vogel exponent, as well as the extent of drag reduction. These experiments were performed using a wind tunnel where both rectangular specimens and disks cut in along several radii were exposed to flow at moderate to high Reynolds numbers; $6,400 \leq Re \leq 54,000$ as shown in Fig. 1-8(b) and (c). Over this extensive range, the drag coefficient remains nearly constant for rigid bluff bodies. On the other hand, flexible objects, especially in the large deformation regime, led to different Vogel exponents. The model of Gosselin *et al.* [109] showed that, for a rectangular plate, the streamlining effect on drag reduction is dominant for small deformations. For large deformations the effect of projected frontal area reduction caused by reconfiguration is more significant.

With an alternative point of departure, Alben *et al.* [114, 115] have used free-streamline theory to address the coupling between hydrodynamic loading and elastic bending on a fiber, specifically to establish how the aerodynamic drag scales with the flow velocity during reconfiguration. To explore this drag scaling, experiments were performed on a glass fiber of length L and rigidity E supported at its mid-point, while being exposed to a flowing soap film (thickness h) with uniform speed U. The underlying reduced equation for the beam curvature depended solely on one parameter, the non-dimensional speed $\eta = (\rho_f h L^3 U^2 / 2E)^{1/2}$, which can also be regarded as the ratio between the kinetic energy of the fluid and the elastic potential energy of the fiber. They found that for $\eta \ll 1$, the fiber remained nearly undeformed;

C_d was constant and the dimensionless drag force, $\tilde{F}_d$, scaled quadratically with η, $\tilde{F}_d \propto \eta^2$. For $\eta \gg 1$, the fibers took on a self-similar shape, and $\tilde{F}_d \propto \eta^{4/3}$ [114]. This means that no reconfiguration is displayed by the flexible beam when $\eta \ll 1$, and thus $\mathcal{V} = 0$, whereas the $\eta \gg 1$ case leads to a Vogel exponent of $\mathcal{V} = -2/3$, as shown by this coupled elastohydrodynamic system.

A third, and arguably more standard, approach to generate a reduced model to describe the aeroelastic coupling is to explicitly include the reconfiguration effect on the normal loading pressure by dividing it into two terms. The first term is the local drag force acting in the same way as the drag acting on a perpendicular plate. The second term arises from the local acceleration of the flow on the deformed flexible body. This idea was first presented by Lighthill [113]. The details of this model will be explained in Chapter 5. The combined action of these loading terms were applied recently for the deformation of flexible elastic sheets exposed to a uniform air flow by Buchak *et al.* [110]. In their study, sheets were laid flat and clamped on the downwind end of a wind tunnel. The air flow then caused the sheets to lift, bend and accumulate, such that the bunch of sheets eventually arrives to a steady state supported by the fluid loading. The model was used to successfully compute the shape of the sheets, using the drag coefficient as the only fitting parameter for a large range of wind speeds.

So far, we have only presented work on static, or quasi-static flexible structures. However, a common area of study in FSI problems relates to the fluttering of flexible structures exposed to uniform flow [91, 101, 102, 103, 111, 112, 116, 117]. One of the canonical examples of this type of problem is the flapping of a flag exposed to wind [101, 102, 103, 117]. Fig. 1-8(d) shows a schematic diagram of the flapping flag geometry [102]. At low wind speeds the flag remains in what is known as the stretched state, where it is straight and aligned with the flow [117]. As the wind speed increases there is a critical velocity at which the flag spontaneously starts to flap with a steady frequency [103, 118]. At higher wind speeds the flag begins to start flapping irregularly [117]. The flapping occurs because of the destabilizing pressure forces from the wind and the stabilizing bending stiffness of the flag [101, 112, 116].

There has been a large body of work studying the spontaneous transition from the stretched state to the steady flapping state [91, 101, 102, 117, 118]. Above the critical velocity, the amplitude of the stable flapping increases with velocity [102]. A hysteresis has been observed, allowing steady flapping to persist even below the critical velocity if flapping has been initiated [102]. Additionally the mass and length of the plates can affect the critical wind speed [101, 102].

In Chapter 5 we present a combined numerical and experimental study on flexible strips deformed by the wind. We perform wind tunnel experiments on flexible porous strips where we measure the wind speed and quantify the deformation in the strips. We will use the reduced loading model used by Buchak *et al.* [110] to determine the drag coefficient based on the results of the experiments. Additionally we will explore the effect of the Cauchy number on the drag coefficient.

1.6 Effect of Porosity in Rigid Structures

We commented above on how the flexibility of a structure can have a strong effect on the aerodynamic drag that it experiences (because of reconfiguration). The porosity, ϕ, defined for a slender perforated plate as the fraction of material replaced by voids, can also have a strong effect on the aerodynamic drag. In the limit of large Re, the effect of porosity has often been studied in relation to screens, which cause a reduction in pressure when used to obstruct flow [119]. Many investigations [119, 120, 121, 122, 123, 124, 125, 126, 127] have been done with both experimental measurements and theoretical modeling to examine the dependence of the drag coefficient on the pressure loss coefficient, K, rather than directly on ϕ. The pressure loss coefficient, when the incident flow is normal to the screen, has been typically defined as $K = \Delta p/(\frac{1}{2}\rho_a U^2)$, where Δp is the pressure difference across the screen. The value of K is known to be a function of ϕ, Re and the Mach number M [119]. However, at large Re and low M, the pressure loss coefficient becomes only a function of ϕ, with past studies [125, 127] proposing the relation $K \sim (1-\phi)/\phi^2$, where the proportionality constant is of order 1 [119, 126, 127].

Taylor [126] was one of the pioneers in describing the effect of porosity on the drag of a perforated screen. His modeling strategy was to replace the screen by a uniformly spaced array of sources. The flow field produced by combining the free stream flow with the one generated by the resistance sources yielded a prediction for the drag coefficient of the screen as a function of the pressure loss coefficient [127]. This method proved to be reasonably accurate for small values of K (large values of ϕ) where C_{d} decays to 0 with K, but failed at high values of K (low values of ϕ) where it predicted that C_{d} would decrease with increasing K. At high values of K, C_{d} should attain a constant value (the drag coefficient of the continuous sheet). In work by Koo and James [123], a refinement of this prediction adapted the previous model to determine C_{d} as a function of K, which produced a saturation of C_{d} up to a constant value with increasing K [123]. These predictions have been tested experimentally in several studies. Blockley [120] measured the pressure loss and drag coefficients of perforated plates as a function of porosity and found reasonably good agreement with the theoretical results, especially for large porosity. Later, Castro [121] reported experimental results on perforated plates and measurements on the corresponding drag coefficients, using both the wake traverse method and a drag balance method. A similarly good agreement was found with the predictions of Koo and James [123] and experimental results of Blockley [120] for high porosity, but found a worse agreement for low porosity.

All the studies presented in this section, have focused on the effect of porosity for rigid structures in a flow. However, very little work has been done on flexible porous structures. In Chapter 5, we will study how introducing porosity effects the drag coefficient of flexible strips. We will compare the results of our study on flexible perforated strips to those of the rigid porous plates presented in this section.

1.7 Outline of Thesis

This chapter introduced the fundamental principles leading to drag forces, particularly on bluff bodies, along with a literature review of the current state of research.

In subsequent chapters, we present a collection of results derived using a joint experimental and numerical approach to learn more about how modifications in morphology can effect the aerodynamic drag on structures. We harness the deformable nature of elastic membranes to develop cylindrical specimens whose surface topography can be controlled through pneumatic actuation. These structures are used to study how modifying different geometric parameters affects the aerodynamic drag. We also show, that by actively tuning the shape of the specimens, we can control the drag coefficient as the Reynolds number changes. Additionally, we study the effect of porosity on drag in a system where the forces from the fluid flow induce deformation of flexible perforated strips.

In Chapter 2, we study the effect of grooves on the aerodynamic performance of cylinders at high Reynolds numbers. We use specimens comprised of a rigid skeleton and a flexible membrane. We modify the groove depth using pneumatic control. Using both experiments and simulations, we characterize the relationship between the internal pressure and the groove depth. We then use wind tunnel experiments to develop an understanding of the functional dependence of the drag coefficient on the Reynolds number with various groove depths. Using active specimens, we demonstrate the ability to achieve a monotonically decreasing C_{d} in the critical Reynolds number regime. This is in stark contrast to static grooved specimens, that first exhibit a decrease and then an increase of C_{d}.

In Chapter 3, we expand on the results from Chapter 2, by utilizing specimens with a 3D array of dimples rather than longitudinal grooves. Using similarly constructed specimens with a rigid skeleton and flexible membrane, we study the effect on aerodynamic performance of dimpled cylindrical specimens with various surface topographies. In particular, we perform wind tunnel experiments on specimens with dimples of various diameters and depths arranged in different configurations.

Using the results of Chapter 3, we are able to determine how the dimple depth, effects the dependence of the drag coefficient on the Reynolds number. We use this knowledge in Chapter 4, to demonstrate that the drag coefficient can be controlled by actively modifying the depth of the dimples. Much like the grooved case, we show

that we can achieve a monotonically decreasing C_{d}. Additionally we show that, in the high Reynolds number regime, the functional dependence of C_{d} on Re can be programmed to achieve other effects.

We then move on to study a system in which the aerodynamic forces lead to significant deformation of structures. In Chapter 5, we use a joint numerical and experimental approach to study the effect of porosity on the drag of flexible perforated strips. We use a reduced loading model to determine the drag coefficient of the strips and compare those results to rigid porous plates.

Finally, in Chapter 6, we summarize the key methods and findings of this work. We conclude with a discussion of some limitations of the research presented in this thesis, and suggestions for future work.

Chapter 2

Aerodynamic drag on deformable grooved cylinders

In this chapter, we study a mechanism for active aerodynamic drag reduction on morphable grooved cylinders, whose topography can be modified pneumatically. First, we characterize the relationship between groove depth and pneumatic loading. Secondly, wind tunnel tests are used to measure the aerodynamic drag coefficient (as a function of Reynolds number) of the grooved samples, with different levels of periodicity and groove depths. Finally, we leverage the morphable nature of our system to dynamically reduce drag for varying aerodynamic loading conditions.

This chapter is organized as follows. In Section 2.2, we describe our experimental apparatus used to measure the drag forces on the cylindrical samples, and detail the sample fabrication method. Section 2.3 discusses the mechanical behavior of the latex material used for the flexible film in the specimens. In Section 2.4, we describe the finite element simulations and physical experiments used to study the mechanics of deformation of the outer elastomeric film, and establish a relationship between the groove depth and the internal pressure in the specimens. Next, the protocol of the wind tunnel experiments is presented in Section 2.5.1. Finally, the results of the aerodynamic experiments are presented in Sections 2.5.2 and 2.5.3.

2.1 Motivation

The *Carnegiea gigantea*, commonly known as the Saguaro cactus (Fig. 2-1), is an iconic and endemic plant to the Sonoran desert in the American southwest. These cacti can grow to be 15 m tall with diameters over 0.8 m and weigh over 1800 kg [128, 129]. Despite their shallow root base, these essentially cylindrical plants are able to withstand wind speeds of up to $38\,\mathrm{ms}^{-1}$ without toppling over, and can live as long as 150 years [86]. The surface morphology of a mature Saguaro cactus comprises between 10 and 30 vertical (axial) grooves that are equally spaced around its circumference [128]. The depth of these grooves varies along the trunk [12], and their shape also changes with the seasons [128]. During the wet season, the trunk undergoes hygroscopic swelling and the grooves are less pronounced. In reverse, during the dry season, the stored water is gradually consumed and the grooves deepen [128]. For a 1.5 m tall cactus, the ratio between groove depth and plant diameter has been measured to be approximately 0.07 [130]. A possible evolutionary advantage of the grooves is that they may provide additional structural support to the plant. Another prevailing hypothesis in the literature [12, 79] is that the axial corrugations are thought to yield an aerodynamic advantage that reduces the overall form drag on the structure. This drag reduction may then allow the plant to withstand high wind loads, for example, during storm conditions. In our current study, we do not set out to determine which hypothesis is correct. Instead, we use the latter interpretation of the effect of the grooves on drag reduction, as a source of inspiration and motivation for our work.

Recall from Section 1.1, that smooth cylinders under high Reynolds number flow conditions ($Re \gtrsim 2 \times 10^5$, taking the diameter as the characteristic length), are well-known to undergo a phenomena referred to as the *drag crisis* [34]. With increasing Re, the drag coefficient, C_d, first drops sharply (*critical regime*), until a minimum is reached at a critical Reynolds number, Re^*, after which C_d increases again (*supercritical regime*), before plateauing (*transcritical regime*) [38, 41]. This drop in drag is related to a delay in separation caused by a laminar-to-turbulent flow transition



Figure 2-1: Representative photograph of a Saguaro cactus (Scottsdale, Arizona) [87].

in the boundary layer. Roughening the surface of the cylinder causes the drag crisis to occur earlier by promoting the transition from a laminar to turbulent boundary layer [12, 41, 78].

Studies specifically on the effect of grooved cylinders are numerous, and many were covered in detail in Section 1.4. Overall, combining the findings from the past studies, establishes that different groove patterns can change the aerodynamic performance of a cylinder. However, these investigations were limited in the range and extent of the explored parameter space by the time and cost needed to fabricate individual samples for each configuration. Additionally, each individually manufactured sample (with a fixed surface shape) minimizes the drag coefficient at a single value of Reynolds number, Re^*, whereas, for all other Re, the drag can be specifically higher. As such, an important shortcoming precluding the translation of this drag reduction mechanism with fixed topographies into engineering applications is that any aerodynamic enhancement is limited to relatively narrow ranges of Re.

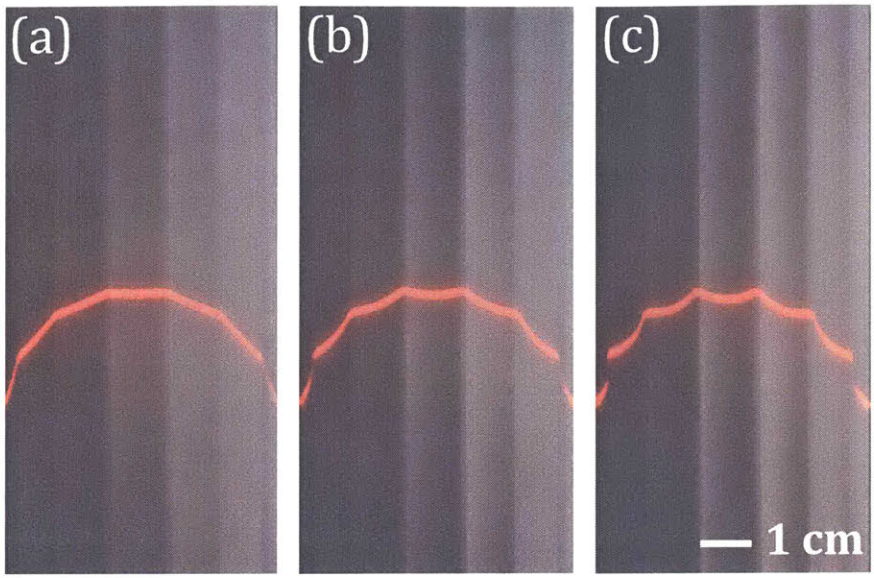


Figure 2-2: Photographs of a grooved cylindrical sample covered by a stretched latex film. The surface topography can be morphed pneumatically by increasing the pressure differential between the inside and the outside of the samples: (a) $\Delta p = 1000\,\text{Pa}$, (b) $\Delta p = 5000\,\text{Pa}$, (c) $\Delta p = 10,000\,\text{Pa}$. A laser sheet aligned at $45\,^\circ$ with respect to the cross section of the sample is used to measure the depth of the surface grooves.

In this Chapter, we study the aerodynamic performance of cylinders using a single, albeit morphable, sample whose topography can be varied systematically and precisely on demand. The tuning of the surface shape is accomplished by the pneumatic actuation of the flexible elastomeric film covering an inner rigid skeleton, with a single pressure signal that can be continuously varied. In Fig. 2-2, we present representative photographs of a sample at three different states of pneumatic loading ($\Delta p = 1$, 5 and 10 kPa). Therefore, by varying the internal pressure of the sample, we can set the sample to numerous fixed groove shapes, specifically the groove depth. Wind tunnel tests are used to characterize the aerodynamic drag of our samples, over a wide range of Reynolds numbers, for each fixed depth. We determine which groove depth exhibits the lowest drag coefficient at any given Reynolds number. Finally we present a system in which the drag on the samples can be automatically minimized by changing the groove depth '*on the fly*', depending on the measured velocity of the oncoming flow.

2.2 Wind tunnel experimental setup and sample fabrication

Our cylindrical specimens comprised a rigid acrylic skeleton covered by a stretched cylindrical film made of latex. The rigid skeleton contained a series of inner cavities set by an array of equally spaced radial spokes, aligned axially. Decreasing the internal pressure in the cavities caused the outer latex film to stretch further and, consequently increase the depth of the axial grooves. Therefore, the topography of the samples could be tuned gradually and on-demand, through pneumatic actuation. These specimens were then loaded aerodynamically in a flow field generated by a wind tunnel. The resulting drag force was measured directly by a precision system containing a load-cell. The velocity of the incoming flow was then varied systematically to determine the drag coefficient, C_{d}, over a range of Reynolds number ($2.5 < Re\,[\times 10^4] < 15$), and for different set values of the groove depth.

We proceed by describing in more detail, first, the experimental apparatus and, then, the specimen fabrication procedure.

2.2.1 Experimental apparatus

Fig. 2-3(a) shows a photographs of the experimental apparatus used for wind tunnel tests throughout this chapter, as well as Chapters 3 and 4. The incoming air flow was produced by an open return wind tunnel with a $30.5 \times 30.5\,\mathrm{cm}^2$ test section, which was capable of producing uniform steady flow speeds of $2 < U\,[\mathrm{ms}^{-1}] < 34$, measured by a pitot tube and a high accuracy capacitance manometer (690A Baratron, MKS Instruments). For all the values of U used in this study, the turbulence intensity, defined as fluctuations of the wind speed, were below 1% of the mean velocity. The flow direction was aligned with the y-axis (see the definition of the axes in Fig 2-3(a)). The cylindrical specimens were mounted such that they spanned the width of the wind tunnel, along the x-direction, perpendicular to the incoming flow, and positioned at the vertical center of the test section. The specimen protruded through

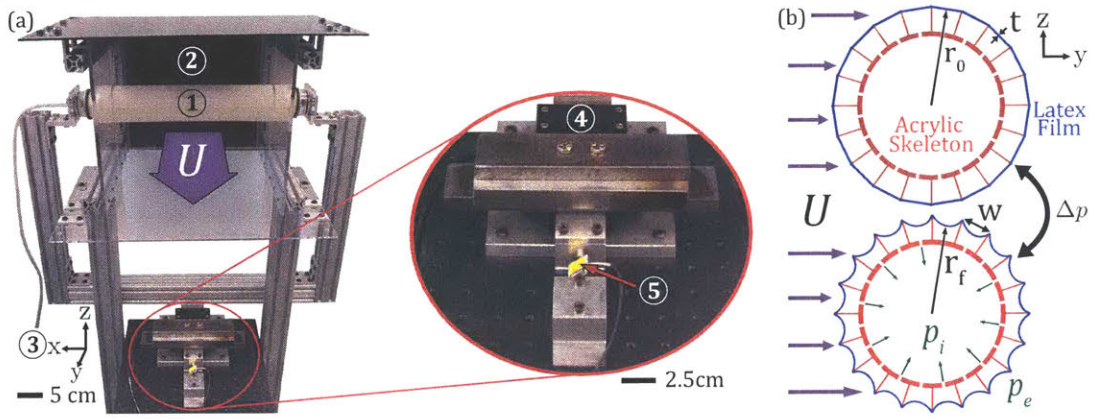


Figure 2-3: Setup of wind tunnel experiments. (a) Photograph of the experimental apparatus used to measure the drag force on a grooved cylindrical specimen under aerodynamic loading. The specimen (1), mounted across the wind tunnel (2), is rigidly connected to a force sensor (5) via an air bearing (4) to measure the exerted aerodynamic drag forces. The internal pressure of the specimen is set by a regulated vacuum pressure source (3). The air flow with average far-field speed U is aligned perpendicularly to the axis of the specimen. (b) Schematic diagram of the cross-section of the specimen (top) comprising a rigid acrylic skeleton (red) covered by a thin latex film (blue, thickness $t = 0.25\,\text{mm}$). Depressurizing (Δp) the inner cavity of the shell results in deeper grooves (bottom).

holes in the y-z side walls of the test section. At the location of the samples, the displacement thickness of the boundary layer was $\delta^* \approx 1.5\,\text{mm}$. In comparison to the length of the samples, the boundary layer is therefore small (approximately 0.5%).

The cylindrical specimens were 43 cm long with a 3.5 cm radius (measured from the center of the cylinder to the extremity of one of the spokes). Circular caps made out of acrylic were inserted at both ends of the specimen to ensure sealing. One of these endcaps (left-hand side of Fig 2-3(a)) contained a port to connect the specimen, via PVC tubing, to a vacuum pump (DOA-P704-AA, Gast). A high-resolution electronic pressure control valve (QPV1, Proportion-Air, Inc.) was introduced between the specimen and the vacuum pump to regulate the pressure of the system using a data-acquisition device (DAQ, USB-6008, National Instruments). This pressure control valve was then controlled by a custom LabVIEW program (LabVIEW 2010, National

Instruments). The two endcaps of the specimen were mounted onto a U-shaped aluminum frame, which was itself bolted to one end of a linear air bearing (RAB2, Nelson Air Corp.). The other end of the air bearing was connected to a precision load-cell (LRM200 Minature S-Beam Load Cell, Futek). With this setup, aerodynamic drag forces exerted onto the grooved cylindrical specimens could be measured in the range $0.05 < F_{\mathrm{d}}\,[\mathrm{N}] \leq 22.2$.

Both the force and the wind velocity signals were digitized simultaneously by the DAQ system. The experimental setup detailed above allowed for the control of the internal pressure of the cylindrical specimens (and thus the shape of the grooves), while simultaneously enabling measurement and recording of both the drag forces on the specimen and the velocity of the incoming flow.

2.2.2 Fabrication of the specimens

In Fig. 2-3(b), we present a schematic diagram of the cross-section of our custom fabricated cylindrical specimens. The specimens consisted of a latex film (represented by the blue line in Fig. 2-3(b)) stretched over a rigid acrylic skeleton (represented by the red circle with spokes in Fig. 2-3(b)).

To manufacture the rigid skeleton, first, spokes with a height of 9.5 mm were laser cut (Laser Pro, Spirit GLS) out of 1.6 mm thick acrylic plates. Second, a series of rectangular holes were laser-cut on the surface of an acrylic tube (50.8 mm outer diameter and 3.175 mm wall thickness). There were two sets of holes cut into the base tube. The first set was uniformly spaced around the circumference of the cylinder and were subsequently plugged with the spokes to create the skeletal structure, with an outer diameter of 69.8 mm. The second set of holes was cut to allow air to flow between the inside of the tube and the cavities created beneath the latex film (more details below). This allowed for the pressure to equalize inside the base tube and in the cavities. The spacing between the ends of two neighboring spokes, w, depended on the number of grooves in the specimen. In our experiments we used specimens with $N = \{14,\ 16,\ 20,\ 24\}$ grooves (*i.e.*, $w = \{15.5,\ 13.6,\ 10.9,\ 9.1\}$ mm, respectively).

Thin latex sheets (thickness $t = 0.25$ mm) were cut into rectangles, and the ends

glued together to form tubular shells with 50.8 mm diameter. The latex film was then stretched over the acrylic skeleton and the ends were sealed with o-rings. The resulting value of the prestretch (defined as the ratio between the perimeter of the latex film after and before stretching over the skeleton) depended on the number of grooves of the specimen: $\lambda = \{1.364, 1.366, 1.369, 1.371\}$ for $N = \{14, 16, 20, 24\}$, respectively. These values of pre-stretch were chosen to ensure that no fluttering of the latex membrane was observed in the wind-tunnel experiments (Section 2.5.2), especially in the upper range of Reynolds numbers explored, where vortex-induced vibrations were otherwise possible.

2.3 Material characterization of the latex

The elastic properties of the latex films (needed for the Finite Element Simulations detailed in Section 2.4, below) were determined using a universal testing machine (5943, Instron). Dog bone specimens (ASTM D412 type A and B) were laser-cut from the same latex material used to make the specimens, and tested under uniaxial tension.

The tests were executed with a constant cross head velocity of 20 mm/min. Experiments were performed at slower velocities to check for strain rate dependence, however the results were nearly identical, so it was determined that 20 mm/min was slow enough to neglect viscoelastic effects. Two lines were drawn on the specimens and photographed at regular intervals (5 seconds between each photograph) while the universal testing machine recorded the force. Fig. 2-4 show representative photographs of the dog bone tests at various levels of stretch ranging from $1 \leq \lambda \leq 2.71$. The photographs were used to determine the stretch over time, while the force measurements were used to determine the stress over time.

The first tensile tests were run with "virgin" specimens. The virgin specimens were unstretched after the laser cutting procedure was complete. We ran subsequent experiments with the same specimen after the initial test. Fig. 2-5(a) shows the results of successive tests with the same specimen.

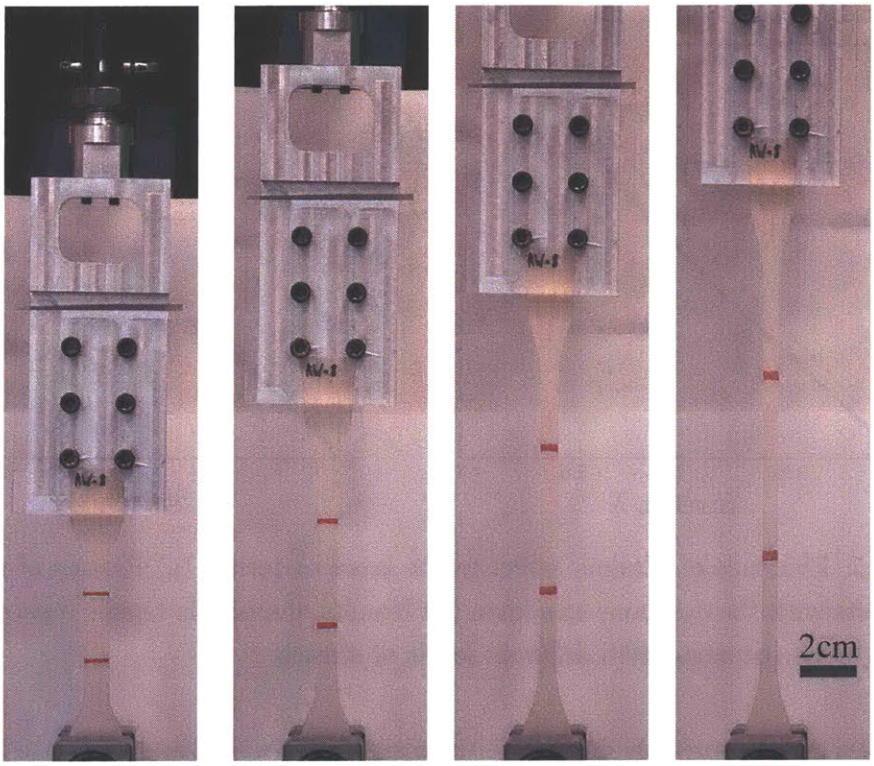


Figure 2-4: Photographs of a dog bone specimen during a tensile test at $\lambda = 1$, 1.57, 2.14 and 2.71. The red lines are used to determine the level of stretch in the specimens.

After the second test, each successive experiment yielded nearly identical results, as shown by the colored lines in Fig. 2-5(a). However, the test on the virgin specimen, showed different results from the subsequent tests. This is an example of Mullins' effect [131]. Mullins' effect, is a phenomenon in which the stress-strain behavior of a rubber material is history dependent, specifically depending on the maximum loading to which the material has been exposed [131]. Fig. 2-5(b) shows the experimental results of a single specimen stretched to several different levels. The virgin specimen was stretched to $\lambda = 1.66$ and then again stretched the same amount. The specimen was then stretched to $\lambda = 1.84$ twice and subsequently stretched two times to each $\lambda = 2.13$ and 2.69. These tests are further evidence that the latex material we used exhibits Mullins' effect.

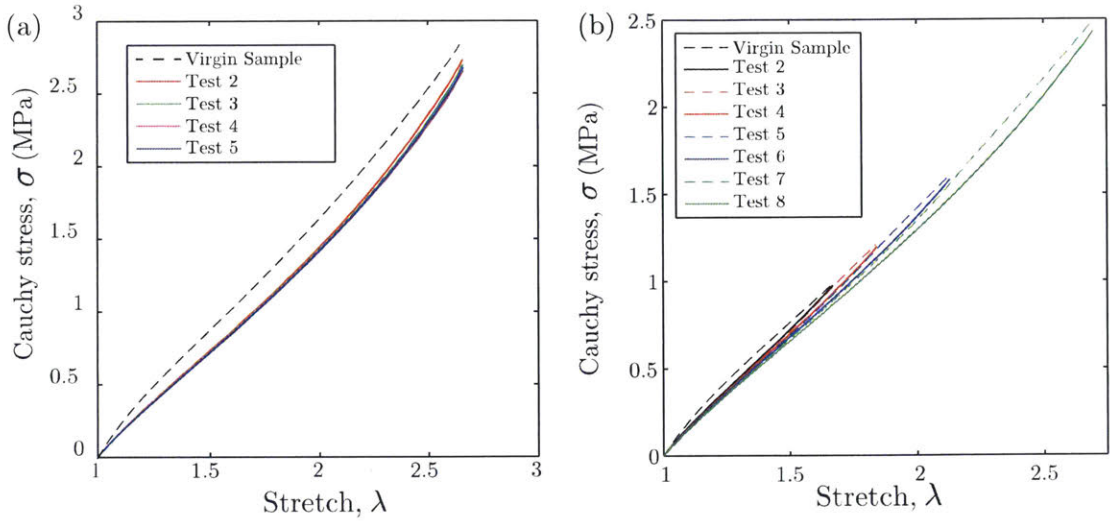


Figure 2-5: Evidence of Mullins' effect in the latex material. (a) Results of multiple tensile tests with the dog bone specimen (b) Results of multiple tensile tests with the same dog bone specimen with different levels of stretch.

In order to appropriately determine the constitutive model and associated parameters to use in the simulations, it was important to know how the material would behave under conditions similar to those that would be experienced during the grooved specimen experiments. With the grooved samples, we preconditioned the latex to approximately a stretch of $\lambda = 1.85$ by increasing Δp until that value of stretch was reached ($\Delta p \approx 15$ kPa). This magnitude of stretch is higher than the maximum reached in the specimens during wind tunnel experiments ($\lambda_{\max} \approx 1.7$) so it was deemed to be a sufficiently high stretch with which to precondition the specimens.

Additional tensile tests were performed with 8 different dog bone specimens, after being preconditioned to a stretch of $\lambda = 1.85$. The results of these tests are shown with the solid black lines in Fig. 2-6. Using a custom Matlab script, the data was fit to different constitutive models. The red dashed line and blue dashed-dotted line are the best fits of the Gent and Neo-Hookean constitutive models, respectively.

It was determined that the Gent model fit the experimental data the best, thus it was selected for the Finite Element simulations presented in Section 2.4. The Gent model is a rubber elasticity model that applies to materials with non-linear behavior at large deformation. The model makes use of the following strain energy density

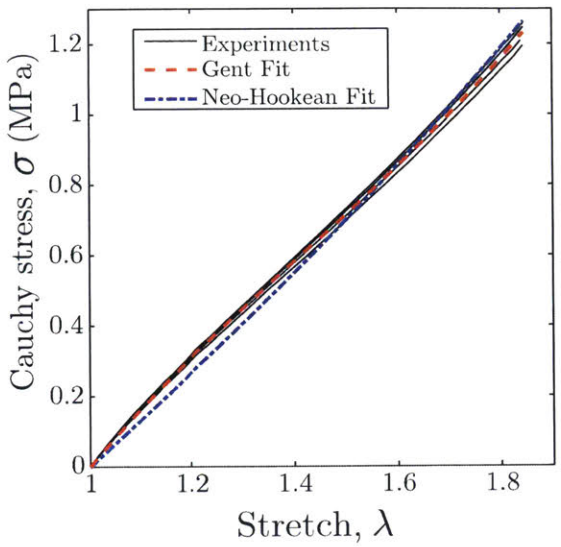


Figure 2-6: Results of fitting the Gent and Neo-Hookean constitutive model to the experimental data.

function:

$$W = C_1 J_m \ln\left(1 - \frac{I_1 - 3}{J_m}\right) + C_2 \ln\left(\frac{I_2}{3}\right), \tag{2.1}$$

where C_1, C_2 and J_m are the parameters used to fit the experimental data, and I_1 and I_2 are the invariants of the deformation tensor and are defined as:

$$I_1 = \lambda_1^2 + \lambda_2^2 + \lambda_3^2 \tag{2.2}$$

$$I_2 = \lambda_1^{-2} + \lambda_2^{-2} + \lambda_3^{-2}, \tag{2.3}$$

where λ_i are the principal stretches. The Gent model was implemented in Abaqus through the user defined function, UHYPER. The strain energy potential was modified to avoid the singularity at $I_1 = J_m + 3$ by following the example of Ref. [132]. The script for the UHYPER function was written by Francisco López Jiménez (a former post-doc at the Elasticity, Geometry and Statistics Laboratory at MIT, and now at the University of Colorado Boulder).

In the Gent model of Eq.(2.1), the parameters C_1 and C_2 are elastic coefficients, and J_m is a coefficient related to the maximum stretch ratio. The two elastic coefficients can be used to estimate the shear modulus, G, of the material. From the fitting

of the Gent model to the stress-stretch data shown above we obtained: $J_m = 37.5 \pm 1.7$, $C_1 = 115.7 \pm 5.7\,\text{kPa}$, $C_2 = 518.0 \pm 30.2\,\text{kPa}$ and $G = 577 \pm 32\,\text{kPa}$.

2.4 Mechanics of deformation of the surface

In this section, we present the results of both mechanical experiments and finite element simulations, used to characterize how the shape of the grooves, specifically the groove depth, d, depends on the internal pressure, Δp. This relationship between d and Δp will be required later (Section 2.5) to inform the wind tunnel experiments. In Fig. 2-7(a), we show a schematic diagram of a segment of the latex film suspended above a single cavity of the rigid skeleton. When the value of the pressure inside the cavity, p_i, is smaller than the exterior pressure, p_e, the pressure differential, $\Delta p = p_e - p_i$, loads the latex film. This loading causes the film to deform inward and, thus, deepen the surface groove. To study the mechanics of deformation of the film, we performed a series of experiments where Δp was fixed to a set value and a laser sheet was then projected onto its surface, at a 45° angle relative to the central axis of the cylinder. Photos were taken of the resulting line of illumination, representative examples of which are shown in Fig. 2-2. From these photographs, we extracted the height profile of the grooves, using a custom image processing code (Matlab).

Along with the physical experiments, we performed Finite Element Modeling (FEM) using Abaqus/Standard 6.14. Given the axial symmetry of the system, the model was simplified to a single two-dimensional (2D) groove section (shown in Fig. 2-7). The acrylic skeletal structure was simulated with rigid elements, while the film was simulated with 2D solid elements (CPE4H). A convergence study was performed, which led to the selection of a regular mesh with 150 elements along the arc-length of the latex film, and 8 elements along its thickness. The simulation protocol was as follows: (i) first, the film was deformed to the appropriate value of prestretch ($\lambda = \{1.364, 1.366, 1.369, 1.371\}$ for the specimens with $N = \{14, 16, 20, 24\}$, respectively); (ii) then, a uniform negative pressure was applied to the inner surface of the film, so that the pressure differential was increased linearly from $\Delta p = 0$ to

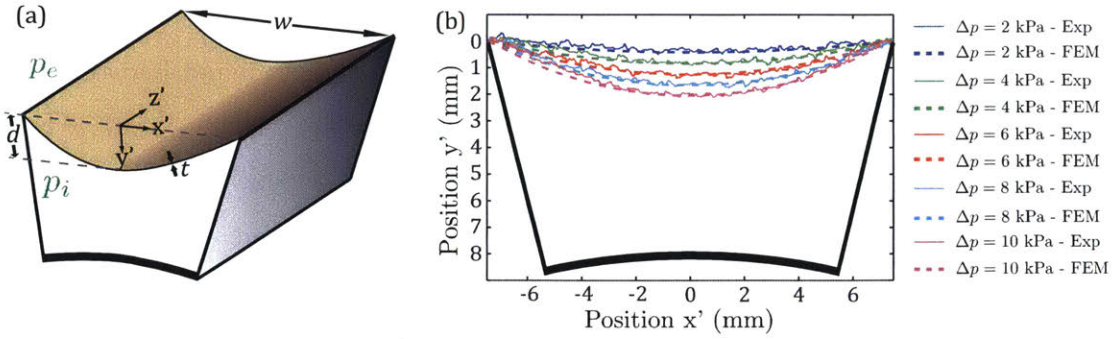


Figure 2-7: Setup of the FEM simulations. (a) Schematic diagram of a single groove after applying the pneumatic loading by setting the pressure differential to Δp. The groove depth, width and film thickness are represented by d, w and t, respectively. (b) Results of experiments (solid lines) and FEM simulations (dashed lines) showing the shape of the surface of the latex film at increasing values of $\Delta p = \{2,\ 4,\ 6,\ 8,\ 10\}$ kPa, for a specimen with $N = 14$ grooves. The rigid (acrylic) skeleton is represented by the thick black lines. Given the periodicity of the system, only the data for a single groove is shown.

$\Delta p = 10$ kPa. This pneumatic loading was implemented as a live pressure, such that the force was always applied normal to the surface.

In Fig. 2-7(b), we show examples of the experimental and computed surface profiles of a single groove, at five different values of the internal pressure ($\Delta p = \{2,\ 4,\ 6,\ 8,\ 10\}$ kPa), for a specimen with $N = 14$ grooves. The groove profiles closely resemble catenaries, especially for small values of Δp, which is to be expected given the nearly radial pneumatic loading on the latex film. We find excellent agreement between the experiments and the FEM simulations, noting that the latter involve no free fitting parameters.

From the groove profiles, a representative set of which was shown in Fig. 2-7(b), we measure the groove depth as $d = r_\mathrm{o} - r_\mathrm{f}$, where r_o and r_f are defined in Fig. 2-3(b), and d is drawn schematically in Fig. 2-7(a). It is worth noting that the groove depth, d, is defined relative to the initial state of the specimen with no pressure being applied. This means that for a specimen with N grooves, $d = 0$, corresponds to an N-sided polygon rather than a perfect cylinder. However, for increasing values of N, the specimen approaches the a smooth cylinder case. In Fig. 2-8(a), we plot d versus Δp,

for four different specimens with $N = \{14, 16, 20, 24\}$, from both the experiments and the corresponding FEM simulations; excellent agreement is found between the two. The errorbars on the experimental data represent the standard deviation of five different tests. We find a linear relationship between the groove depth and the internal pressure. The constant of proportionality decreases for the specimens with increasing N. This is likely due to the difference in stretch required to reach the same groove depth in specimens with more grooves. Given a constant groove depth, specimens with higher N achieve a higher stretch than those with fewer grooves. Thus, a larger load, *i.e.* Δp, must be applied to specimens with more grooves.

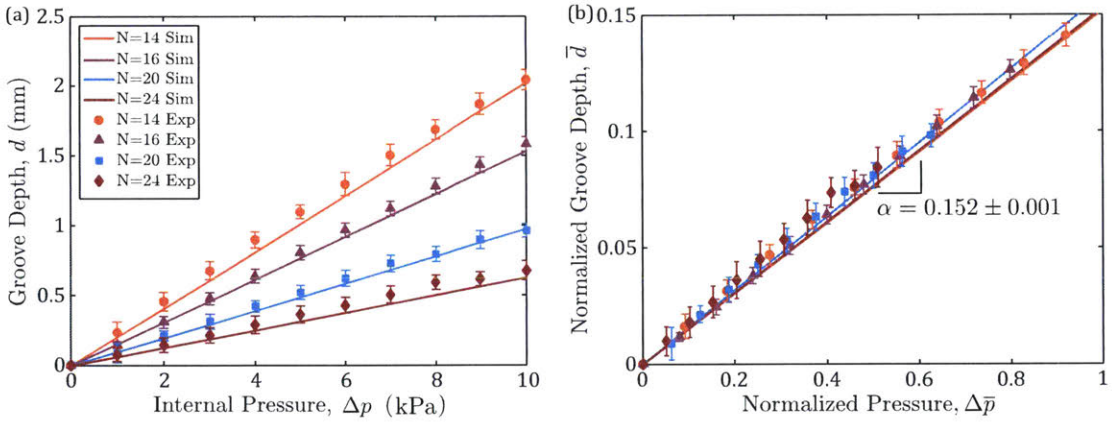


Figure 2-8: Dependence the mechanical deformation on the pneumatic actuation. (a) Groove depth, d, versus pressure differential, Δp, for specimens with different numbers of grooves; see legend, which also applies to (b). Solids lines and data points correspond to simulations and experiments, respectively. (b) Normalized groove depth, $\overline{d} = d/w$, as a function of normalized pressure, $\Delta\overline{p} = \Delta pw/[Gt]$, for the same data as in (a). The slope of the best linear fit to the data is $\alpha = 0.152 \pm 0.001$.

Next, we nondimensionalize the groove depth as $\bar{d} = d/w$, and the pressure as $\Delta\bar{p} = \Delta pw/[Gt]$. The latter was chosen based on dimensional analysis. In Fig. 2-8(b), we plot these dimensionless quantities and find that all the experimental and numerical data collapse onto a linear master curve, for all of the specimens tested:

$$\bar{d} = \alpha\Delta\bar{p}, \tag{2.4}$$

where $\alpha = 0.152 \pm 0.001$ was determined by fitting the data. We were not able to rationalize this pre-factor, so we will use Eq.(2.4) as a semi-empirical relation.

Thus far, our results establish a predictive relationship between the groove depth and the internal pressure of the specimens. With this knowledge, together with the electronic pressure control valve, we are able to set and vary the depth of the grooves on demand. This capability was used in the subsequent wind tunnel experiments to systematically characterize the dependence of the aerodynamic performance of our specimens, specifically the drag coefficient, on the groove depth. The details and results of these experiments are addressed next.

2.5 Aerodynamic drag characterization with wind tunnel experiments

Above, through mechanical experiments and FEM simulations, we established a relationship between the depth of the grooves and the internal pressure of the specimens. We proceed by characterizing the aerodynamic performance of our grooved specimens using wind tunnel tests. More specifically, we shall systematically quantify how the aerodynamic drag coefficient of the specimens, C_d, varies with the Reynolds number of the flow (in the range $2.5 < Re\,[\times 10^4] < 15$), as a function of the groove depth, d.

Two types of experiments were undertaken with either (i) *fixed* or (ii) *active* grooves. (i) For the *fixed groove experiments*, we measured C_d across the full range of Re, while setting the internal pressure of the specimen at a fixed value, to target a constant value of d. In doing so, we followed the mechanical design principles identified in Section 2.4 that relate d with Δp. For each value of d, we tabulated the corresponding minimum value of C_d and the critical Re^* at which it occurred. (ii) Additionally, we performed *active groove experiments* where the Reynolds number was gradually increased, and at each Re, the groove depth was automatically adapted to minimize the drag coefficient. As we shall show below, these morphable cylinders with active control of their groove depth exhibited an overall aerodynamic drag, across

the full range of Re, that was significantly lower than any of their fixed counterparts.

2.5.1 Experimental protocol to measure the aerodynamic drag coefficient

During each wind tunnel experiment, the groove depth of the specimens was set by varying the internal pressure through the vacuum regulator as described in Section 2.2.1. The groove depth was varied from $d = 0$ to $d = 0.81\,\mathrm{mm}$ (*i.e.*, $\bar{d} = d/w = 0.1$ in dimensionless form), for four specimens with the following numbers of grooves: N =14, 16, 20 and 24. The wind speed was then slowly increased at a rate of $\dot{U} \approx 0.05\,\mathrm{m/s^2}$, until either the wind speed reached a maximum (at $U = 34\,\mathrm{ms^{-1}}$) or the signal from load-cell became saturated (at $F_\mathrm{d} = 22.25\,\mathrm{N}$).

Based on the measured quantities, we calculated the Reynolds number as:

$$Re = \frac{UD}{\nu}, \tag{2.5}$$

where $D = 6.98\,\mathrm{cm}$ is the outer diameter of the specimen, and $\nu = 1.57\times10^{-5}\,\mathrm{m^2s^{-1}}$ is the kinematic viscosity of air (at $25°C$). Moreover, the drag coefficient was calculated as:

$$\bar{C}_\mathrm{d} = \frac{2F_\mathrm{d}}{\rho U^2 L D}, \tag{2.6}$$

where $\rho = 1.18\,\mathrm{kg\,m^{-3}}$ is the density of air (at $25°C$), and $L = 30.5\,\mathrm{cm}$ is the width of the wind tunnel. All experiments were performed in the range $2.5 < Re\,[\times10^4] < 15$, over which, the measured drag force was in the range $0.3 < F_\mathrm{d}\,[\mathrm{N}] < 17$.

It is important to note that the projected area of the specimen is relatively large compared to the cross-sectional area of the test section of wind tunnel; the blockage ratio is $\beta = DL/L^2 = 0.23$. As such, blockage effects [133] need to be taken into account. Otherwise, calculating the drag coefficient directly from Eq.(2.6) would lead to artificially high values. In order to compensate for this blockage, Maskell's

theory [134] was used to *correct* the measured drag coefficient as:

$$C_{\mathrm{d}} = \frac{\bar{C}_{\mathrm{d}}}{1 + \epsilon\,\beta\,\bar{C}_{\mathrm{d}}}, \tag{2.7}$$

where $\bar{C}_{\mathrm{d}}$ is the *uncorrected* drag coefficient (from Eq. (2.6)) and $\epsilon = 0.3453$ is a numerical factor determined using the following fitting protocol. Wind tunnel experiments were first performed using four smooth, rigid cylinders of diameters $D = \{1.90, 3.81, 6.35, 7.62\}$ cm, in the range of Reynolds number, $2.5 < Re\,[\times 10^4] < 15$. The results of these experiments are shown in Fig 2-9.

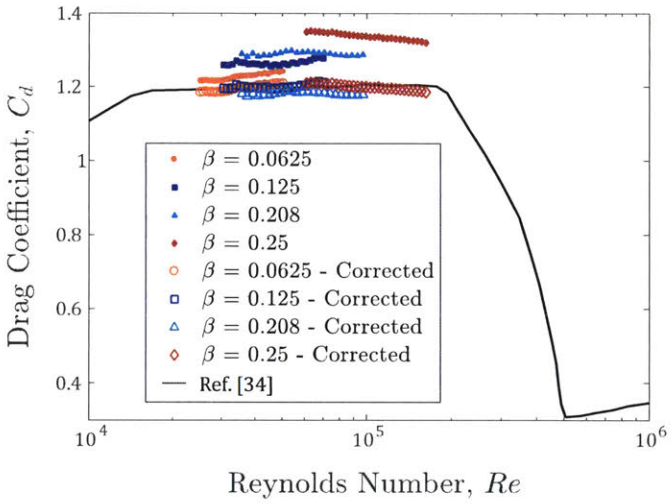


Figure 2-9: Drag Coefficient, C_d, versus Reynolds number, Re, for smooth cylinders of different diameters and thus blockage ratios ranging from $1.90 < D\,[\mathrm{cm}] < 7.62$ and $0.0625 < \beta < 0.25$, respectively. The solid black corresponds to the classic curve for a smooth cylinder [34]. The solid symbols are the uncorrected experimental results, and the open symbols are the corrected results using Maskell's theory [134] with $\epsilon = 0.3453$, which was determined using the procedure described in the text.

Throughout this range of Re, our smooth cylinders, unlike the grooved specimens, remained in the subcritical regime (*i.e.* prior to the drag crisis), where the drag coefficient for a smooth cylinder is well-known to be 1.2 [34]. As expected, for all the diameters tested experimentally, the $\bar{C}_{\mathrm{d}}$ calculated through Eq.(2.6) were consistently above this classic value. We then took the experimental data for $\bar{C}_{\mathrm{d}}(Re)$, displayed as the solid symbols in Fig. 2-9, and calculated C_{d} through Eq.(2.7), while taking

ϵ as a free fitting parameter. In the fitting procedure, we minimized the difference $|\langle \bar{C}_d \rangle - 1.2|$, using the `fminsearch` algorithm in Matlab [135], where $\langle \cdot \rangle$ represents averaging over the full Re range. In the fitting procedure, the uncorrected drag coefficients of all of the cylinders were considered simultaneously in order to attain a single value of ϵ that applied to all the specimens by minimizing the total difference from the expected classic value of 1.2. This procedure yielded $\epsilon = 0.3453$. The open symbols in Fig. 2-9 represent the drag coefficients for each specimen when this particular value of ϵ is used for the blockage correction. As a result all four cylinders used in this calibration, upon correction, exhibited the same value of $C_d \approx 1.2$. For the remainder of this study, we will report aerodynamic drag coefficients corrected through Eq.(2.7), with this specific value of ϵ, to take blockage effects into account.

2.5.2 Aerodynamic drag coefficient versus Reynolds number for the fixed grooved specimens

In Fig. 2-10(a), we plot a family of curves of the measured (and corrected for blockage effects) drag coefficient, C_d, as a function of Reynolds number, Re, for a specimen with $N = 24$ grooves. The curves represent the specimen in several fixed states with normalized groove depth in the range $0 \leq \bar{d} \leq 0.093$, at equally spaced increments of $\bar{d} = 0.0072$. The classical results for smooth cylinders by Wieselsberger [34] are also plotted (solid black line). For this smooth cylinder case, in the range of $2 \leq Re\,[\times 10^4] \leq 20$, the drag coefficient is constant, at $C_d = 1.2$. The onset of the drag crisis occurs at $Re \approx 2 \times 10^5$, after which C_d drops dramatically for increasing Re until it reaches the minimum of $C_d = 0.3$ at $Re = 5 \times 10^5$. Hereon, we refer to the lowest value of the drag coefficient and the critical Reynolds number at which it occurs as C_d^* and Re^*, respectively.

For the shallowest groove depth ($\bar{d} = 0$), the drag coefficient in the subcritical regime decreases slowly from $C_d = 1.24 \text{ to } 1.20$ over the range $2.5 \leq Re\,[\times 10^4] \leq 7$. This indicates that in the subcritical regime, the drag on the specimens is slightly higher than that on a smooth cylinder, presumably due to the slightly non-circular

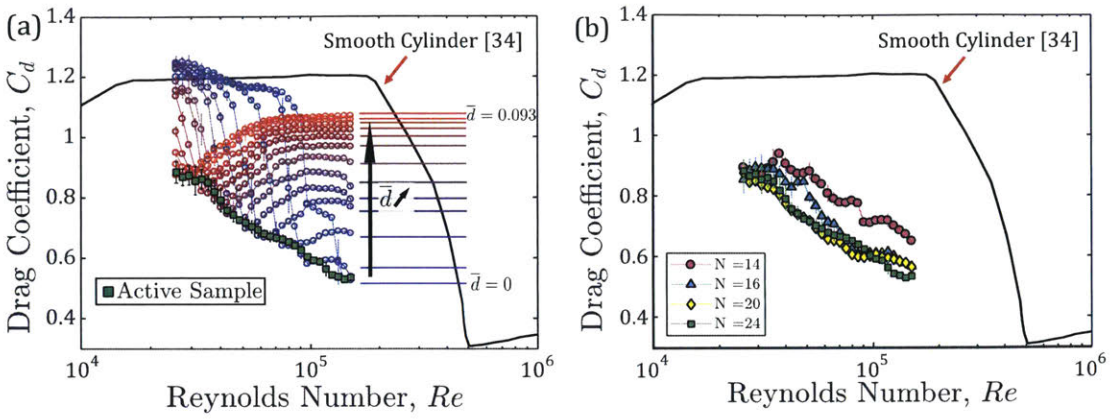


Figure 2-10: Drag Coefficients, C_d, versus Reynolds number, Re, for grooved cylinders at increasing values of depressurization (and consequently increasing normalized groove depth, $\bar{d}$). Solid black line correspond to the result for a smooth cylinder [34].(a) Fixed specimens with $N = 24$ grooves at increasing values of normalized groove depth, $\bar{d}$ (circles) and actively controlled specimen (squares). The fixed specimens range in groove depth from $\bar{d} = 0$ to 0.093 in equally spaced increments of $\bar{d} = 0.0072$. (b) Actively controlled specimens with $N = 14$ (circles), $N = 16$ (triangles), $N = 20$ (diamonds) and $N = 24$ (squares).

cross section. The fixed specimen also deviates from the smooth cylinder in terms of the value of Reynolds number for the onset of the drag crisis: $Re = 7 \times 10^4$ for the fixed grooves specimen with $\bar{d} = 0$, and $Re = 20 \times 10^4$ for the smooth cylinder. For this fixed case, past the initiation of the drag crisis, C_d decreases for increasing Re, but never reaches a minimum. This means that for the fixed groove depth of $\bar{d} = 0$, the critical Reynolds number is above the maximum Reynolds number that we could explore experimentally, $Re^* > 1.5 \times 10^5$.

As the groove depth is systematically increased, the dependence of drag coefficient versus Reynolds number changes dramatically. Focusing on $\bar{d} = 0.043$, the drag crisis begins at approximately $Re = 2.75 \times 10^4$ and the drag coefficient drops sharply until reaching a minimum drag coefficient of $C_\mathrm{d}^* = 0.72$, at $Re^* = 4.85 \times 10^4$. As the Reynolds number is increased further, the drag coefficient increases until asymptoting at $C_\mathrm{d} = 0.86$. For experimental runs with deeper grooves, *e.g.* $\bar{d} = 0.093$, the $C_\mathrm{d}(Re)$ curve is starkly different from the cases with shallower grooves. The drag coefficient

first increases monotonically with Re, but eventually asymptotes to $C_d = 1.05$. This behavior points to the fact that for this particular value of the groove depth ($\bar{d} = 0.093$), the critical Reynolds number is lower than the lower bound of the available experimental range (*i.e.* $Re^* < 2.5 \times 10^4$).

The above results (for $N = 24$ grooves) indicate that as $\bar{d}$ increases, Re^* decreases, whereas C_d^* increases. This trend also holds for specimens with different number of grooves. In Fig 2-11(a), we plot C_d^* versus $\bar{d}$, for specimens with $N = 14$, 16, 20 and 24 grooves. For all of these cases, C_d^* increases with $\bar{d}$. Moreover, for a given value of $\bar{d}$, specimens with increasing N exhibit a decreasing value of C_d^*. Note that, even though $C_d^* \lesssim 0.9$ for all the data shown in Fig 2-11(a), this is not necessarily the absolute maximum value of the C_d^* for these specimens since only curves with a well-defined minimum were considered in our analysis. As described above for the case with $(N, \bar{d}) = (24, 0.093)$, specimens with grooves deeper than those plotted in Fig 2-11 exhibit a monotonically increasing C_d with Re, without a clear minimum (the drag crisis occurs below the experimentally available range of Reynolds number).

Fig. 2-11(b) shows the critical Reynolds number as a function of groove depth, for specimens with different values of N. We find that Re^* decreases with $\bar{d}$ for all cases. It is interesting to note that while there does not seem to be a trend with N, the data for each specimen is consistent with a power-law scaling, $Re^* \sim \bar{d}^{-0.5}$, as is made more clear in the double-logarithmic plot in the inset of Fig. 2-11(b).

The results presented thus far for the $C_d^*(\bar{d})$ and $Re^*(\bar{d})$ behavior are in agreement with the classic work of Achenbach [41] on the effect of surface roughness on drag coefficient for smooth cylinders. In his seminal studies, cylinders with different levels of roughness were fabricated by gluing sand grains of different sizes to the surface of cylinders. His studies defined a roughness coefficient as k_s/D, where k_s is the sand-grain roughness and D is the cylinder diameter. The results showed that increasing the roughness coefficient decreased the critical Reynolds number, and increased the minimum drag coefficient [41]. In our experiments the groove depth is analogous to the sand-grain roughness. For sake of comparison with Achenbach's data, Figs. 2-11(c) and 2-11(d) show $C_d^*(d/D)$ and $Re^*(d/D)$, respectively. Both Achenbach's work [41]

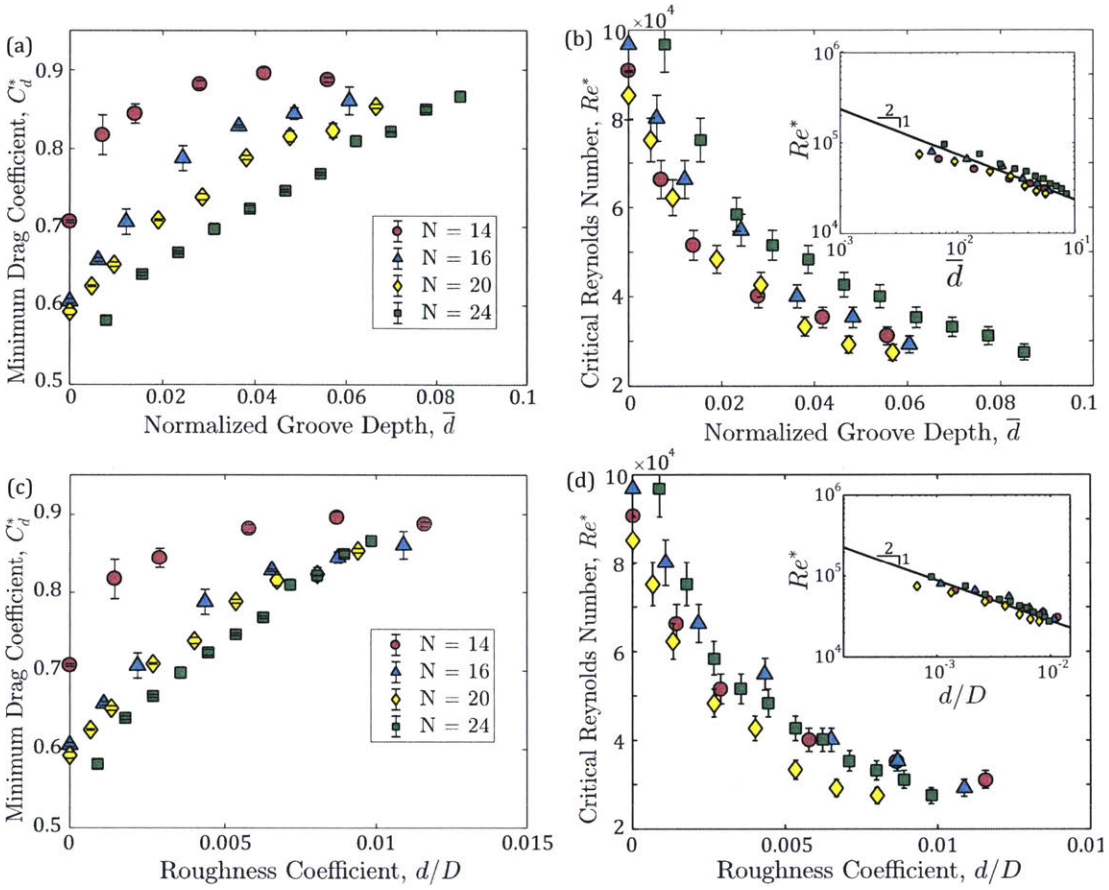


Figure 2-11: Effect of groove depth on the minimum drag coefficient and critical Reynolds number. (a) Minimum drag coefficient, C_{d}^*, of each $C_{\mathrm{d}}(Re)$ curve in Fig. 2-10a, versus normalized groove depth, $\overline{d}$ for specimens with different numbers of grooves (see legend). (b) Critical Reynolds number, Re^*, versus normalized groove depth, $\overline{d}$, for the same specimens used in (a). Inset: Log-log version of the same data suggesting consistency with the power-law scaling $Re^* \sim \bar{d}^{-1/2}$ (solid line). (c) C_{d}^* versus the roughness coefficient, d/D for the same data shown in (a). (d) Re^* versus the roughness coefficient, d/D for the same data shown in (b).

and our own, demonstrate that at each Reynolds number there is a specific groove depth (or roughness in Achenbach's case) which minimizes drag. However, unlike Achenbach's work, which required a separate specimen for each value of roughness, we can obtain obtain a family of curves for different groove depths with a single specimen. This makes it possible to more readily and systematically gather data for a large number of surface shapes. Being able to explore a numerous groove depths,

allowed for the determination of the drag minimizing groove depth at each value of Re. This relationship will be leveraged next to actively control the specimen, such that, given variable wind loading conditions, the grove depth can be automatically varied to minimize the aerodynamic drag.

2.5.3 Minimal aerodynamic drag from active pneumatic control of the surface deformation

The active system used to minimize the drag under changing conditions involved combining all of the results presented thus far. First, in Section 2.5.2, we determined the groove depth which minimized the drag coefficient, at each Reynolds number. To set the groove depth to the optimal value, the corresponding internal pressure was determined according to the relationships found in Section 2.4. Combining these, we find the internal pressure required to minimize C_d at each Reynolds number. Therefore, an experimental control system was developed to actively change the surface morphology to minimize the drag coefficient. This system used the wind velocity data measured by the pitot tube (and therefore Re) and then employed the relationship described above to set Δp in the specimen to target the drag minimizing value. The details of this system will also be used in Chapter 4, and more details are described in Section 4.1 and a schematic of the control loop is shown in Fig. 4-1.

The green squares in Fig. 2-10(a) show experimental data obtained using this active drag minimizing mechanism, demonstrating that the drag coefficient can be reduced significantly and consistently when compared to the fixed surfaces. This minimal behavior is achieved by essentially *surfing the wave* of minimum drag coefficient $C_\mathrm{d}^*(Re)$. As such, the behavior of the active specimen is a lower bound envelope of all of the fixed specimens for different values of $\bar{d}$. Across the full range of Reynolds number explored ($2.5 \leq Re\,[10^4] \leq 15$), the drag coefficient of the active specimens decreases monotonically from $C_\mathrm{d} = 0.90$ to 0.54, which is in stark contrast to the highly non-monotonic behavior of the fixed specimens (due to the presence of the drag crises).

Fig. 2-10(b) reproduces the data in Fig. 2-10(a) (for the active specimen with $N = 24$), but now also adding the results for the active specimens with $N = 14$, 16, and 20. For clarity, the $C_d(Re)$ curves of the corresponding static specimens have not been included. Both active specimens with $N = 20$ and $N = 24$ exhibit similar behavior in which there is a steady monotonic decrease in C_d with increasing Re. For the active specimen with $N = 16$ the relationship $C_d(Re)$ is less smooth than the other specimens. Moreover, for lower Reynolds numbers (around $2.5 < Re[10^4] < 6$), the drag coefficient for this $N = 16$ case is higher than the specimens with a higher number of grooves. Reducing the number of grooves further to $N = 14$, the relationship $C_d(Re)$ becomes even less smooth and the drag coefficient is higher across the full range of Re. Given this, larger values of N seem to enhance the performance of the specimens up to a point, beyond which increasing N has no effect.

It is important to note that the initial state of each specimen is an N-sided polygon due to the fact that the latex film is stretched over the rigid acrylic skeleton. When N is sufficiently large, the geometry is closer to a rough cylinder, with a roughness that can be pneumatically tuned. However, when N is small, such as in the case of $N = 14$, the geometry becomes too discrete for the system to behave as a rough cylinder. We believe that this is the reason why the $N = 14$ active specimen has a $C_d(Re)$ behavior that is significantly less smooth than the other specimens with more grooves.

2.6 Conclusion

In summary, we have experimentally investigated the aerodynamic performance of morphable grooved cylinders, whose surface topography can be varied through pneumatic actuation. We focused on how the the aerodynamic drag of specimens with different groove depth and numbers, changed as a function of the velocity of the incoming flow (in high Reynolds number conditions). The surface topography of each specimen, namely the depth of the grooves, could be systematically and dynamically varied by applying a pressure differential across the outer latex shell.

We first used a series of mechanical experiments, combined with finite element simulations, to study the relationship between the groove depth of the specimens and the pneumatic load applied (Sections 2.3 and 2.4). With a thorough understanding of the mechanical deformation, we proceeded to systematically study the aerodynamics with wind tunnel experiments. In Section 2.5.2, we presented results of experiments with fixed grooves (*i.e.*, setting and then holding Δp constant for the full sweep of Reynolds number, during a single experimental run). These experiments showed that the drag coefficient, C_{d}, versus Reynolds number, Re, curves depended strongly on groove depth. From these experiments with with fixed grooves, we determined the optimal groove depth for a given Reynolds number. With this information at hand, we then introduced an active control system that sensed the incoming wind speed and set the corresponding optimal groove depth to minimize the aerodynamic drag. We demonstrated that the actively morphable specimens exhibited a drag that was consistently and significantly lower than the fixed specimen counterparts (Section 2.5.3).

It should be noted that since we use a pneumatic system to control our specimens, the pressure field on the surface of the specimens resulting from the flow could potentially affect the geometry of the latex membrane in the specimens. However, throughout all of our experiments, the maximum stagnation stagnation pressure is at most 710 Pa, and this value is only reached at the extreme upper limit of the Reynolds numbers explored. Given that the pneumatic loading of the specimens involves a pressure differential that is significantly higher (typically $\Delta p > 1\,\mathrm{kPa}$) than the stagnation pressure, we assumed that the pressure imposed by the flow field has no effect in modifying the resultant geometry of the specimen.

In the next Chapters (3 and 4), we explore a similar method of surface actuation, but with 3D distribution of dimples on the surface, instead of axial grooves.

Chapter 3

Aerodynamic drag on deformable dimpled cylinders: a parameter study

In this chapter, we report results from a study on the aerodynamic performance of cylinders with morphable dimpled surfaces. The surface topography can be varied systematically using pneumatic actuation. The specimens comprise a rigid acrylic skeleton with a flexible latex membrane stretched over it, and the application of a pressure differential, causes the latex membrane to deform. We performed wind tunnel experiments with these specimens to systematically study the effect of several geometric parameters on the aerodynamic performance.

This chapter is organized as follows. In Section 3.1 we motivate the work and highlight related literature. In Section 3.2, we describe the design features of the specimens, as well as their manufacturing process. In Section 3.3, we present the results of mechanical experiments performed to characterize the relationship between the dimple depth and the pressure differential applied to the system. In Section 3.4.1, we describe the procedure followed to perform the wind tunnel experiments. Finally, in Sections 3.4.2 and 3.4.3, we present the results of wind tunnel experiments on specimens for which we systematically varied the arrangement of the dimples.

3.1 Motivation

From the early days of golf, players have sought out technological improvements to equipment to improve their game. Over the years, particular attention has been paid to improvements of the golf ball. Starting in 1618 and for the subsequent 200 years, a ball with a leather shell filled with feathers, known as the "featherie," was the pinnacle of golf ball technology [139]. However, in 1845 the introduction of the Gutta-percha ball, a.k.a. the "guttie," made the featherie obsolete [48]. Gutta-percha is the evaporated sap of various tropical trees which, when heated, can be molded into rubbery spheres [140]. The ability to mold balls from gutta-percha made manufacturing of golf balls significantly easier and improved their flight. It was discovered that the ball flight improved further when the initially smooth ball had a damaged surface [140]. Armed with this knowledge, manufacturers began making golf balls with intentionally patterned surfaces. Initially, it was common for balls to be covered with a series of bumps, known as a "bramble pattern," but eventually it was discovered that balls with indentations performed better than balls with protrusions [140]. In 1908, the first patent for a dimpled golf ball was issued [69]. Since then, the golf ball industry has grown dramatically, and manufacturers are constantly trying to improve the performance of balls to capture a larger piece of the over half a billion dollar golf ball market [141].

The dimples on golf balls have generated a large body of research into the aerodynamic performance of dimpled bodies [48, 61, 67, 68, 70, 71, 72, 74, 75]. Numerous studies on the drag forces on golf balls have shown that the dimples cause the drag crisis (defined in Section 1.1) to occur at a lower Reynolds number, followed by only a slight increase in the drag coefficient after the initial drop [48, 74]. It has also been shown that the geometry of the dimples plays an important role in the relationship between the drag coefficient and the Reynolds number [74, 75].

The details of many of the studies on dimpled surfaces were covered in Section 1.3. One common drawback in several of the existing studies on dimpled surfaces is the requirement that, to test a different dimple geometry, a new specimen has to be man-

ufactured. This cost, in both time and money, has limited the kind and number of parameters that have been studied. One study by Terwagne *et al.* [75] utilized the wrinkling instability to create spheres with dimples that could have variable depth. They found that, by tuning the dimple depth during wind tunnel experiments, they could effect the dependence of the drag coefficient on Reynolds number [75]. Another recent study, by Hodges and Seffen [142], explored the drag on cylinders with a compliant surface capable of forming dimples. By compressing a foil sleeve wrapped around a rigid cylinder with a gap between the two, a buckling instability formed periodic dimple like patterns on the surface [142]. In this study, changing the size of the gap and the level of compression induced different surface patterns [142]. Hodges and Seffen performed wind tunnel experiments with these specimens and demonstrated that, the drag coefficient could be reduced by as much as 68% when compared to a smooth cylinder [142]. It is important to note that in these tests, the aerodynamic forces themselves induced a change in surface shape. However, when the wind speed was reduced, the surface recovered to its initial form [142].

3.2 Design, fabrication and assemblage of the experimental specimens

The design of our dimpled cylindrical specimens was similar to that of the grooved experiments presented in Chapter 2. The specimens comprised a rigid acrylic tube with a series of laser-cut holes in its surface. A tube was formed from a flexible latex membrane, and was stretched over the acrylic skeleton. By depressurizing the inside of the cylinder, the latex stretched into the holes, thereby forming dimples. These dimples were circular depressions on the surface, with a diameter fixed by the size of the laser-cut holes in the base acrylic cylinder. The depth of the dimples was varied by changing the magnitude of the applied pressure differential.

Fig. 3-1(d) shows a schematic diagram of the layout of the dimpled specimens, from the top view. The specimens are made of a rigid acrylic tube with an outer

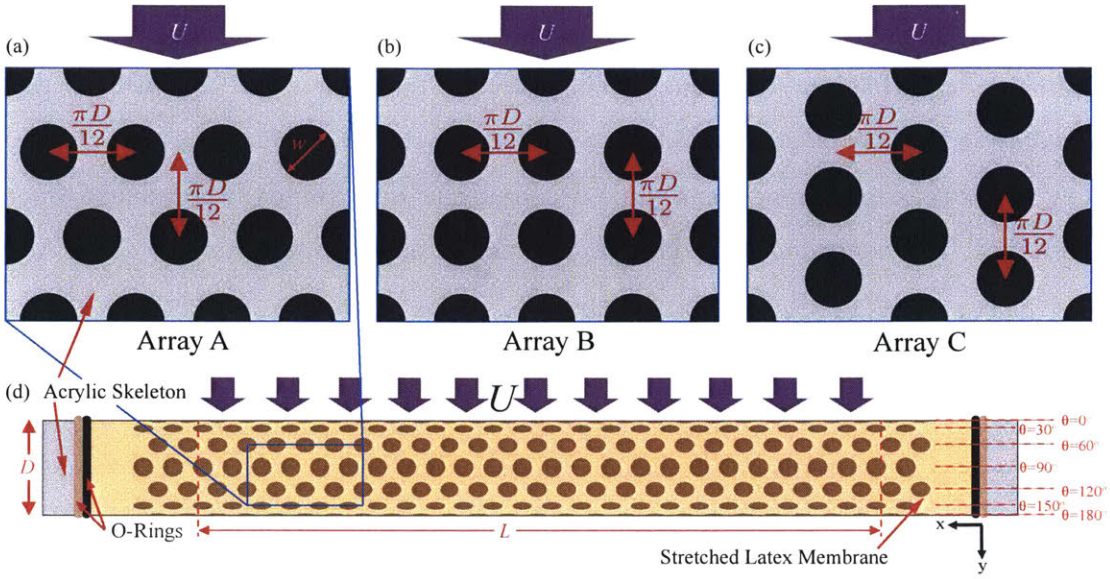


Figure 3-1: Design of the dimpled specimens. (a-c) Schematic diagram of the three different arrays explored in the experiments. The gray area represents the solid base acrylic skeleton, and the black circles correspond to the location of the holes. (d) Top view schematic diagram of the entire specimen with the latex membrane stretched over the acrylic base tube and sealed with o-rings. The stagnation point of the flow occurs at $\theta = 0°$

diameter of $D = 50.8$ mm and wall thickness of 3.175 mm. Using a rotary fixture of the laser cutter (Laser Pro, Spirit GLS), circular holes were cut into the cylinder. The cylinder was cut to a length of 44.5 cm (long enough to span through the width of the wind tunnel, $L = 30.5$ cm). The holes were arranged uniformly on the surface of the cylinders with multiple different distributions. We will refer to the different hole patterns shown in Figs. 3-1(a), (b) and (c) as *Array A*, *Array B* and *Array C*, respectively. Each array was designed as a series of circular holes on a 2D plane which was then projected onto the circumference of the circular cylinders.

Array A is a hexagonal lattice of holes, with horizontal rows aligned along the x-axis of the cylinder, as shown in Fig. 3-1(a). The rows of holes are equally spaced, such that there are 12 rows around the circumference of the specimens. Therefore, the spacing between rows along the surface was $\frac{\pi D}{12} \approx 13.3$ mm. The axial spacing between holes was the same as the spacing between rows, and every other row was

perfectly out of phase to create the hexagonal array shown in Fig. 3-1(a). *Array B*, has a square distribution of holes with a spacing of $\frac{\pi D}{12} \approx 13.3$ mm, as shown in Fig. 3-1(b). *Array C* has holes distributed with the same spacing as *Array A*, however, the orientation of the pattern is perpendicular to that of *Array A*, as shown in Fig. 3-1(c).

For each of these distributions, several different dimple diameters, w, were examined. For *Array A*, diameters of $w = \{4.64, 5.82, 6.98, 8.14, 9.30, 10.70\}$ mm were explored, and for *Arrays B* and *C*, $w = \{6.98, 9.30, 10.70\}$ mm were tested. *Array A* was used as a baseline to explore the effect of changing the dimple diameter and depth thoroughly, whereas *Arrays B* and *C* were used to investigate the effect of changing the actual layout of the dimples.

Once the acrylic base tubes were prepared, the latex membranes were manufactured. Thin latex sheets (thickness $t = 0.25$ mm and shear modulus $G = 577 \pm 32$ kPa) were cut into rectangles. The ends of the rectangles were glued together using rubber cement (Best Test) to form tubes with a diameter of 36.9 mm. The latex tubes were then stretched over the acrylic cylinders, and the ends were sealed with o-rings, as shown in Fig. 3-1(d). The ends of the acrylic base cylinder were capped, and one end was connected to vacuum pump (DOA-P704-AA, Gast). An electronic pressure control valve (QPV1, Proportion-Air, Inc.) controlled the pressure applied, Δp, inside the specimens.

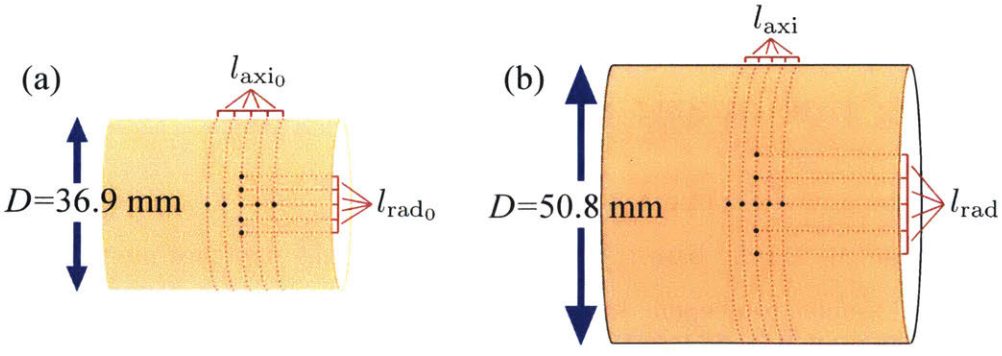


Figure 3-2: Procedure for measuring the prestretch in the membrane. (a) Schematic diagram of the latex film in the unstretched state, with dots in lines along the axial and radial directions. (b) Schematic of the latex film after it has been stretched over the acrylic base tube.

We measured the prestretch caused by the difference in radius of the membranes and acrylic base tube when no pressure was applied ($\Delta p = 0$). To do so, first, we drew dots on the unstretched latex tubes aligned in both the axial and radial directions. These dots were equally spaced, at distances of l_{axi_0} and l_{rad_0}, as shown in Fig. 3-2(a). When the latex membrane was stretched over the acrylic base tube, the new distances in the axial and radial directions were l_{axi} and l_{rad} respectively, as shown in Fig. 3-2(b). The prestretches were defined as

$$\lambda_{\text{axi}} = \frac{l_{\text{axi}}}{l_{\text{axi}_0}} \tag{3.1}$$

and

$$\lambda_{\text{rad}} = \frac{l_{\text{rad}}}{l_{\text{rad}_0}} \tag{3.2}$$

where $\lambda_{\text{axi}} = 0.87 \pm 0.02$ and $\lambda_{\text{rad}} = 1.38 \pm 0.01$ are the prestretch in the axial and radial directions, respectively. Similarly to the case of the grooved cylinders presented in Section 2.2.2, the radial prestretch ensured that there was no fluttering of the membrane during the wind tunnel experiments, that could otherwise have been caused by slack between the latex tube and the rigid acrylic skeleton.

3.3 Mechanics of deformation of the dimples during pneumatic actuation

Similar to the grooved specimens studied in Chapter 2, when a vacuum pressure is applied inside the acrylic base tube, the latex membrane stretches inward, thereby causing the dimples to deepen. In this section, we present the results of mechanical experiments designed to characterize how the shape of the dimples, specifically the dimple depth, d, depends on the applied pressure differential, Δp. This $d(\Delta p)$ dependence, will later be used in Section 3.4 to help interpret the results of the wind tunnel experiments.

3.3.1 Experimental procedure to study dimple deformation

Recall that, for the grooved specimens, a setup using a laser line oriented at 45° incident to the surface of the specimens was used, as described in Section 2.4. That setup could not be used for the dimpled cylinders since these specimens are a 3D structure that is not uniform in the axial direction. Instead, we used a 3D laser scanner (NextEngine 3D-scanner Ultra HD) to measure the surface shape.

The mechanical characterization experiments were performed by first setting the internal pressure in the specimens to a set value. The scanner was placed above, and oriented parallel to, the specimen, as shown in Fig. 3-3(a). The 3D-scans captured approximately one third of the circumference of the cylindrical specimens, which was sufficient for the purpose of determining the average dimple depth. The result of a representative 3D-scan on a specimen with *Array A*, dimple diameter $w = 9.30$ mm, and applied pressure $\Delta p = 20$ kPa, is shown in Fig. 3-3(b). The 3D-scan produced a point cloud with (x, y, z) coordinates.

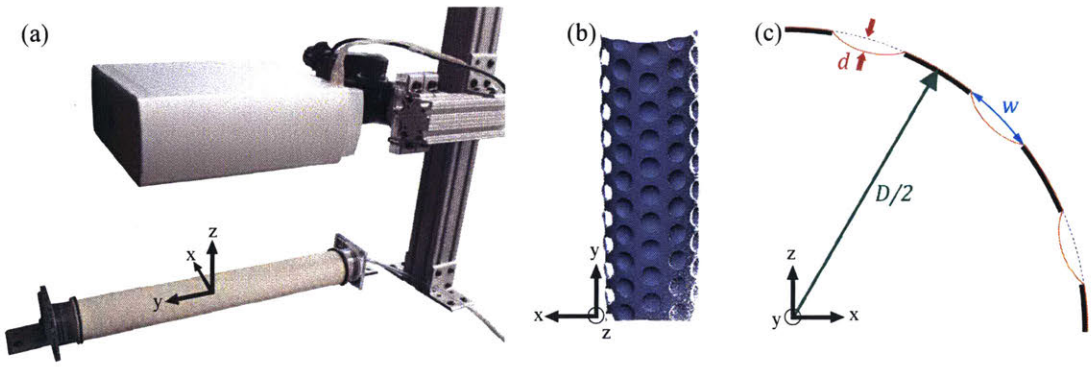


Figure 3-3: Summary of mechanical experiments to determine the dimple depth. (a) Experimental setup for 3D-scanning the surface profile of the dimpled specimens. (b) Resulting 3D point cloud from a 3D-scan of a specimen with *Array A*, $w = 9.30$ mm and $\Delta p = 20$ kPa. (c) Schematic defining the dimple depth d, dimple diameter w, and the cylinder diameter D.

We wrote Matlab code to extract the dimple depth from the 3D-scans. First, a circle was fit to the projection of all the data onto the xz-plane. This allowed us to shift the points such that the center of the fitted circle was located at (0,0), in the xz-plane. Next, all of the points were converted to polar coordinates with the

original y-axis aligned in the axial direction. Since the dimples were produced by laying a 2D array of circular holes onto the surface of a cylinder, we then converted the polar coordinates into a 2D array, with an index value equal to the value of the radial component. Using the `imfindcircles` Matlab function, we found the location of each dimple.

The dimple depth is defined relative to a smooth cylinder, as shown in the schematic diagram of Fig. 3-3(c). To compute the depth, we subtracted the minimum index value inside a circle from the median value just outside of that circle. This gave the depth of the dimple relative to the surface of the cylinder for a given dimple. The mean depth of all the dimples on a specimen, d, was considered the dimple depth for that specimen.

3.3.2 Dependence of the dimple deformation on the pneumatic actuation

The dependence of the dimple depth on the applied pressure is shown in Fig. 3-4, for specimens with the following values of dimple diameter: $w = \{4.64, 5.82, 6.98, 8.14, 9.30, 10.70\}$ mm. In the figure, the error bars on the data points correspond to the standard deviation of between 3 and 8 experiments with different specimens.

Focusing first on Fig 3-4(a), the dimple depth, d, is plotted as a function of the applied pressure, Δp. In the base state, with $\Delta p = 0$ kPa, there is a non-zero dimple depth for all of the specimens, the reason for which we explain next. Recall that the dimple depth, is defined relative to the smooth cylinder, as shown in Fig. 3-3(c). When the latex membrane is initially stretched over the body of the cylinder, the latex will cover the holes such that there is no curvature in the film. This means that a section of the circular cross section has been cut off by the membrane, and so even before any vacuum pressure is applied the specimens are not smooth cylinders. Since the dimple diameter acts as a chord length, when w/D is increased the sagitta grows. Based on our definition of d, the sagitta is equal to the initial dimple depth, d_0. Therefore, as w/D increases, so does d_0. The y-axis on the right side of the plot

in Fig. 3-4(a) shows the normalized dimple depth, $d^* = d/D$. In Section 3.4, we will use this normalized dimple depth when examining the aerodynamics.

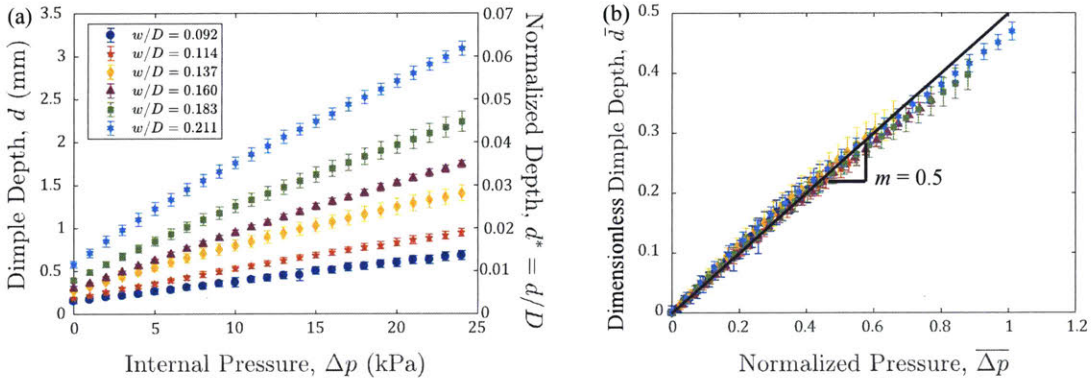


Figure 3-4: Dependence of the dimple depth on the internal pressure. (a) The dimple depth, d, as a function of the applied pressure for specimens with several different dimple diameters. (b) Collapse of the dimple depth data with a scaling based on the results of Cao *et al.* [143]. $\bar{d} = \frac{d'}{w/2}$ and $\overline{\Delta p} = \frac{\Delta p(w/2)}{\sigma_0 t}$ where σ_0 and t are the prestress, and thickness of the film.

In order to further study the mechanics of deformation of the dimples, we define a shifted dimple depth, $d' = d - d_0$, which, in the base state of $\Delta p = 0$, yields $d' = 0$. Aiming for a more general description of the data for specimens with different dimple diameters, we turned to similar problems found in literature. A study by Cao *et al.* [143] examined the delamination of a graphene film on a substrate. The delamination occurred at the edge of a circular blister that was being inflated [143]. Assuming the blisters were axi-symmetric, Cao *et al.* solved the governing differential equation for the deflection of a membrane to determine the shape of the blisters when they were inflated [143]. This process, yielded an analytical solution for the height, h, of a blister with known radius, a, being inflated with pressure, p.

$$h = \frac{pa^2}{4\sigma_0 t} - C_1\sqrt{\frac{D}{4\sigma_0 t}}\left[I_0\left(a\sqrt{\frac{\sigma_0 t}{D}}\right) - 1\right] \tag{3.3}$$

where σ_0 is the pre-stress in the membrane, t is the membrane thickness, D is the

bending stiffness of the film and

$$C_1 = \frac{pa}{2\sigma_0 t}\left[\frac{\frac{K_s a}{D}+\nu+1}{\left(\frac{K_s a}{D}+\nu+1\right) I_1\left(a\sqrt{\frac{\sigma_0 t}{D}}\right)+a\sqrt{\frac{\sigma_0 t}{D}} I_0\left(a\sqrt{\frac{\sigma_0 t}{D}}\right)}\right] \tag{3.4}$$

where K_s is the rotational stiffness of the film at the delamination front, and I_0 and I_1 are the modified Bessel functions of the first kind. Depending on the boundary conditions, the rotational stiffness can range from $K_s = 0$ (simply supported) to $K_s \to \infty$ (clamped). The prestress in the film ($\sigma_0 = 50$ kPa) was determined from the results of tensile tests presented in Fig. 2-6. The bending stiffness, D, was defined as

$$D = \frac{2G(1-\nu)t^3}{12(1-\nu^2)} \tag{3.5}$$

where $G = 577$ kPa is the shear modulus determined from the tensile tests, ν is Poisson's ratio and t is the thickness of the film. Assuming incompressibility ($\nu = 0.5$), which is appropriate for our elastomeric films, and using the initial thickness of the film ($t_0 = 0.254$ mm), we estimated the bending stiffness to be $D = 3.15 \times 10^{-6}$ Nm. We also assumed a fully clamped boundary condition, such that $K_s \to \infty$. Using the two extreme values for the diameters of the holes that we have considered for the design of our specimens ($a = 2.32$ and 5.35 mm), we computed the relative magnitude of the two terms in Eq.(3.3). We found that the first term was approximately an order of magnitude larger than the second, and thus determined that the depth of our dimples should scale as

$$\frac{2d'}{w} \propto \frac{\Delta p w}{2\sigma_0 t} \tag{3.6}$$

From now on, we shall refer to $\bar{d} = 2d'/w$ as the dimensionless dimple depth, and to $\overline{\Delta p} = \Delta p w/(2\sigma_0 t)$ as the dimensionless pressure. In Fig. 3-4(b), the above scaling of Eq.(3.6) is used to replot the raw data of Fig. 3-4(a), finding that the dimensionless dimple depth and pressure data collapse onto a single line. However, note that the slope of the collapsed data is 0.5, which is different from the analytical solution

that predicts a slope of 0.25, based on the first term of Eq.(3.3) [143]. The difference between our results and the analytical solution could be attributed to various factors. For example, we use the unstressed thickness of the membrane, t_0, to nondimensionalize the pressure. However, if we assume the latex is incompressible ($\lambda_{\text{rad}}\lambda_{\text{axi}}\lambda_{\text{t}} = 1$), then, using the values for λ_{rad} and λ_{axi} found in Section 3.2, we can calculate the prestretch through the thickness to be $\lambda_t = 0.84$. From this value of prestretch, we find that the thickness of the latex at $\Delta p = 0$ kPa is $t' = 0.213$ mm. Using t' instead of t_0, we find a slope of 0.41 for the slope of the curve in Fig. 3-4(b), which is closer to that of the analytical solution (0.25), but still significantly different. Additionally, we assumed that the boundary condition was clamped for our specimens, but if that is not accurate, K_s would be finite. While the exact prefactor of the analytical solution is not recovered for our experiments, the scaling presented in Eq.(3.6) does lead to an excellent collapse of the data, and this is all that was required to proceed to the wind tunnel experiments.

3.4 Wind tunnel experiments on fixed dimpled specimens

The results of the 3D-scan experiments provided an understanding of the dependence of the dimple depth on the internal pressure in the specimens. We proceed with wind tunnel experiments to characterize the aerodynamic performance of the dimpled cylindrical specimens. Specifically, we quantify how changing the depth, diameter and arrangement of the dimples can effect the dependence of the drag coefficient, C_{d}, on the Reynolds number of the flow, in the experimentally available range: $Re_{\text{min}} = 3 \times 10^4$ to $Re_{\text{max}} = 1.45 \times 10^5$.

The apparatus used for the wind tunnel experiments with the dimpled cylinders is the same as that to that used for the grooved specimens presented in Chapter 2, shown in Fig. 2-3(a). Similarly to the aerodynamics study on the grooved samples, we performed both *fixed* and *active* dimple experiments. In the *fixed* dimple experiments,

we measured the C_d across the full range of Re, while setting Δp to a fixed value, and thus a constant dimple depth. In the *active* dimple experiments, we varied Δp as the Re changed in order to achieve a desired dependence of C_d on Re. The remainder of this chapter will focus on the *fixed* dimple experiments, in which we explore the effect of different geometric parameters on the aerodynamic performance. Chapter 4 will focus on the *active* specimens.

3.4.1 Experimental protocol

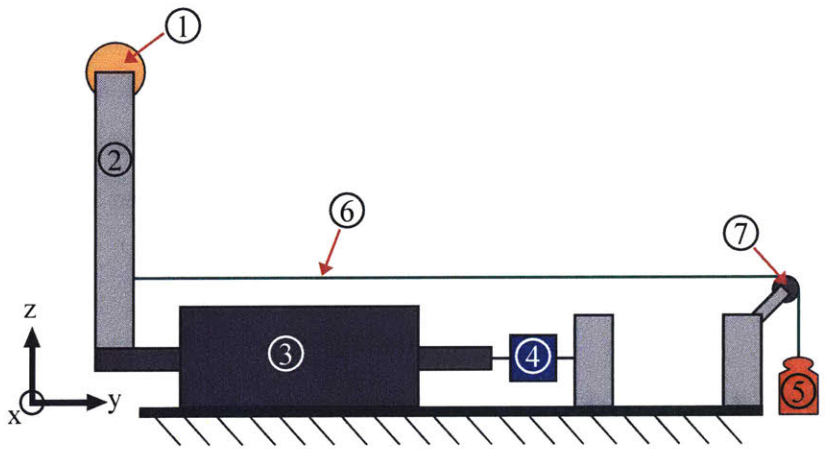


Figure 3-5: Schematic diagram of the setup used to calibrate the force sensor. The specimen (1), mounted to the top of the aluminum frame (2). The bottom of the aluminum frame is attached to one end of a linear air bearing (3), and the other end of the air bearing is connected to the load cell (4). A known calibration weight (5) applies a load to the aluminum frame via a nitinol wire (6) hung over a rotational air bearing (7).

Before each set of experiments, the force sensor was calibrated with a setup shown schematically in Fig. 3-5. First, the voltage signal from the force sensor was measured to establish a baseline. Then, one end of a nitinol wire was attached to the aluminum frame that held the specimen. The nitinol wire was hung over a rotational air bearing (acting as a frictionless pulley) and the other end of the wire was attached to a calibration weight, which was hung vertically. Using weights of 300, 600 and 900 g, the voltage from the force sensor was measured. We calculated the gravitational force

of the hanging weights, and performed a linear fit to determine the force as a function of the output voltage from the load cell.

In the fixed dimple experiments, the dimple diameter and type of array (*e.g. Array A*, or *B*, or *C*) was set by the specimen selected. The dimple depth for each specimen, on the other hand, could be gradually and systematically varied by the pneumatic actuation. For the results presented in this chapter, each experiment was performed by fixing the internal pressure in the specimen, and thus the dimple depth, as discussed in Section 3.3. For all of the specimens, the pressures tested were in the range $0 < \Delta p\,[\text{kPa}] < 24$, which yielded dimple depths in the range of $0.157 < d\,[\text{mm}] < 3.09$, depending on the diameter of the dimples, as shown in Fig. 3-4(a). In Section 3.3 we defined a dimensionless dimple depth, $\bar{d}$. However, a different parameter is more commonly used in literature [48,67,68,74] when describing dimple depth, $d^* = d/D$. The results from Section 3.3, allow us to readily convert from $\bar{d}$ to d^*, and for the remainder of this chapter we will refer to d^* as the normalized dimple depth. For this work we focus on the range $0.3 < d^*\,[\times 10^{-2}] < 4.5$.

With a fixed dimple depth, experiments were performed by slowly increasing the wind speed at a rate of $\dot{U} = 0.05\,\text{m/s}^2$ up to a maximum speed of $U = 47$ m/s. Blockage experiments similar to those presented in Section 2.5.1 yielded the same results with a blockage parameter $\epsilon = 0.3453$, as defined in Eq.(2.7). In these experiments, the blockage ratio was $\beta = 0.167$. We used the same procedure as that used for the grooved cylinders to calculate the drag coefficient according to Eqs.(2.6) and (2.7). With this process, each experiment produced the drag coefficient as a function of the Reynolds number ($C_\text{d}(Re)$) for a single dimple depth.

3.4.2 Effect of varying the dimple geometry on the drag coefficient

In this section, we study the effect on aerodynamic performance of two geometric parameters of the individual dimples: the normalized dimple depth, $d^* = d/D$, and the normalized dimple diameter, w/D. We performed all the wind tunnel experiments on

specimens with *Array A*, shown in Fig. 3-1(a). We made specimens with dimples of 6 different normalized dimple diameters, $w/D = \{0.091, 0.155, 0.137, 0.160, 0.183, 0.211\}$. Each panel in Fig. 3-6 shows experimental results of the drag coefficient as a function of the Reynolds number for a single specimen (*i.e.* a single w/D) with several different normalized dimple depths. The various symbols represent different values of the dimple size, and will remain consistent in subsequent figures. Each curve in Fig. 3-6 represents the average of 3 experiments with a single dimple depth, diameter, and array.

For each specimen, the dimple depth was changed by varying the pressure over the range, $0 \leq \Delta p$ [kPa] ≤ 24. The color bar on the right side of Fig. 3-6, maps the normalized dimple depth to different colors: blue and red represent shallower and deeper dimples, respectively. Even though the range of Δp was the same across specimens, the difference in dimple diameter led to a variation in the range of depth for each specimen. Since the diameter of the cylinder, D, is constant, this lead to a different range of d^* for each specimen. For example, Fig. 3-6(a) shows the results of experiments on a specimen with $w/D = 0.091$, which could achieve normalized dimple depths of $d^* = 0.3 \times 10^{-2}$ to 1.4×10^{-2}. Whereas the results shown in Fig. 3-6(f), are for the specimen with the largest dimples, $w/D = 0.211$, which could reach normalized dimple depths of $d^* = 1.2 \times 10^{-2}$ to 4.45×10^{-2}. This variation in the range of d^*, is captured visually by the different span of colors shown in each panel.

Focusing first on the results for the sample with the smallest dimples, $w/D = 0.091$, Fig. 3-6(a), we observe that for the shallowest dimples tested, $d^* = 3 \times 10^{-3}$ (the darkest blue), there is no sharp drop in drag coefficient that is indicative of the initiation of the drag crisis. For the deepest dimples, $d^* = 1.4 \times 10^{-2}$, the drag crisis begins at $Re \approx 5.4 \times 10^4$, and the critical Reynolds number (where the drag is minimized) is $Re^* = \{1.17 \pm 0.03\} \times 10^5$. Most of the dimple depths tested for this specimen exhibit a decreasing $C_\mathrm{d}(Re)$ up to the maximum experimental Reynolds number tested, Re_max. This indicates that, for those dimple depths, the specimen is still in the critical regime, thus $Re^* > Re_\mathrm{max}$. Even for the few depths large enough to observe the minimum drag coefficient, Re^* is close to Re_max, so we do not observe

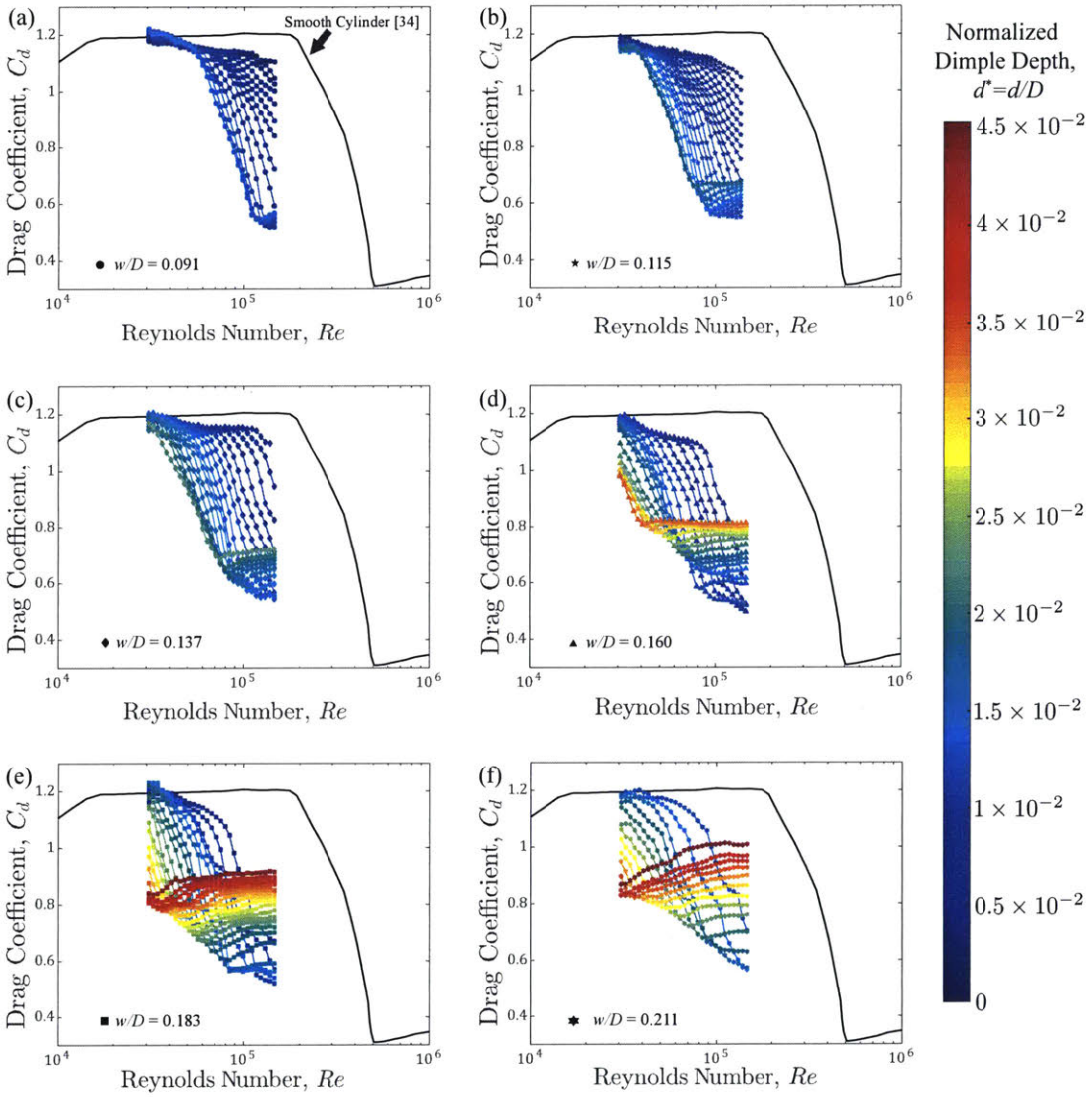


Figure 3-6: The effect of changing dimple size and depth on the dependence of drag coefficient, C_d, on the Reynolds number, Re. Each panel shows results for wind tunnel experiments on specimens with different dimple diameter to cylinder diameter ratios ($w/D = \{0.091, 0.115, 0.137, 0.160, 0.183, 0.211\}$ for samples (a - f), respectively). The colors represent the normalized dimple depth, $d^* = d/D$, as given by the adjacent color bar. The results shown are from experiments on specimens with dimples arranged in the hexagonal lattice, *Array A* shown in Fig. 3-1(a). The black lines are the results of experiments by Wieselsberger [34] on a smooth cylinder.

the behavior in the supercritical and transcritical regime.

The results of experiments on specimens with dimples sizes $w/D = 0.115$ and 0.137 are shown in Figs. 3-6(b) and (c), respectively. In these experiments, the shallowest dimples show the initiation of the drag crisis near $Re_{\max}$ ($Re \approx 1.2\times10^5$ and $Re \approx 1.1 \times 10^5$ for $w/D = 0.115$ and $w/D = 0.137$, respectively). For both of these specimens, even when the maximum pressure differential was applied ($\Delta p = 24\,\text{kPa}$) and the deepest dimples were attained, the initiation of the drag crisis (and a portion of the subcritical regime) can be observed in the experimental range of Reynolds number.

For the specimens with $w/D \geq 0.160$, the shallowest dimples yield results where large portions of the critical regime are observed. The results for the deepest dimples tested for each of these specimens, show none of the subcritical regime, even at the lower limit of experimental Reynolds number, $Re_{\min}$. The deepest and largest dimples, shown in Fig. 3-6(f) ($w/D = 0.211$ and $d^* = 4.45 \times 10^{-2}$), exhibit a monotonically increasing drag coefficient in the experimental range, which indicates that the critical Reynolds number is below $Re_{\min}$ ($Re^* < 3 \times 10^4$).

Looking at all of the data in Fig. 3-6, it is clear that each specimen spans a different portion of the (C_d, Re) space. The smaller dimples can maintain a higher C_d at high Re, while the larger dimples can reach lower C_d at low Re. For each specimen, we observe that, as the dimple depth is increased, the drag crisis occurs earlier and the minimum value of C_d increases. This is consistent with the results for previous studies on dimples [74, 75]. The details of this relationship will be discussed further in Section 3.4.3.

Above the critical Reynolds number, the different specimens exhibit a similar behavior. Using the data in Fig. 3-6(d) as an example, we can learn about the general aerodynamic behavior of the dimpled specimens in the supercritical regime. While the shallowest grooves do not show a critical Reynolds number, even at $Re_{\max}$, most of the dimple depths tested for this specimen do. For $Re > Re^*$, there is a slight increase in C_d, after which the value of C_d is nearly constant. This is in sharp contrast to the results for the grooves presented in Section 2.5.2, where we saw a

rapid increase in C_d after the minimum was reached. The results shown in Fig. 3-6(f) for the deepest dimples might initially seem in contrast to this leveling out of C_d. However, the finding is also in agreement with results from a previous study on dimpled spheres, which found that the rate at which C_d increased after the critical Reynolds number was higher for deeper dimple depths [74].

In Fig. 3-6, each panel represents a specimen with a different dimple diameter, tested at various dimple depths. Note that certain colors (and thus dimple depths), span similar portions of the (C_d, Re) space. This similarity between plots was the first indication that, across specimens, a given dimple depth may yield similar drag profiles. The effect of the dimple depth on $C_d(Re)$ can be more easily explored by grouping curves with similar d^* for different specimens.

Fig. 3-7 shows the dependence of the drag coefficient on the Reynolds number for different normalized dimple depths. The data plotted here is the same as that shown in Fig. 3-6, and represents experiments on specimens with *Array A* and six different sized dimples ($w/D = 0.091$ to 0.211). Each panel was plotted by selecting a normalized dimple depth ($d^* = \{0.5, 1.0, 1.6, 2.0, 2.4, 3.0, 3.4, 3.9\} \times 10^{-2}$, for Fig. 3-7(a-h), respectively) and finding experiments that were performed with a d^* within 5% of that value. The different symbols represent the different dimple diameters, and thus different specimens.

Focusing on Fig. 3-7(a), note that the two curves correspond to data obtained from experiments on specimens with $w/D = 0.091$ and 0.115. The specimens with larger dimples are not represented in this plot because, even when no pressure differential is applied, $d^* > 0.5 \times 10^{-2}$. This is because larger dimples cut off a larger portion of the circular cross section of the cylinder than smaller dimples, thus leading to a higher initial dimple depth, d_0, as discussed in Section 3.3.2. Not all specimens span the same range of d^*, and thus the different panels in Fig. 3-7 are populated with experimental results of different specimens.

Increasing the dimple depth to $d^* = 1.0 \times 10^{-2}$, Fig. 3-7(b) shows results from more specimens (all dimple diameters tested except $w/D = 0.211$). For the deepest dimples, $d^* = 3.9 \times 10^{-2}$ shown in Fig. 3-7(h), we only see results for the two specimens

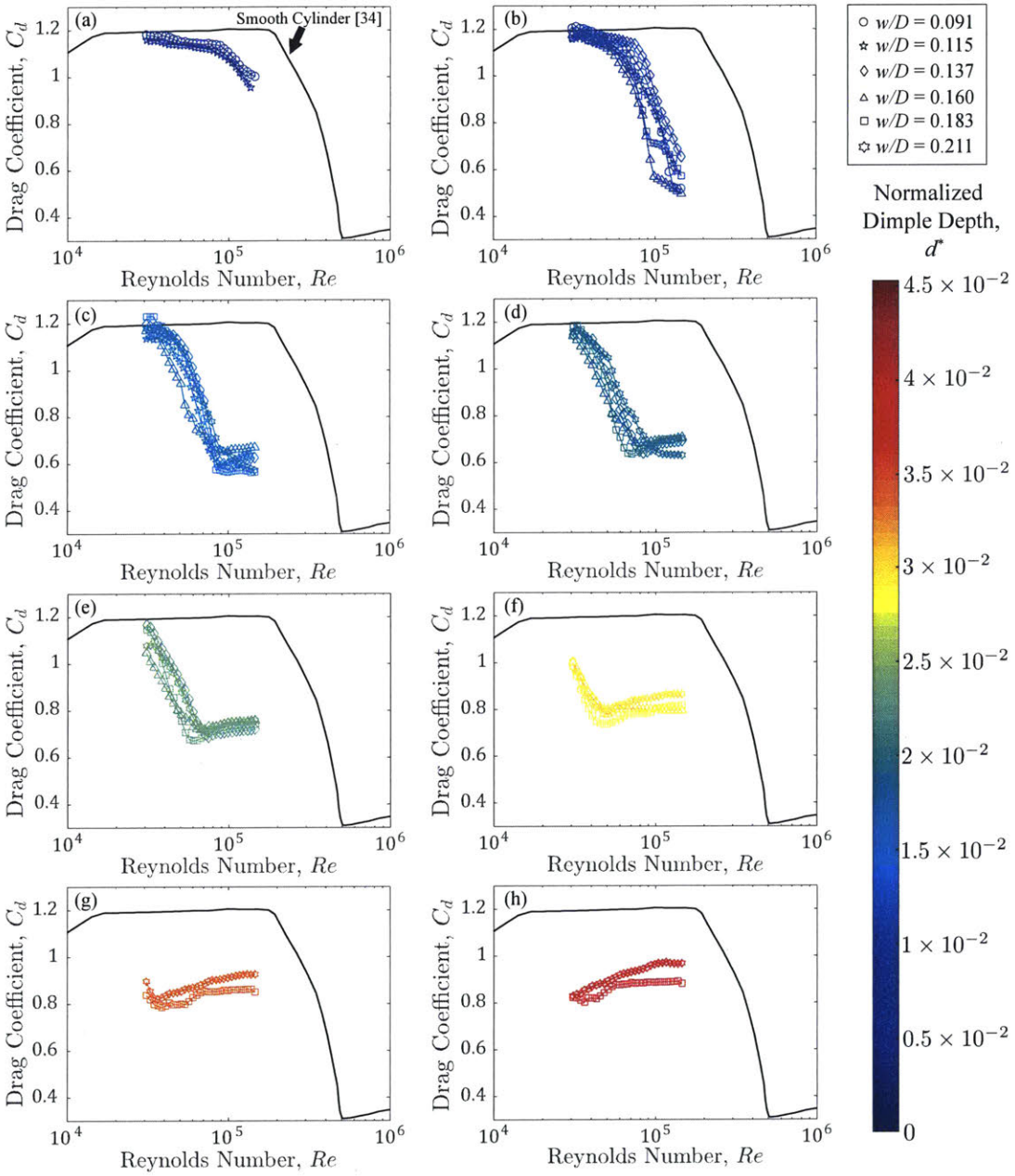


Figure 3-7: The effect of normalized dimple depth on the dependence of the drag coefficient, C_d, on the Reynolds number, Re. Each panel shows results for wind tunnel experiments with different normalized dimple depths, d^*. For panels (a-h) $d^* = \{0.5, 1.0, 1.6, 2.0, 2.4, 3.0, 3.4 \text{ and } 3.9 \pm 5\%\} \times 10^{-2}$, respectively. The different symbols represent specimens with different dimple diameter to cylinder diameter ratios ($0.091 \leq w/D \leq 0.211$). All specimens shown have dimples arranged in *Array A*. The black lines are the results of experiments by Wieselsberger on a smooth cylinder [34].

with the largest dimple diameter ($w/D = 0.183$ and 0.211). In each panel, different specimens with the same normalized dimple depth exhibit similar results. Therefore, for a given normalized dimple depth, $C_\mathrm{d}(Re)$ is independent of the dimple diameter, w/D. Additionally, from the differences between panels, we observe that changing the normalized dimple depth, causes the $C_\mathrm{d}(Re)$ to vary. From these observations, we can conclude that the aerodynamic drag performance is controlled by the depth of the dimples, and is independent of the dimple diameter.

For each dimple depth shown in Fig. 3-7, the results can be averaged across specimens with different diameters. For a given dimple depth, the mean and standard deviation of C_d for all specimens tested was calculated for each Re. Fig. 3-8 shows the average values of C_d and the shaded regions represent the standard deviation. When combining the results from all the different specimens, we show that we can span a larger region of the (C_d, Re) space than could be covered by any single specimen shown in Fig. 3-6. We also see that increasing the normalized dimple depth, d^*, causes the drag crisis to occur earlier, and the minimum drag coefficient to increase. Additionally, above the critical Reynolds number, the shallower dimples have a gradually increasing C_d, whereas the deeper dimples ($d^* = 3.9 \times 10^{-2}$) exhibit a steeper $C_\mathrm{d}(Re)$. This is in agreement with the work on dimpled spheres by Aoki *et al.* [74].

3.4.3 Effect of varying the array of dimples

In the previous section, we examined a single layout (*Array A*) for the arrangement of dimples, and varied the dimple diameter and depth. In this section, we study the effect of changing the arrangement of the dimples. Along with *Array A*, wind tunnel experiments were performed with *Arrays B* and *C*, shown schematically in Fig. 3-1(b) and (c), respectively. In the wind tunnel experiments on specimens with *Arrays A* and *B*, a row of holes was placed facing the flow such that the center of the dimples was at the stagnation point of the flow. Measuring from the stagnation point, this means that the centers of the rows were placed at $\theta = 0°$, $\pm 30°$, $\pm 60°$, $\pm 90°$, $\pm 120°$, $\pm 150°$ and $180°$ (along the circumferential direction), as shown in Fig. 3-1(d). Recall that, similarly to *Array A*, *Array C* also has a hexagonal lattice of dimples, however the rows are

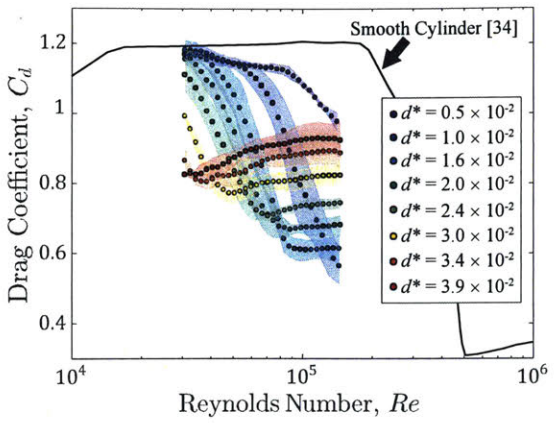


Figure 3-8: The relationship between the drag coefficient, C_d, and the Reynolds number, Re, for different normalized dimple depths. Each curve is the average of the $C_\mathrm{d}(Re)$ for specimens with different hole sizes and *Array A*. The shaded areas represent the standard deviation of the tests. The black line the result of experiments by Wieselsberger on a smooth cylinder [34].

oriented perpendicular to the axis of the cylinder, as shown in Fig. 3-1(c). This difference in orientation, effectively doubles the density of rows for *Array C* (dimples every $\theta = 15°$), but reduces the axial spacing of the dimples.

For these additional arrays, we performed experiments on specimens with dimple diameters, $w/D = 0.137$, 0.183 and 0.211. These specimens were tested using the same procedure as the specimens with *Array A*, and were oriented such that the center of a row of dimples would be at the stagnation point of the flow. The $C_\mathrm{d}(Re)$ curves from these experiments are shown in Fig. 3-9. All three arrays show that depending on the range of achievable dimple depths (set by varying the dimple diameter) different portions of the (C_d, Re) space are covered. Additionally, we see that for the same colors, and thus dimple depths, the $C_\mathrm{d}(Re)$ behavior is similar across specimens.

In Fig. 3-10, each panel shows the results of experiments performed with specimens having a normalized dimple depth, d^*, within 5% of the listed value (ranging from $1.38 \leq d^* \, [\times 10^{-2}] \leq 3.74$). The results from all 3 arrays are shown, thus we use color to indicate the array rather than the dimple depth. The green, purple and orange curves represent *Arrays A*, *B*, and *C*, respectively. Depths were only selected if each of the arrays had at least one experiment performed with a depth within 5% of that

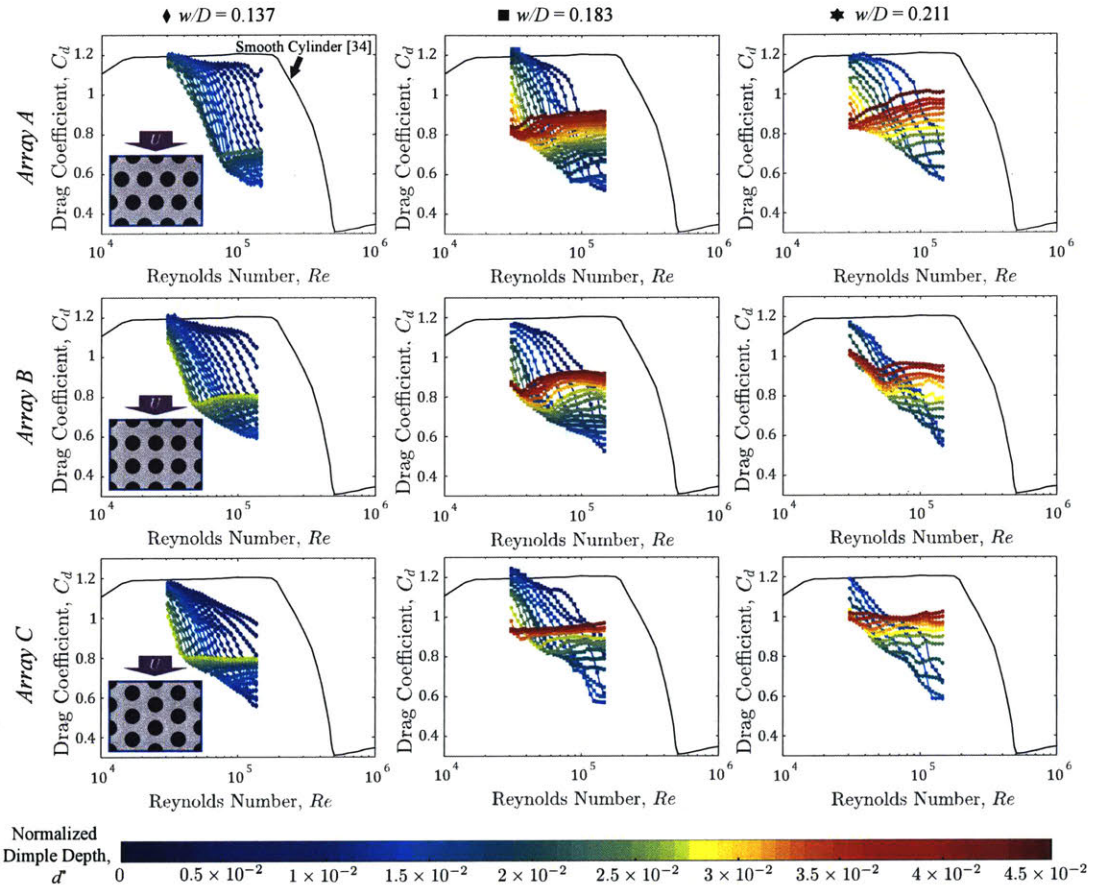


Figure 3-9: Results from wind tunnel experiments on specimens with 3 different arrays and three different dimple sizes (w/D = 0.137, 0.183 and 0.211). Each panel represents several experiments run at different dimple depths for a single specimen.

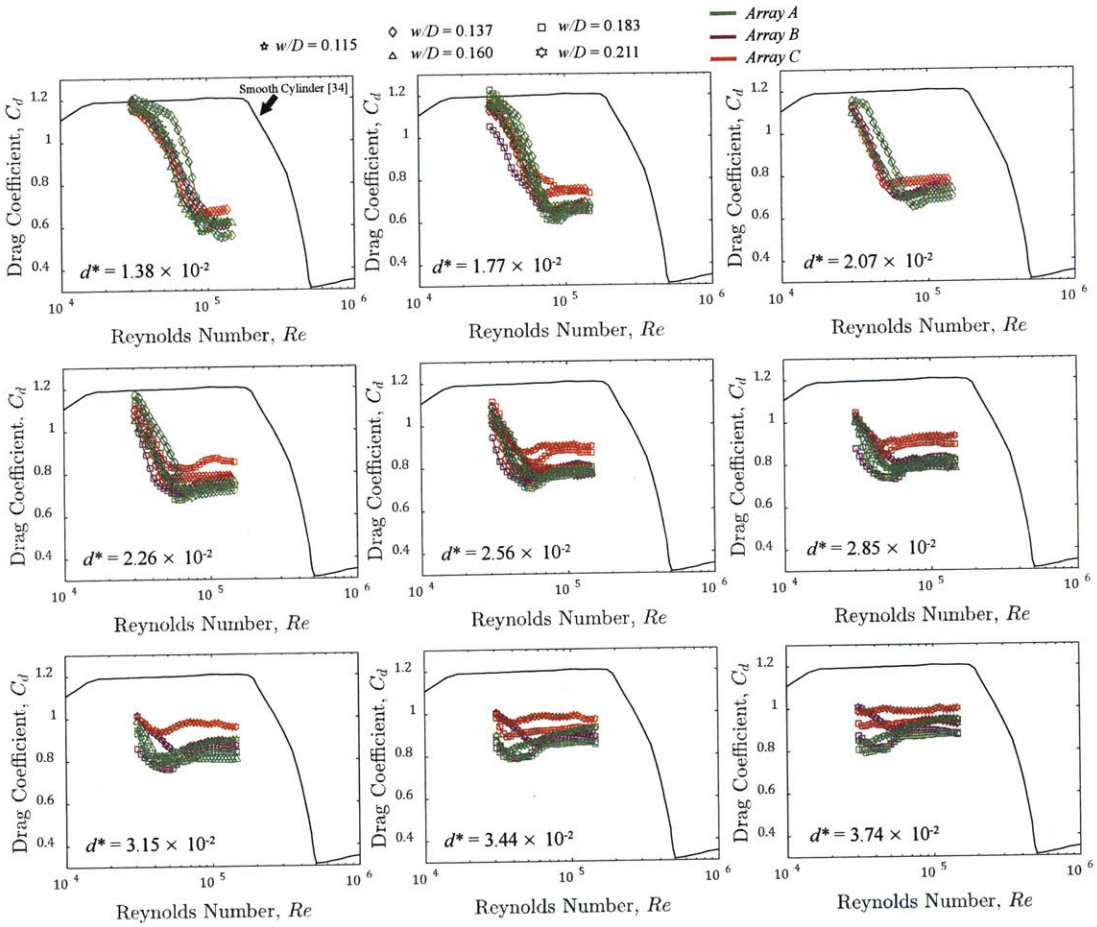


Figure 3-10: Results of wind tunnel experiments on specimens with 3 different arrays grouped by normalized dimple depth, d^*. Each panel contains the results of experiments on different specimens with the same dimple depth. The symbols represent different diameters, and the different colors represent different arrays.

value. Again, the symbols represent different dimple diameters. Note that there are more curves for *Array A*, since there were more dimple diameters tested for that array.

For a given array and depth, the results with different dimple diameters, yield similar results. This is shown by the matching results for a given color in each pane. Additionally, for a given d^*, before the drag crisis and during the critical regime, the results are independent of the type of array. After the critical Reynolds number, the results for *Arrays A* and *B* are similar for a given d^*. However, near the critical Reynolds number and beyond, *Array C* has consistently higher drag coefficients than either *Array A* or *B*. While we have not performed flow visualization to explore why

this deviation in behavior occurs, we speculate that it may be caused by the different locations of the rows of dimples. Recall that *Array C* has effectively twice the density of rows of dimples because of the orientation of the array. We can quantify the differences between these arrays, by studying the data around the critical Reynolds number.

We found the critical Reynolds number, Re^*, and the corresponding minimum drag coefficient, C_d^*, for each specimen, shown in Fig. 3-11. Recall that the critical Reynolds number was defined as the Reynolds number at which the drag coefficient reaches its minimum during the drag crisis (see Section 2.5.2). As before *Array A*, *B*, and *C* are shown in green, purple and orange, respectively. In the figure, the points with error bars are the mean values of specimens with different dimple sizes, w/D, but similar normalized dimple depths for a single array. The error bars represent the range of values for different specimens. The points without error bars represent a single specimen - there was only one specimen with that particular depth for the given array. Notice that there are more points with error bars for *Array A*, since specimens with more dimple diameters were tested for that array.

Fig. 3-11(a) shows Re^* as a function of the normalized dimple depth, for the three different arrays. For each specimen there is a monotonic decrease of the critical Reynolds number with increasing normalized dimple depth. This result is consistent with the results we found for groove depth in Section 2.5.2, and with previous results for surface roughness and dimples [41,68,73], that increasing the scale of the roughness or depth of the dimples caused the drag crisis to occur at a lower Reynolds number. Over most of the range of d^*, the three different arrays yield similar Re^* values.

Fig. 3-11(b) shows the drag coefficient at the critical Reynolds number, C_d^*, as a function of the normalized dimple depth, for the different arrays. A monotonic increase in C_d^* is observed with increasing d^*. Again, this trend is consistent with the results we observed for grooves in Section 2.5.2 and with previous literature results on surface roughness and dimples [41,68,73]. Both *Arrays A* and *B* have very similar critical drag coefficients, whereas *Array C* has a higher C_d^* for all normalized dimple depths. This is consistent with our earlier observation of Fig. 3-10, that after the

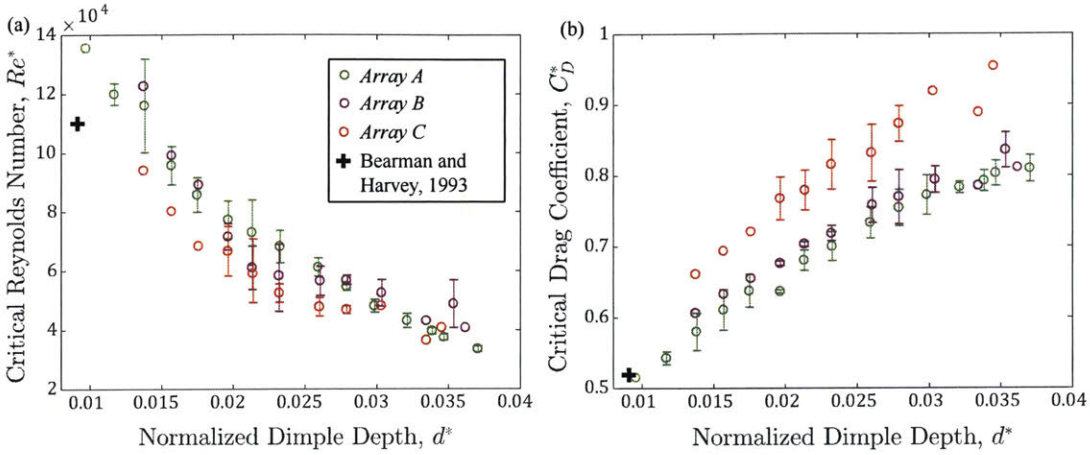


Figure 3-11: Dependence of the critical Reynolds number and critical drag coefficient on the normalized dimple depths for specimens with different arrays. (a) Critical Reynolds number, Re^*, as a function of the normalized dimple depth, d^*, for the different arrays. (b) Drag coefficient at the critical Reynolds number, C_{d}^*, as a function of d^* for the different arrays. In both plots, the error bars represent the maximum and minimum values from multiple specimens with the same array but different dimple sizes, w/D. The black + symbol in each panel represents results of experiments on dimpled cylinders by Bearman and Harvey [68].

critical regime, *Array C* has a higher C_{d}, than either *Arrays A* or *B*.

The black + symbols in Fig. 3-11 correspond to previous experimental results from Bearman and Harvey [68]. In their experiments, specimens with $d^* = 0.91 \times 10^{-2}$ and a hexagonal array similar to our *Array A* were used. The critical Reynolds number observed in their experiments is lower than we observed for dimples with similar depth, but the critical drag coefficient is nearly the same [68].

3.4.4 Comparison of drag profiles between non-uniform and uniform arrays

So far, we have studied different arrays of dimples by changing the location of the holes, but maintained a uniform distribution on the surface. Next, we study several non-uniform patterns. We introduce the non-uniformity by starting with the uniform *Array A*. As a reminder, the experiments are performed with a row of dimples aligned

with the central axis at the stagnation point ($\theta = 0°$). Rows of dimples are axially staggered and located symmetrically above and below the stagnation point at uniform increments, $\theta = \pm 30°$, $\pm 60°$ and $\pm 90°$, as shown in Fig. 3-12(a) with axes defined the same as in Fig. 3-1(d).

We introduced the non-uniformity by systematically removing rows, symmetrically about the stagnation point. It is important to maintain the symmetry of the system to minimize the lift forces, which we are not measuring. We first removed the row of dimples at the stagnation point, $\theta = 0°$ while keeping all the other dimples in *Array A* in the same locations. Subsequent experiments removed individual rows of dimples from the base *Array A* at $\theta = \pm 30°$, $\pm 60°$ and $\pm 90°$. The results of the wind tunnel tests on the non-uniform arrays and corresponding schematic diagrams are shown in Fig. 3-12(c – f). For comparison, we also show the results for the uniform *Array A* in Fig. 3-12(b).

Fig. 3-12(c) shows the results of removing the row of dimples at the stagnation point ($\theta = 0°$). The results appear to be similar to those of the uniform *Array A*. The shallowest dimples show a large portion of the drag crisis, but the experimental range of Re does not go high enough to observe the critical Reynolds number. As the dimple depth is increased, the drag crisis occurs earlier, and Re^* decreases while C_d^* increases. For the deepest dimple depths, the critical Reynolds number remains below the lower bound of the experimental range of Reynolds number, Re_{min}, and the drag coefficient increases monotonically with increasing Re. Overall, there seems to be very little effect of the non-uniformity introduced by removing the dimples at the stagnation point.

The results of removing the next two rows of dimples closest to the stagnation point, at $\theta = \pm 30°$, are shown in Fig. 3-12(d). For the shallower dimple depths the results of this array are similar to those of the uniform *Array A*. For the deeper dimples, at the lower range of Re the C_d decreases slowly with increasing Re, then begins to grow. The gradual decrease in C_d is different from the traditional steep decrease associated with the drag crisis. Despite these differences, the overall results for this array yield markedly similar results to those of the uniform distribution.

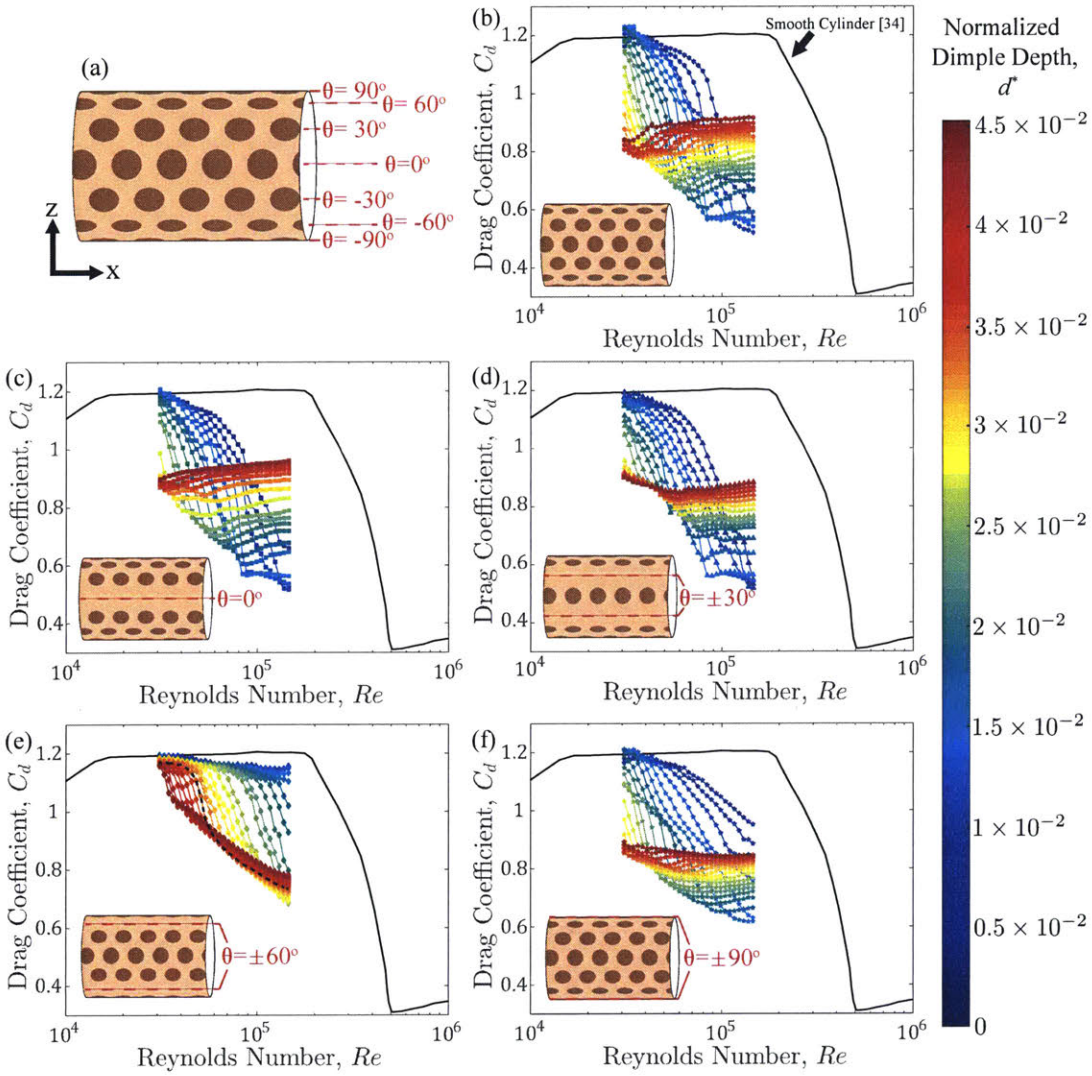


Figure 3-12: Dependence of the drag coefficient on the Reynolds number for non-uniform arrays. (a) Schematic of a section of the uniform Array A used as the base structure for introducing non-uniformity. This is viewed from the upwind side of the specimen, and $\theta = 0$ represents the stagnation point of the flow. (b) Results from wind tunnel experiments for specimens with no rows missing. (c-f) Results for experiments with rows missing symmetrically about the stagnation point at $\theta =$ 0, $\pm 30°$, $\pm 60°$ and $\pm 90°$, (c)-(f) respectively. The black dotted line in (e) highlights the results for $d^* = 3.5 \times 10^{-2}$

When the dimples located at $\theta = \pm 60°$ are removed, the differences in the aerodynamic performance are significantly more pronounced, as shown in Fig. 3-12(e). For all the dimples with $d^* < 1.7 \times 10^{-2}$ the drag crisis is not observed over the entire experimental range of Re. At $d^* = 1.7 \times 10^{-2}$, the drag crisis is initiated near the upper range of the experimental Re. As with other specimens, increasing the dimple depth causes the drag crisis to occur earlier. However, a different behavior of the drag crisis is seen. The black dashed line highlights the results when the normalized dimple depth was $d^* = 3.5 \times 10^{-2}$, and is representative of the $C_d(Re)$ behavior for other dimple depths. At the lower Re the specimen is clearly in the subcritical regime, then at the initiation of the drag crisis the drag coefficient drops steeply. After the initial steep drop, the C_d continues to decrease, but more gradually. This trend was not observed in other specimens.

The results of experiments on specimens with the dimples at the top and bottom of the cylinder missing ($\theta = \pm 90°$), are shown in Fig. 3-12(f). For the shallowest dimples, the drag crisis appears to be much more gradual than for the uniform array, and at the upper limit of the experimental range of Re, the C_d value is higher than that of the uniform specimen. However, as the dimples get deeper the results appear more similar to those of the uniform array.

Since the dimple diameter is the same for each of the specimens presented in this section, the range of attainable normalized dimple depth, d^* is identical. In the previous section, we found that the dimple depth controlled $C_d(Re)$. Those two observations suggest, that the same portion of the (C_d, Re) space is covered for each of the samples presented in this section. However, the introduction of certain non-uniformity, in particular removing the rows at $\theta \geq \pm 60°$, can cause different aerodynamic drag performance across samples with the same d^*.

We can more directly compare the results of the different non-uniform arrays by grouping them by normalized dimple depth. Fig 3-13 shows the results of experiments performed with the different specimens grouped by normalized dimple depth, d^*. Each panel shows results of experiments with the normalized dimple depths within 5% of the selected value ($d^* = \{0.96, 1.32, 1.48, 1.87, 2.19, 2.46, 3.05 \text{ and } 3.74\} \times 10^{-2}$ for

(a-h), respectively). Each of the different symbols represent a different array and the same symbols are used as in Fig. 3-12(b-f).

For the shallowest dimples shown, Fig. 3-13(a), the lower end of the experimental range of Re shows all of the specimens in the subcritical regime with approximately the same C_d. Around $Re = 5.3 \times 10^4$, the drag coefficient for all the specimens, except that with the missing rows at $\theta = \pm 60°$, begins to decrease. For the specimens with the uniform array, and the missing rows nearest to the stagnation point ($\theta =$ 0° and $\pm$ 30°) the results are similar and show the usual steep drop in C_d associated with the critical regime of the drag crisis. For the specimen with the missing rows at the top and bottom of the cylinder ($\theta = \pm 90°$), the C_d does decline, however the drop is more gradual than for the other specimens. The specimen with the row missing at $\theta = \pm 60°$, shown with the diamonds, appears to be in the subcritical regime over the entire experimental range of Re.

As we increase d^*, the results of the uniform and the non-uniform arrays with the rows missing near the stagnation point continue to show similar results. The results of the array with dimples missing on the top and bottom also appear to move closer to those of the uniform array until around $d^* = 1.87 \times 10^{-2}$ where they are nearly the same, as shown in Fig. 3-13(d). At this normalized dimple depth, the drag crisis appears near the upper range of experimental Re for the specimen with the rows missing at $\theta = \pm 60°$.

For each specimen, increasing the normalized dimple depth causes the drag crisis to occur earlier. For the four specimens other than that with the missing rows at $\theta = \pm 60°$, the results are similar for the higher dimple depths ($d^* \geq 1.87 \times 10^{-2}$). Eventually, for a deep enough dimple depth the drag coefficient of the specimen with missing rows at $\theta = \pm 60°$ drops below that of the other three specimens at high Reynolds numbers, as shown in Fig. 3-13(f – h).

In summary, from all the results in this section, we find that, while all the tested specimens span the same range of d^*, the introduction of a non-uniform array caused variations in the aerodynamic performance. When the missing rows were near the stagnation point ($\theta \leq \pm 30°$), the $C_d(Re)$ behavior was similar to that of a uni-

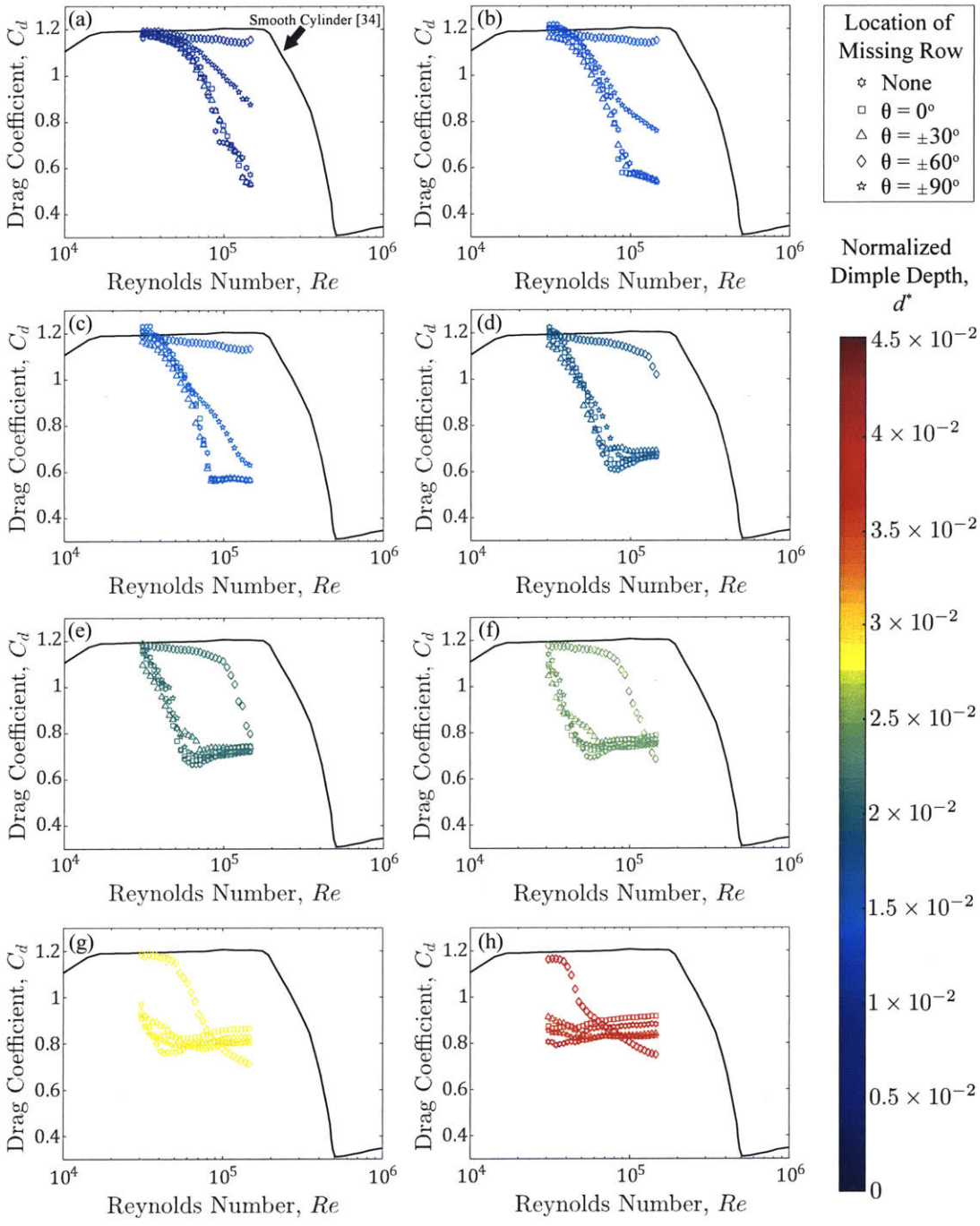


Figure 3-13: The effect of normalized dimple depth, d^*, on the aerodynamic performance of specimens with various non-uniform arrays. Each panel shows the results of multiples specimens with different non-uniform arrays at the same $d^* \pm 5\%$. Each symbol corresponds to a different array.

form array. However, when the missing rows were further from the stagnation point ($\theta \geq \pm 60°$) the aerodynamic performance is modified considerably. In particular, the specimen with the missing rows at $\theta = \pm 60°$ showed a significantly different behavior than that of the other four specimens. We suspect that this modification in behavior is because the missing row is nearest to the natural separation point of a smooth cylinder in the subcritical regime (at around 80° [29]). However, without data about the flow field around the cylinder this is still just a hypothesis. As such, we suggest that follow-up experiments with flow visualization be performed to study the underlying mechanism causing this phenomenon.

3.5 Conclusions

In this chapter, we explored the aerodynamic performance of cylindrical specimens with tunable dimpled surfaces. The specimens comprise a latex membrane stretched over an acrylic base tube with an array of circular holes cut into it. We performed mechanical experiments with a 3D-scanner to determine the relationship between the applied pressure differential, Δp, and the dimple depth. Based on an analytical solution from Cao *et al.* [143], we collapse the data for specimens with different dimple diameters. For the aerodynamics experiments, we used a normalized dimple depth, d^*, so the experiments on dimpled cylinders could be more easily compared to the results for smooth cylinders.

Having characterized the relationship between d^* and Δp, we ran wind tunnel experiments with the dimpled specimens. To study the effect of the diameter of the dimples, we ran experiments on specimens with the same array (*Array A*, which had a hexagonal distribution of dimples with rows aligned parallel to the cylindrical axis) but different dimple diameters (w/D). For each specimen, experiments were performed with numerous d^* values. We found that the normalized dimple depth was the primary parameter that controlled the dependence of C_d on Re, independently of the dimple diameter.

Additionally, we performed experiments on samples with different uniform arrays

(*Arrays B*, a square array of dimples, and *Array C*, a hexagonal array of dimples with rows aligned perpendicular to the cylindrical axis). We found that, in the critical regime, the three different arrays all yielded similar results. However, above the critical Reynolds number, *Array C* had a higher drag than both *Arrays A* and *B*.

We also explored several non-uniform arrays, in which rows of dimples from *Array A* were removed. We found that, while none of the non-uniform specimens yielded the same results as the uniform array, the performance of the specimens with the rows of dimples missing at $\theta = 0$ and $\pm 30°$ did not differ greatly from the uniform array. However, when the rows of dimples at $\theta = \pm 60°$ and $\pm 90°$ were removed, the specimens showed markedly different behavior from the uniform array. We suspect this variation in aerodynamic performance is caused by the close proximity of the removed dimples to the natural separation point of a smooth cylinder.

In this chapter, we performed a parametric study on the effect of the dimple diameter, depth, and distribution on the aerodynamic performance of dimpled cylindrical specimens. We used our ability to actively change surface shape to run experiments on a single specimen at several different dimple depths. During each individual experiment, the dimple depth was fixed for all Reynolds numbers. In the next chapter, we present experiments in which we control $C_d(Re)$ by actively modifying the surface shape as the Reynolds number changes.

THIS PAGE INTENTIONALLY LEFT BLANK

Chapter 4

Programmable aerodynamic drag control on dimpled cylinders

As we saw in Chapters 2 and 3, a sample with a static surface has a fixed drag coefficient, C_{d}, at a given Reynolds number, Re. As the Reynolds number is modified, *e.g.* by varying wind speed, the drag coefficient will also change.

In this chapter, we use tunable specimens, along with the results from Chapter 3, to actively modify the depth of the dimples in order to actively control $C_{\mathrm{d}}(Re)$. For this work, we focus on specimens with a hexagonal arrangement of dimples, with various dimple diameters. We use different specimens depending on the desired form of $C_{\mathrm{d}}(Re)$. In Section 4.1, we will demonstrate that the drag can be minimized over a wide range of Re, by modifying the depth of the dimples in a prescribed way as the wind speed changes. In Section 4.2, we show that we can attain several other functional forms of $C_{\mathrm{d}}(Re)$: constant, rapidly increasing and, rapidly decreasing. Finally, in Section 4.3, we discuss the limits of our particular system of controlling the drag profile, and present reasons why some specimens are better for certain purposes.

4.1 Minimizing drag by actively changing the dimple depth

As discussed in Section 3.4.3 and shown in Fig. 3-11, for a given fixed normalized dimple depth $d^{*\prime}$, the drag coefficient is minimized at the critical Reynolds number, $Re^{*\prime}$. Additionally, at $Re^{*\prime}$ all other dimple depths, d^*, yield a higher drag coefficient than $d^{*\prime}$. Therefore, to minimize the drag over the entire range of experimental Reynolds number in our experiments, we need a specimen for which $Re_{\min} \geq Re^* \geq Re_{\max}$.

Referring back to Fig. 3-6(a–d), we see that the specimens with $w/D = \{0.091, 0.115, 0.137, 0.160\}$ each achieve a low enough d^* to produce $Re^* \geq Re_{\max}$. However, these specimens do not produce deep enough dimples to exhibit $Re^* \leq Re_{\min}$. Therefore, these specimens were precluded from being used to minimize the drag coefficient. The specimen with $w/D = 0.183$, shown in Fig. 3-6(e) demonstrated Re^* in the entire range of experimental Reynolds number, so we used it to perform experiments in which we actively minimized C_d with changing Re.

To control the drag coefficient as the Reynolds number changed, we created an active control system. The steps of the control loop are shown in Fig. 4-1. First, the wind speed is recorded with the pitot tube and digital manometer, described in Section 2.2.1. The Reynolds number was then calculated. Given the Reynolds number, we determined the normalized dimple depth d^*, and applied pressure Δp, necessary to achieve the desired drag coefficient.

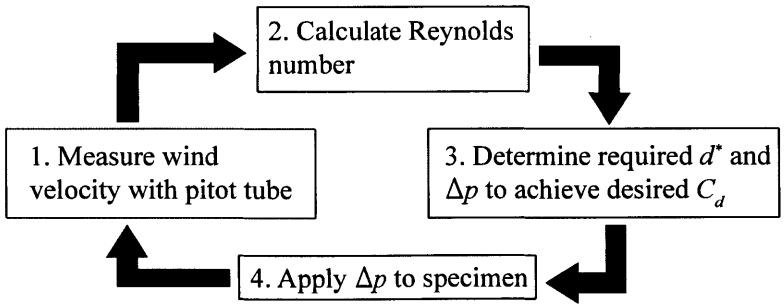


Figure 4-1: Schematic diagram of the procedure followed by the control loop in the active specimens.

While measuring wind speed and computing the Reynolds number are simple, determining the appropriate d^* to achieve a specified C_d is not. We first examined the results from the static experiments shown in Fig. 3-6(e). For a given Reynolds number, we determined which experiment (*i.e.*, which value of d^*) gave the lowest C_d. Since we are focusing on a single specimen, each d^* corresponds to a particular applied pressure, Δp. The squares in Fig. 4-2(a) show, for various Reynolds numbers, which d^* and Δp tested with a static experiment on the specimen with $w/D = 0.183$, yields the lowest drag coefficient. The colors corresponds to d^*, based on the color bar at the right side of the figure.

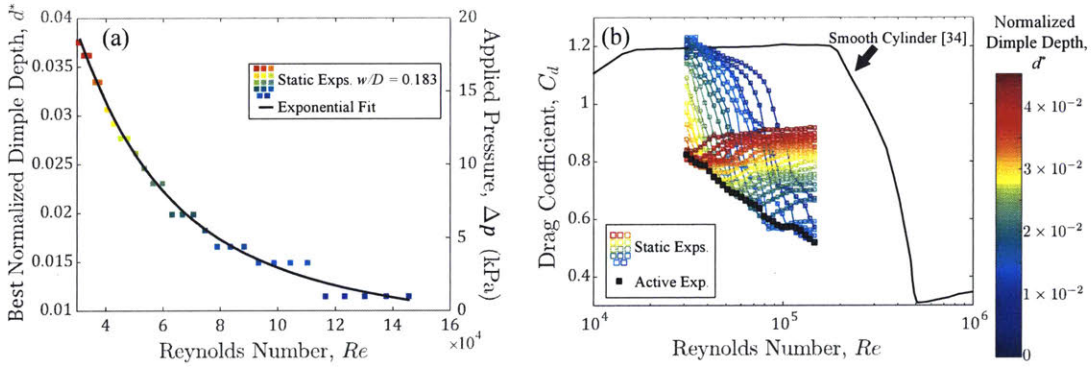


Figure 4-2: Actively minimizing the drag coefficient on a dimpled cylinder. (a) The static experiments for the specimen with *Array A* and $w/D = 0.183$ that produced the lowest C_d for various Re. Each color represents a normalized dimple depth and thus the applied pressure that produced the minimum C_d, as shown to the right. The black line is an exponential fit to the points following Eq.(4.3). (b) The results of both static experiments (colored squares) and active drag minimization experiments (black squares). The black line is results of a smooth cylinder from Wieselsberger [34].

The static results shown in Fig. 4-2(a) gave us an approximation of the normalized dimple depth that would minimize C_d for each Re. Because the static tests were performed at discrete depths, certain d^* values gave the lowest C_d at multiple Reynolds numbers (specifically those shown in Fig. 4-2(a) with multiple points for a single d^*). To account for the fact that untested depths might be optimal, we fit a continuous function to the data; the black line in Fig. 4-2(a) is this fit. We tried several different functional forms, and determined that the exponential function below provided an

excellent empirical description of the data.

$$d^* = 0.065e^{-3.42\times10^{-5}*Re} + 0.017e^{-3.15\times10^{-6}*Re} \tag{4.1}$$

This continuous function gives the value of d^* (and thus Δp based on the results from Section 3.3.2) that would minimize the drag coefficient for any given Re in the experimental range. Note that this function would not necessarily apply if the experimental range of Reynolds number were changed. However, it was an excellent fit to our data, which was sufficient for our purposes.

With the continuous function of Eq.(4.1) to describe the data at hand, all of the necessary ingredients of the control loop shown in Fig. 4-1 were established, and the system was implemented. In the wind tunnel experiments, we slowly increased the wind speed, as the active system continuously adjusted the pressure applied to the specimen, and the drag force was recorded. The results of these active experiments are shown with the solid black squares in Fig. 4-2(b), where the static results are shown with the open colored squares. The different colors correspond to different static dimple depths according to the adjacent color bar. The active system successfully provided a C_d near the minimum value observed in the static experiments over the entire range of Re.

4.2 Programmable drag by actively changing the dimple depth

Having successfully created a system that could adapt the shape of the surfaces to minimize the drag coefficient, we decided to explore the possibility of using the active system to program other functional dependences of the drag coefficient on the Reynolds number, $C_\mathrm{d}(Re)$. Specifically, we attempted to make $C_\mathrm{d}(Re)$ 1) constant, 2) rapidly increasing, and 3) rapidly decreasing. In this section, we utilize the active control loop system, introduced in Section 4.1, on a specimen with $w/D = 0.115$. This particular specimen was chosen because of the relative ease of precisely controlling

the dimple depth, compared to specimens with larger dimples, which will be discussed in detail in the next section.

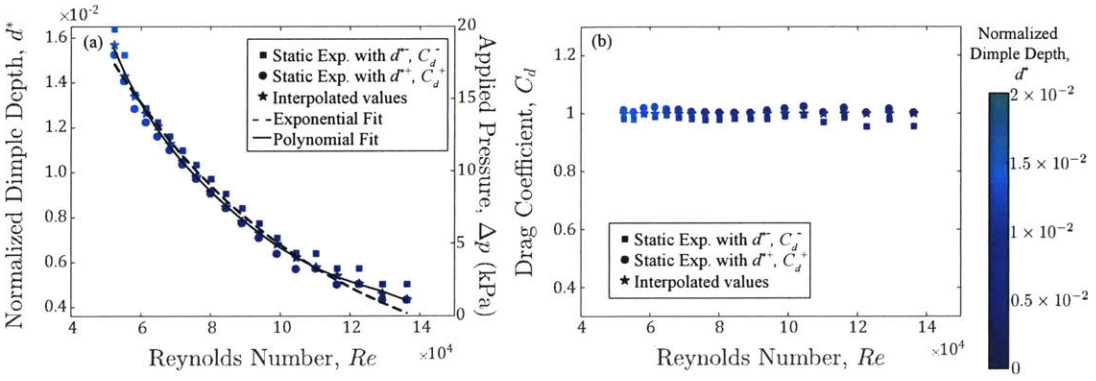


Figure 4-3: Process to actively maintain a constant $C_\mathrm{d} = 1.0$. (a) The normalized dimple depth, d^*, and applied pressure, Δp, required to achieve $C_\mathrm{d} = 1.0$, as a function of Re, for the specimen with $w/D = 0.115$. The squares and circles are results of static experiments and the stars are the interpolated results. The dashed and solid black lines are exponential and fifth order polynomial fits, respectively, to the interpolated results. (b) The results of static experiments that produced a C_d just above (circles) and just below (squares) the desired value of 1.0 (stars).

We first discuss the case in which we wanted to maintain $C_\mathrm{d} = 1.0$ for the range $5.24 \times 10^4 < Re < 1.37 \times 10^5$. For a given Re, we determined which static dimple depths gave the closest C_d both above and below $C_\mathrm{d} = 1.0$. In Fig. 4-3(b) the circles represent the static test with d^{*+} that produced the closest $C_\mathrm{d}^+ = C_d > 1.0$, and the squares represent the case with d^{*-} that yielded the closest $C_d^- = C_\mathrm{d} < 1.0$. The d^* values corresponding to each of these cases are plotted in Fig. 4-3(a) with the same symbols. We linearly interpolated between these two static experiments to determine the d^* (and thus Δp) value required to achieve $C_\mathrm{d} = 1.0$ at a given Re:

$$d^* = \frac{(1.0 - C_\mathrm{d}^+)(d^{*+} - d^{*-})}{C_\mathrm{d}^+ - C_\mathrm{d}^-} + d^{*+} \tag{4.2}$$

The interpolated d^* values are shown with the stars in Fig. 4-3(a). We initially followed a similar procedure to that used in Section 4.1, of fitting an exponential function to the interpolated results, as shown by the dashed black line in Fig. 4-3(a).

However, we observed that an exponential function did not fit this data very well, particularly at the lower and upper bounds of the experimental range of Reynolds number. In this work, the quality of the continuous functional fit to the data is only important in our experimental range of Reynolds number. We do not aim to make a prediction outside of this range, and therefore, any functional form that fits the interpolated data well can be used. After trying multiple functions, we determined that a fifth order polynomial (Eq.(4.3), with coefficients shown in the second row of Table 4.1) fit the data reasonably well, as shown with the solid black line in Fig. 4-3(a).

$$d^* = A(Re^5) + B(Re^4) + C(Re^3) + D(Re^2) + E(Re) + F \tag{4.3}$$

With the same specimen ($w/D = 0.115$), we also demonstrated the ability to maintain other constant drag coefficients, $C_\mathrm{d} = 0.9$ and 1.1. Fig. 4-4(a) shows the results of active experiments in which we attempted to maintain a constant $C_\mathrm{d} =$ 0.9, 1.0 and 1.1 with the orange, magenta and yellow stars, respectively. For each of these active experiments, the same procedure was followed as described above for $C_\mathrm{d} = 1.0$, and a fifth order polynomial was fit to the interpolated d^* versus Re data. The fitting process yielded the coefficients presented in Table 4.1, and the functions are plotted in Fig. 4-4(b).

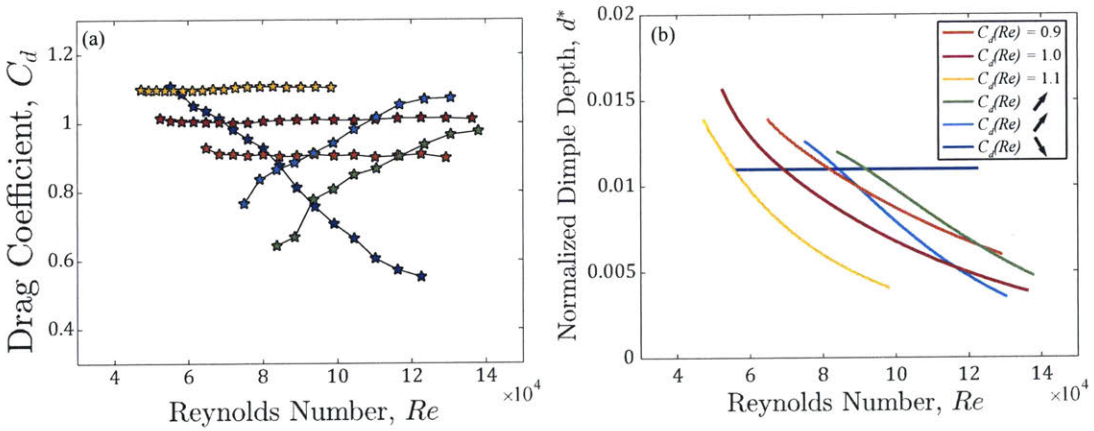


Figure 4-4: Experimental results of programming the drag coefficient. (a) The results of active experiments on a specimen with $w/D = 0.115$. (b) The normalized dimple depth, d^*, required to achieve the desired C_d.

	A	*B*	*C*	*D*	*E*	*F*
$C_d(Re) = 0.9$ —	-6.57×10^{-27}	3.37×10^{-21}	-6.89×10^{-16}	7.09×10^{-11}	-3.81×10^{-6}	9.89×10^{-2}
$C_d(Re) = 1.0$ —	-9.18×10^{-27}	4.52×10^{-21}	-8.83×10^{-16}	8.66×10^{-11}	-4.44×10^{-6}	1.07×10^{-1}
$C_d(Re) = 1.1$ —	-3.21×10^{-27}	1.54×10^{-21}	-3.11×10^{-16}	3.40×10^{-11}	-2.10×10^{-6}	6.32×10^{-2}
$C_d(Re)$ ↗ —	2.83×10^{-27}	-1.86×10^{-21}	4.90×10^{-16}	-6.41×10^{-11}	3.98×10^{-6}	-7.98×10^{-2}
$C_d(Re)$ ↗ —	6.88×10^{-27}	-4.07×10^{-21}	9.62×10^{-16}	-1.12×10^{-10}	6.21×10^{-6}	-1.16×10^{-1}
$C_d(Re)$ ↘ —	0	0	0	0	0	1.10×10^{-2}

Table 4.1: The coefficients of the polynomial Eq.(4.3) for the different active test cases plotted in Fig. 4-4(b).

At first, it appears that the higher order terms may not be necessary since, the coefficients are many orders of magnitude smaller than those of the lower order terms. However, since we are at high Reynolds number ($\mathcal{O}[10^5]$), the higher order terms are still relevant. For example, for the case with $C_\mathrm{d}(Re) = 1.0$, at the upper range of Reynolds number ($Re = 1.37 \times 10^5$), the terms in Eq.(4.3) corresponding to coefficients $A - F$ are $\{-0.443,\ 1.593,\ -2.270,\ 1.626,\ -0.609,\ \text{and}\ 0.107\}$, respectively. Note, that none of these terms are insignificant compared to the rest.

Achieving a rapidly decreasing C_d (shown with the dark blue stars in Fig. 4-4(a)) was straightforward. Because of the presence of the critical regime in the drag crisis of a static specimen, we simply maintained a constant dimple depth, as shown by the dark blue line in Fig. 4-4(b). However, creating a system with a rapidly increasing C_d, could not be achieved with the same, constant d^* strategy. This is because, even after the critical Reynolds number, the drag coefficient of dimpled specimens increases gradually, as described in Section 3.4.2. Following the methodology used to maintain a constant C_d – interpolating to find the required d^* and fitting a fifth order polynomial to the results – we were able to achieve a rapidly increasing $C_\mathrm{d}(Re)$, as shown by the green and light blue stars in Fig. 4-4(a). The coefficients are shown in Table 4.1, and the fits are plotted in Fig. 4-4(b).

In this section, we demonstrated a few specific forms of the $C_\mathrm{d}(Re)$ behavior that we achieved by actively modifying the dimple depth as the wind speed changed. However, the drag profiles that can be produced are not limited to the cases of a

constant, rapidly increasing or rapidly decreasing $C_d(Re)$. Following the methodology of determining a continuous function, $d^*(Re)$, which achieves a desired C_d, other forms of $C_d(Re)$ can be achieved. However, there are limits to this system, which are described in the following section.

4.3 Limitations on the active control mechanism

In the previous section, we reported on experiments with an actively changing surface to control the drag on a specimen with $w/D = 0.115$. With the maximum dimple depth, $d^* = 0.02$, the specimen exhibited subcritical behavior (*i.e.* high C_d) at Re_{min}. Therefore, at relatively low Reynolds numbers, the specimen with $w/D = 0.115$ could not reach drag coefficients less than $C_d = 1.2$. However, specimens with larger dimples, could exhibit lower drag coefficients at Re_{min}. Thus, we proceeded to explore the possibility of programming the drag coefficient on specimens with larger dimple diameters, to attempt to control the C_d in a wider range of Re.

Given the success of maintaining a constant C_d on the specimen with $w/D = 0.115$, we followed the same procedure presented in Section 4.2 to attempt to maintain a constant C_d on the specimen with slightly larger dimples, $w/D = 0.137$. The results of the attempt to maintain $C_d = 1.0$ in specimens with $w/D = 0.115$ and 0.137 are shown in Fig. 4-5(a) and (b) respectively.

In Fig. 4-5, we see that the drag coefficient differs from the desired $C_d = 1.0$ value significantly more for the specimen with $w/D = 0.137$ than for the one with $w/D = 0.115$. To understand this lack of precision control in the specimen with larger dimples, we first examined the d^* values required to maintain the constant $C_d = 1.0$ for each case.

To determine the d^* value required to achieve $C_d = 1.0$ for each Re, we followed the same interpolation procedure presented above in Section 4.2. Fig. 4-6(a) shows the normalized dimple depth required to produce $C_d = 1.0$ at various Reynolds numbers for the two different specimens. The star and diamond symbols represent the specimens with $w/D = 0.115$ and 0.137, respectively. The d^* values for the two spec-

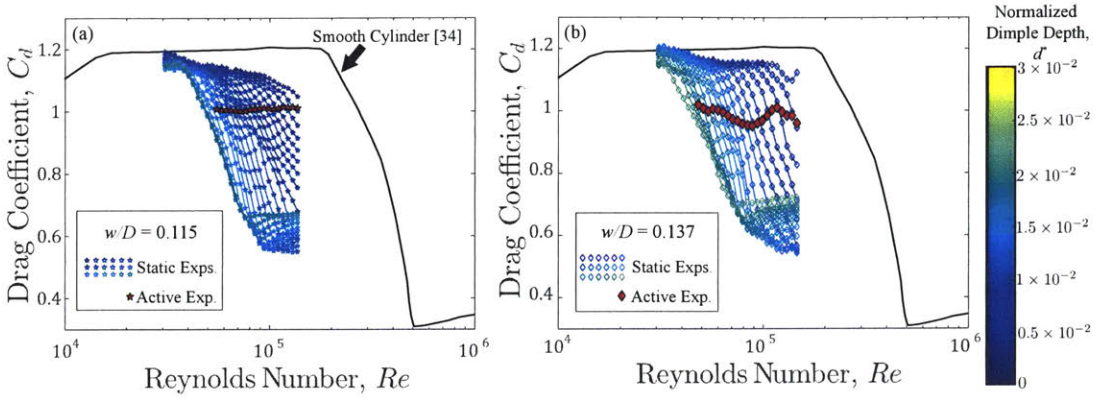


Figure 4-5: The results of active experiments attempting to maintain a constant $C_d = 1.0$ for specimens with $w/D = 0.115$ (a) and $w/D = 0.137$ (b). The black lines are results of a smooth cylinder from Wieselsberger [34].

imens are similar. This is consistent with the result of Section 3.4.2, that the dimple depth controls the drag.

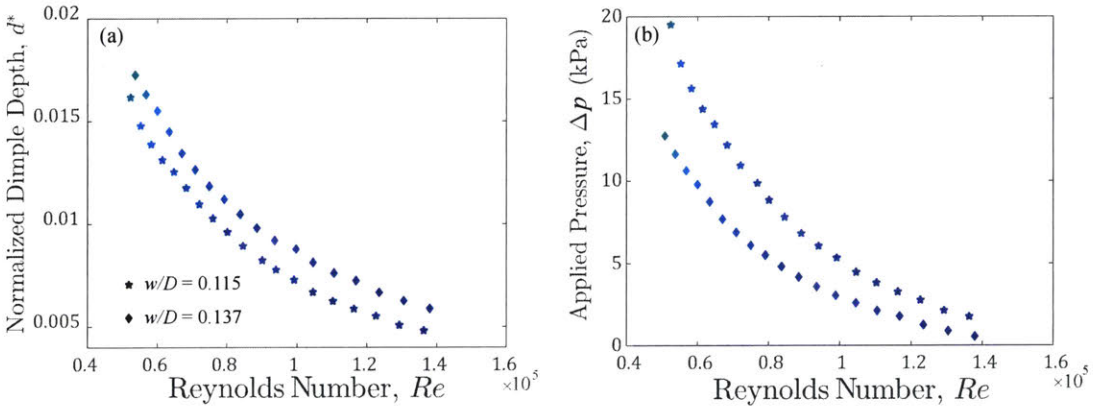


Figure 4-6: (a) The normalized dimple depth, d^*, required to maintain $C_\mathrm{d} = 1.0$ at various Reynolds numbers for specimens with $w/D = 0.115$ (stars) and $w/D = 0.137$ (diamonds). (b) The applied pressure required to achieve the d^* values shown in (a) for each specimen.

The depths required to maintain $C_\mathrm{d} = 1.0$ for each specimen are similar, but since the size of the dimples are different, the required Δp varies between specimens. Fig. 4-6(b) shows the Δp required to achieve $C_\mathrm{d} = 1.0$ over the experimental range of Re. At Re_min we can see that the specimen with $w/D = 0.115$ requires a $\Delta p \approx 20\,\mathrm{kPa}$ while the specimen with larger dimples, $w/D = 0.137$, requires $\Delta p \approx 13\,\mathrm{kPa}$. At Re_max, the

smaller and larger dimpled specimens require $\Delta p \approx 2$ and 1 kPa respectively. Therefore, in the specimen with smaller dimples, the pressure varies over about 18 kPa, whereas the range of required pressure when $w/D = 0.137$ is smaller (≈ 12 kPa). The larger span of Δp to achieve the same variation in d^*, suggests that the depth is less sensitive to changes in pressure for the specimen with smaller dimples.

This difference in sensitivity, can be visually understood by examining the variation in the static results presented in Fig. 4-5. For both specimens, the static curves represent results of experiments where the Δp values were increased incrementally by ≈ 1 kPa. In the critical regime, where $C_\mathrm{d} = 1.0$, we observe that the curves are closer together for the specimen with smaller dimples. Therefore, the same change in pressure results in a smaller change in drag profile for specimens with smaller dimples.

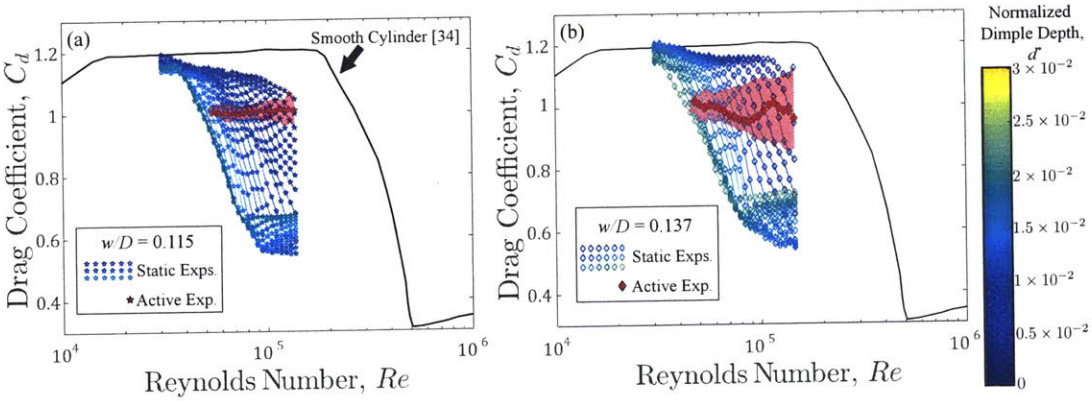


Figure 4-7: The effect of applying a pressure differential, Δp, 1kPa both higher and lower than the value that would produce $C_\mathrm{d} = 1.0$ for samples with $w/D = 0.115$(a) and $w/D = 0.137$(b).

Because of practical limitations on the pressure control, the actual Δp value applied to the specimens may not be exactly the same as that which the function calls for. The same amount of error in Δp will affect each specimen differently. At a given Re, the function outputs an applied pressure that would produce $C_\mathrm{d} = 1.0$, call this $\Delta p'$. To demonstrate the sensitivity to errors in Δp, we used the results of the static experiments to estimate, for a given Reynolds number, what the drag coefficient would be if there were an error in applied pressure of $\Delta p' \pm 1$ kPa. The shaded areas in Fig. 4-7(a) and (b) represent these results.

This increase in sensitivity with dimple diameter initially seems to contradict the finding in Section 4.1, where we were able to successfully minimize the drag on a specimen with even larger dimples, $w/D = 0.183$. However, when we follow the same procedure to study the sensitivity of the drag coefficient to errors in Δp, we get the result shown in Fig. 4-8.

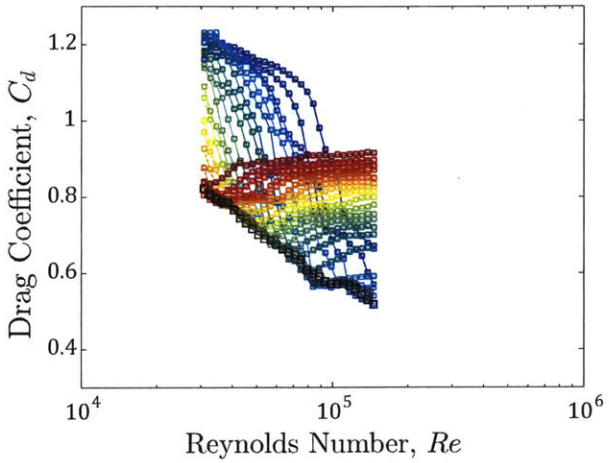


Figure 4-8: The effect of applying a pressure differential, Δp, 1 kPa both higher and lower than the value that determined from exponential fit in Section 4.1.

In Fig. 4-8, the black squares are the results of the drag minimization experiment, and the shaded black region represents range of C_d if the applied pressure was $\Delta p' \pm 1\,\mathrm{kPa}$. We find that the error is much smaller than either of the cases where we attempted to maintain a constant C_d. This is because, in the middle of the critical regime, the drag coefficient is very sensitive to changes in dimple depth, whereas near the critical Reynolds number (where the drag is minimized) the sensitivity is significantly smaller. Therefore, in practice, it is easier to minimize the drag coefficient than it is to maintain a constant C_d, if that value occurs in the critical regime.

4.4 Conclusions

In this chapter, we aimed to combine the results of the static experiments from Chapter 3 with the tunable nature of the surfaces to control the drag on dimpled

cylinders under changing flow conditions. We first attempted to minimize the drag over a range of Reynolds numbers. We approached this task by studying the static experiments to determine for each Re, which normalized dimple depth, d^*, gave the lowest drag coefficient. We fit a continuous exponential function to this discrete data, and created a control system, that modified the Δp value based on the wind speed to minimize the drag. This system was deployed in the wind tunnel experiments, and yielded a specimen with a low drag over a range of wind speeds.

Following a similar procedure, we showed that, with appropriate selection of specimens, we could program other various $C_{\mathrm{d}}(Re)$ behaviors, specifically; constant, rapidly increasing, and rapidly decreasing. However, we found experimental limitations preventing us from precisely controlling the C_{d}, particularly in specimens with larger dimples in the critical regime. It is important to note, that these are only practical limitations of our particular experiments. In principle, programming the drag coefficient by changing dimple depth can be done with large dimples. Perhaps all that is needed is a pressure regulator with more precise control. Another approach would be to use an active feedback control loop in which the drag coefficient is measured, and used as the input, and the applied pressure is modified accordingly.

Chapter 5

Aeroelastic deformation of a perforated strip

In this Chapter, we perform a combined experimental and numerical investigation on the static deformation of perforated elastic strips under uniform aerodynamic loading, at high Reynolds number conditions. The static shape of the porous strips is quantified as they are deformed by wind loading. The experimental profiles are compared to numerical simulations using a reduced model that takes into account the normal drag force on the deformed surface. We compute the drag coefficient of the strip by fitting the experimental data to the model.

The work in this chapter was done in close collaboration with Hussain Karimi (specifically implementing the numerical model presented in Sections 5.3 and 5.4) and Claudio Falcón (specifically, in much of the data analysis presented in Sections 5.6 and 5.7), and is outlined as follows. In Section 5.2, we describe the experimental setup and measurement techniques used to acquire data, which are then compared to the reduced model presented in Section 5.3. The experimental results on continuous strips (no porosity) are presented and discussed in Section 5.4. In Section 5.5, we characterize the effect of porosity on bending stiffness of the strips. The results of the aerodynamic experiments are presented in Section 5.6. In Section 5.7, we present and analyze the discrepancies between our experimental results in different loading configurations. Finally, in Sections 5.8 and 5.9, we discuss and conclude.

5.1 Introduction

While there have been numerous studies on independent effects of either porosity (discussed in Section 1.6) or flexibility (discussed in Section 1.5) on drag, there is a dearth of work that combines the two effects. A proxy to the effect of porosity on the drag coefficient of flexible structures has been studied in a reconfiguration experiment on what was called a 'poroelastic system', which involved experiments on spherical body with many flexible fibers extending radially outward [144]. It was found that the body as a whole had a Vogel exponent (defined in Section 1.5) $\mathcal{V} = -1$ rather than the previously found $\mathcal{V} = -2/3$ for independent slender structures [144]. This study combined flexibility and porosity by using several independent flexible bodies placed in close proximity to one another. More recently, a different study used numerical simulations to track the effect of porosity on the flapping dynamics of a 1D filament exposed to axial flow. It was discovered that both the flapping amplitude and flapping frequency drop when the porosity is above a critical level [145]. To our knowledge, there is a distinct lack of exploration on the combined effects of flexibility and porosity on the shape of statically deformed singular bodies in flow.

Here, we investigate the effect of both flexibility and porosity on the aerodynamic drag of rectangular elastic strips that are exposed to a uniform air flow, at high Reynolds numbers conditions. We make use of a combination of wind tunnel experiments and computer simulations using a reduced model. Moreover, we consider elastic strips with different material properties, over a wide range of porosities. The strips were studied in two different experimental configurations (horizontal and vertical clamping), as described in Fig. 5-1. The deformed profile of these flexible perforated specimens is experimentally measured and compared to the simulations. A restriction on the maximum deformation is imposed to validate the numerically generated profiles against experiments; namely, the maximum angle of deflection of the tip of the flexible strips is 45° with respect to the horizontal. Geometrically this means that, beyond this point, the tangential shear effects on drag are assumed to be no longer negligible. By comparing and fitting the experiments to the computed

profiles, we measure the drag coefficient C_d as a function of porosity for different velocities, bending stiffnesses and degrees of deformation. We found that the drag coefficient for perforated flexible strips decreased with increasing porosity, in a way that quantitatively parallels that of perforated rigid plates [120, 121] for the horizontally clamped configuration but not for the vertical configuration. Unexpectedly, we have found that the drag coefficient values for the vertically clamped configuration are smaller than those of the horizontal configuration, except for the solid strips where they coincide. Using this data, we also study the effect of porosity on the deformation of perforated strips by computing the drag coefficient as a function of the Cauchy number. In that regard, we find that for a given value of porosity, the drag coefficient remains constant as a function of Cauchy number for a large range of material properties and flow speeds.

5.2 Procedure of wind tunnel experiments to test perforated flexible strips

For all of the experiments reported in this chapter, we performed wind tunnel tests with flexible strips of different thicknesses and levels of porosity. Each strip was clamped to one of the walls of the test section of the horizontal wind tunnel, such that the face of the strip was set perpendicularly (and the thickness parallel) to the flow direction. We considered the two configurations shown in Figs. 5-1(a) and (d), with a strip that was either clamped vertically or horizontally exposed to horizontal flow, both of which will be described in detail below. For each strip, experiments were performed over a range of flow speeds. The deformed profile of the strip was measured by taking videos through a clear side wall of the test section of the wind tunnel. The sample strips were laser cut (Laser Pro, Spirit GLS) with width $w = 28$ mm, length $l = 275$ mm and thickness $0.242 \leq h\,[\text{mm}] \leq 0.508$ from Polyethylene terephthalate (PETG) or acetate sheets (mass densities $\rho \in [1280, 1330]\text{kg/m}^3$, respectively). One edge of each strip was painted fluorescent orange (Liquitex) to aid

with the visualization and subsequent image processing.

5.2.1 Details of wind tunnel used for experiments

Our experiments made use of an open return wind tunnel with a $100 \times 30.5 \times 30.5\,\mathrm{cm}^3$ test section capable of producing uniform steady flows with speeds in the range $2 < U\,[\mathrm{m/s}] < 34$, which are measured by a pitot tube and a high accuracy capacitance manometer (690A Baratron, MKS Instruments). This was the same wind tunnel used for the experiments presented in Chapters 2, 3, and 4. At the location of the clamps,

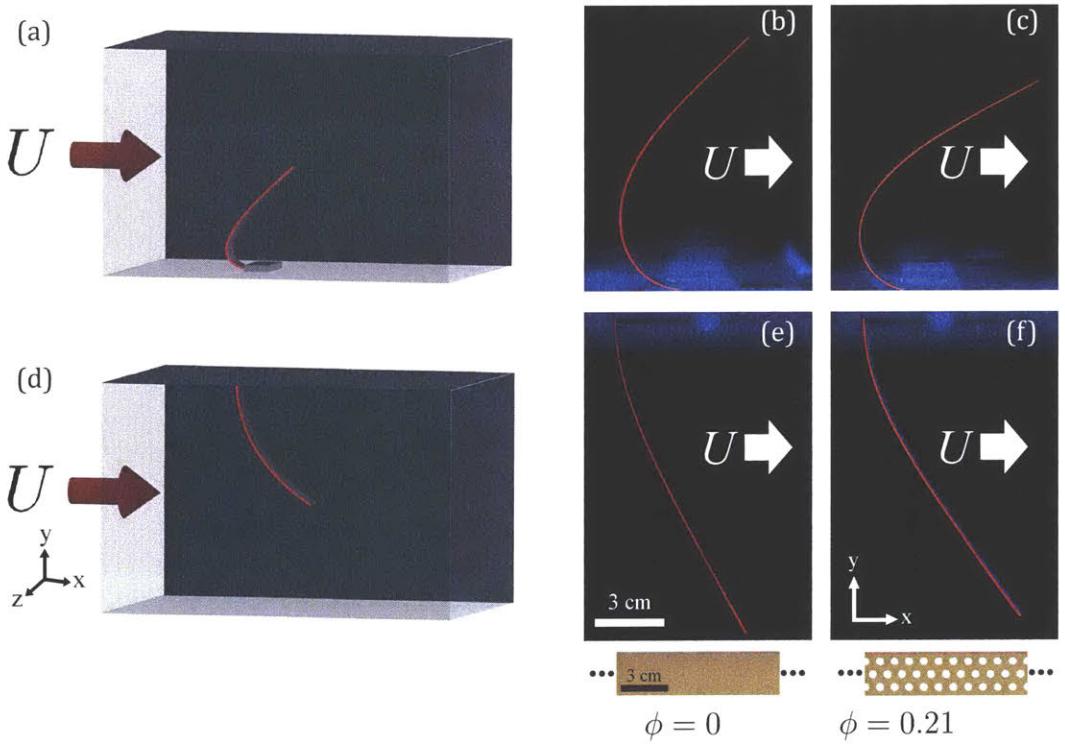


Figure 5-1: Setup of the wind tunnel experiments. (a-c) Horizontally clamped configuration. (d-f) Vertically clamped configuration. (a) and (d) Schematic diagram of the samples mounted in the wind tunnel. (b) and (c) representative still images in horizontally clamped configuration each at $U = 9.8\mathrm{m/s}$. (e) and (f) representative still images in vertically clamped configuration each at $U = 2.1\mathrm{m/s}$. (b) and (e) are the same sample with $\phi = 0$ and bending stiffness, $B = 0.0125$ Nm. (c) and (f) are the same sample with $\phi = 0.21$ and $B = 0.00602$ Nm.

the displacement thickness of the boundary layer is $\delta^* \approx 1.5\,\text{mm}$. In comparison to the length of the strips, the boundary layer is, therefore, small (approximately 1%). As such, we believe that neglecting the non-uniformity in the oncoming flow due to the presence of the boundary layer is appropriate. For all the values of U used in this study, the fluctuations of the wind speed were below 1% of the mean velocity. There was no need to consider blockage corrections since the maximum blockage (defined as the ratio of the projected area of the strip normal to the flow to the cross section of the wind tunnel) was always below 5%. The flow direction was aligned with the x-axis (see definition of the axes in Fig. 5-1(d)). The far-side wall and the ceiling (in the xy and xz-planes, respectively) of the test section were painted matte black in order to block as much of exterior light as possible, as well as minimize reflections. The near-side wall and floor (in the xy and xz-planes, respectively) were made of optically clear acrylic, as shown in the schematics of Fig. 5-1(a) and (d). An array of black lights was placed beneath the floor of the test section to make the orange paint on the edge of the strips fluoresce. A camera (D3200, Nikon) was placed 1.5 m away from the test section of the wind tunnel such that the edge of the strips could be captured through the near-side transparent wall.

5.2.2 Configurations of wind tunnel experiments

As noted above, two different configurations of the strips within the wind tunnel were studied. The first was similar to that of Ref. [110], albeit with a single strip in the current study, and will be referred to as the *horizontally clamped configuration*; see in Fig. 5-1(a)-(c). In this horizontally clamped case, the strip was placed flat at the center of the floor of the test section. An acrylic block was used to secure the downwind end of the strip to enforce a clamped boundary condition, while being aligned with the direction of the flow. Upon clamping, the total length of the strip that was free to deform was $L = 152.4\,\text{mm}$. Note that to obtain nontrivial (*i.e.*, deformed) configurations of the strip, it was required that the flow speed be set above a critical value such that the aerodynamic loading could support the self-weight of the strip [110].

The second configuration considered, shown in Fig. 5-1(d)-(f), will be referred as the *vertically clamped configuration.* In this case, the strips were exposed to the flow through a small slit on the ceiling of the test section, which also acted as a clamp by allowing the samples to be affixed vertically. A schematic of the clamping mechanism is shown in Fig. 5-2. First, a section of the ceiling of the wind tunnel was set on a linear track and was put in the open position (Fig. 5-2(a)) and the elastic strip was inserted (Fig. 5-2(b)). Through the thickness of the acrylic panels of the ceiling, on the sides making contact with the strips, thin latex sheets (0.1 mm thickness) were glued to increase the frictional contact between the clamp and the strip, so as to minimize sliding between the two, as shown in Fig. 5-2(a). The ceiling was then slid shut into the closed position and secured tightly to ensure the clamped boundary condition at the entrance to the wind tunnel; see Fig. 5-2(c). Since the ceiling of the wind tunnel was fixed horizontally, clamping the strips using the thickness of the wind tunnel ensures the strips were perpendicular to it, along the y-axis shown in Fig. 5-2. Note that, for visual clarity, the schematic in Fig. 5-2 only shows the ceiling of the wind tunnel and not its side walls.

Similarly to the horizontally clamped configuration, the total length of the clamped strip that was free to deform was $L = 152.4\,\text{mm}$. In both configurations (horizontal and vertical clamping), the painted edge of the strip faced the near-side wall of the extension and thus the camera. Illumination was reduced within the wind tunnel facility such that the effect of the black light on the fluorescent paint on the edge of the strip enhanced the contrast between the sample and the background. This process greatly simplified the extraction of the deformed profile of the strips, both in the horizontal and the vertical configurations.

5.2.3 Procedure for wind tunnel experiments

Each experiment was performed by first allowing the wind tunnel to reach a steady flow speed, U, whose value was recorded using the pitot tube. During the experiments, the strips were not perfectly steady, and instead had small amplitude unsteady oscillations. These oscillations are thought to be due to unsteadiness of the incoming flow

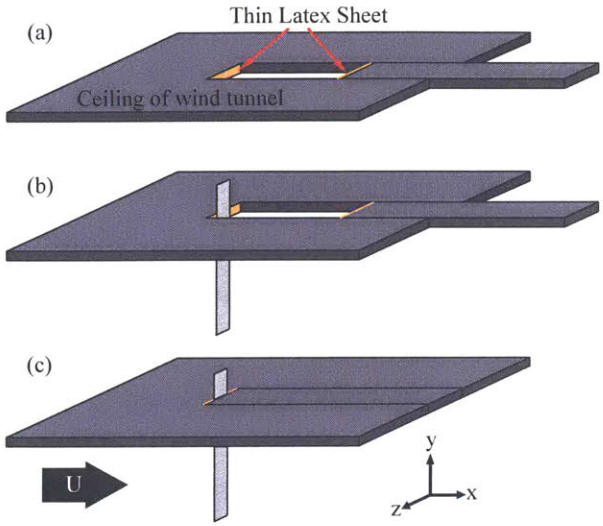


Figure 5-2: Schematic diagram of the clamping mechanism used for the vertical configuration. (a) Open position of the ceiling of the test section of the wind tunnel, with the thin films of latex glued to the through-thickness faces. (b) The strip is inserted into the open ceiling, perpendicularly to it. (c) The ceiling is closed onto the strip, thereby clamping the strip into a vertical configuration.

rather than resulting from aeroelastic fluttering [89]. The amplitude of oscillations was small compared to the level of deflection of the entire strip (the amplitude of the tip oscillation was smaller than 2 mm). Because of these oscillations, a single still image might not have captured the equilibrium position of the strip, so videos were taken instead. Each video was 10 seconds long and taken at 24 frames per second. The equilibrium position of the strip for a given velocity was determined using a custom image processing algorithm. Representative examples of the experimental deformation profiles obtained after this image processing are provided in Fig. 5-4 below (solid black lines).

5.3 Details of the numerical model

In Fig. 5-3(a), we present a schematic diagram of the geometry of the problem that we seek to model, along with the definition of several relevant quantities. To interpret the experimental data and rationalize the results, we use a reduced model based on

the classic Kirchhoff-Euler beam equations in the xy-plane, and take into account interaction between the elastic strip and the flow through an aerodynamic forcing term. In the absence of twist, and incurring uniform loading along the depth, the two-dimensional (in-plane) slender rod equations presented in Eqs. (5.1), below, describe the large deformation of the elastic strips under aerodynamic loading. As derived in Ref. [146], by considering the forces and torques acting on a differential element of a beam of width w, height h and length L, the local rate of change in linear and angular momentum, per unit length, and kinematics are

$$\rho_s w h \frac{\partial^2 \boldsymbol{r}}{\partial t^2} = \frac{\partial \boldsymbol{F}}{\partial s} + \boldsymbol{P} - (\rho_s g h w)\mathbf{e}_y, \tag{5.1a}$$

$$\frac{\rho_s w h^3}{12}\frac{\partial^2 \theta}{\partial t^2} = \frac{\partial M}{\partial s} + \boldsymbol{F}\cdot\hat{\mathbf{n}}, \tag{5.1b}$$

$$M = Bw\frac{\partial \theta}{\partial s}. \tag{5.1c}$$

In the schematic diagram of Fig. 5-3(a), we sketch the definitions of important variables in our problem: the local deflection angle, $\theta(s,t)$, which is a function of time t and arc length s; the local position vector, $\boldsymbol{r}(s,t)$; the tangential vector, $\hat{\mathbf{t}}$; and the normal vector $\hat{\mathbf{n}}$. Acting on the beam are the internal forces $\boldsymbol{F}(s,t)$, external load per unit length $\boldsymbol{P}(s,t)$ (and gravity) and internal moment $M(s,t)$. The material density of the strip is ρ_s and its bending stiffness is defined as $B = Eh^3/12(1-\nu^2)$ [147], where E is the Young's modulus, and ν is the Poisson's ratio. Eq. (5.1a) represents the local change in linear momentum due to the acting forces, Eq. (5.1b) represents changes in angular momentum due to moments about the local arc length s, and Eq. (5.1c) represents the local internal moment due to beam bending. Boundary conditions require $\theta = 0$ at the clamped end, $s = 0$, in addition to the absence of internal force $\boldsymbol{F} = 0$ and moment $M = 0$ at the free end, $s = L$. This last condition, when introduced into Eq. (5.1c) imposes the curvature restriction $\partial\theta/\partial s = 0$ at the free end.

In equilibrium, the fluid load acting on the strip balances its weight and the beam stands still in a deformed shape. Under these conditions, time derivatives vanish and Eq. (5.1) may be combined into the following single nonlinear integro-differential

equation

$$B w \frac{\mathrm{d}^2\theta}{\mathrm{d}s^2} + \hat{\mathbf{n}} \cdot \int_s^L (\boldsymbol{P} - \rho_s g h w \hat{\mathbf{e}}_y)\, \mathrm{d}s = 0, \tag{5.2}$$

where Eq. (5.1a) was integrated from s to L in order to satisfy the free end boundary condition $\boldsymbol{F}(L,t) = 0$ for all values of t. Eq. (5.2) can be solved once the external loading, $\boldsymbol{P}$, is known. The challenge is that, in general, $\boldsymbol{P}$ is not known *a priori*. Drawing upon the work in Ref. [110], we chose to investigate the horizontal geometry shown in Fig. 5-1(a)-(c) and Fig. 5-3, for which the following loading model has been introduced

$$\begin{aligned} \boldsymbol{P} &= \frac{Bw}{L^3}\left(\frac{1}{2}C_{\mathrm{d}}C_y \sin^2\theta - \frac{\pi}{4}\frac{w}{L}C_y \cos^2\theta \frac{\mathrm{d}\theta}{\mathrm{d}s}\right)\hat{\mathbf{n}} \\ &= (P_{\mathrm{d}} + P_l)\hat{\mathbf{n}}, \end{aligned} \tag{5.3}$$

where $C_y = \rho_a U^2 L^3/B$ is the Cauchy number (the dimensionless ratio between aerodynamic and bending forces) with ρ_a the air density. The first term, P_{d}, in Eq. (5.3) represents the local drag forces, arising from purely inertial effects, of a flow impinging perpendicular to the surface at each point $\boldsymbol{r}(s,t)$; *i.e.*, $P_{\mathrm{d}} \propto (U\hat{\mathbf{e}}_x \cdot \hat{\mathbf{n}})^2 = U^2 \sin^2\theta$. This term is characterized by a single fitting parameter, C_{d}, the local drag coefficient that is taken as a global constant. The local Lighthill forces due to momentum

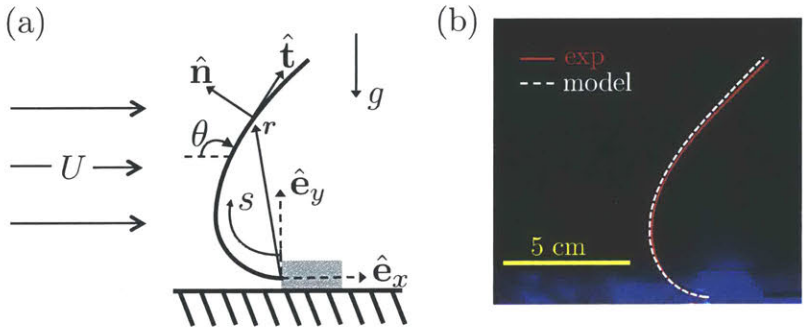


Figure 5-3: Setup of the horizontal configuration. (a) Diagram of the beam deformation. The local deflection angle, $\theta(s)$, behaves according to Eq. (5.2). (b) Numerical solution to forcing model Eq. (5.3) (dashed-white line) overlaid atop a typical experimental observation (solid-red line). The PETG strip shown has length L =15.24 mm, bending stiffness $B = 0.0125$ Nm and was exposed to a wind load of $U = 9.8$ m/s.

changes in the flow tangential to the beam arising from advection [113] are accounted for via the second term in Eq. (5.3) as

$$P_l = (U\hat{\mathbf{e}}_x \cdot \hat{\mathbf{t}}) \frac{\mathrm{d}}{\mathrm{d}s}\left(\rho_a \pi \left(\frac{w}{2}\right)^2 (U\hat{\mathbf{e}}_x \cdot \hat{\mathbf{n}})\right) = -\rho_a \pi \left(\frac{w}{2}\right)^2 U^2 \cos^2\theta \frac{\mathrm{d}\theta}{\mathrm{d}s}. \tag{5.4}$$

The system described by Eqs. (5.2)–(5.3) is solved by finite-difference method in which the local deflection in the forcing terms is initiated by a slight disturbance then updated over each iteration until convergence between steps. In particular, computations are initialized with $\theta_0(s) = s/L$, which fixes $\boldsymbol{P}_0$ and $\hat{\mathbf{n}}_0$ in Eq. (5.3) for the first iteration.

Returning to Eq. (5.2) with the derivative operator replaced by the centered finite-difference matrix of 250 nodes along s, $[D^2]$, and enforcing boundary conditions, an updated curvature angle $\theta(s)^{(\mathrm{new})}$ is obtained by matrix inversion,

$$\theta(s)^{(\mathrm{new})} = -\frac{1}{Bw}[D^2]^{-1}\left(\hat{\mathbf{n}}_0 \cdot \int_s^L (\boldsymbol{P}_0 - \rho_s g h w \hat{\mathbf{e}}_y)\, \mathrm{d}s\right). \tag{5.5}$$

The boundary condition at the end of the strip ($s = L$) is $\mathrm{d}\theta/\mathrm{d}s = 0$. The other boundary condition at the clamping location ($s = 0$) is set such that the initial angle in the numerical simulations is equal to that measured in the experiments $\theta_0 = \theta_{0,\mathrm{exp}}$, which is always less than 3°. Convergence is reached once repetitive application of the procedure above leads to less than 0.5% changes in $\theta(s)$. Finally, the arc profile of the beam is drawn by computing the local position through integration of the tangent vector,

$$\boldsymbol{r}(s) = \int_0^s \hat{\mathbf{t}}\, \mathrm{d}s, \tag{5.6}$$

as illustrated in Fig. 5-4 (red dashed line) for different values of the bending stiffness of the strip and loading velocities. Comparisons of the beam profile produced from the model and captured from experiments are discussed in the following section.

The vertically clamped configuration – shown in Figs. 5-1(d)-(f) and discussed in Section 5.7 – can be readily described through the vertical analog of Eq. (5.3), by modifying the trigonometric factors accordingly. Namely, the transformation $\theta(s) \rightarrow$

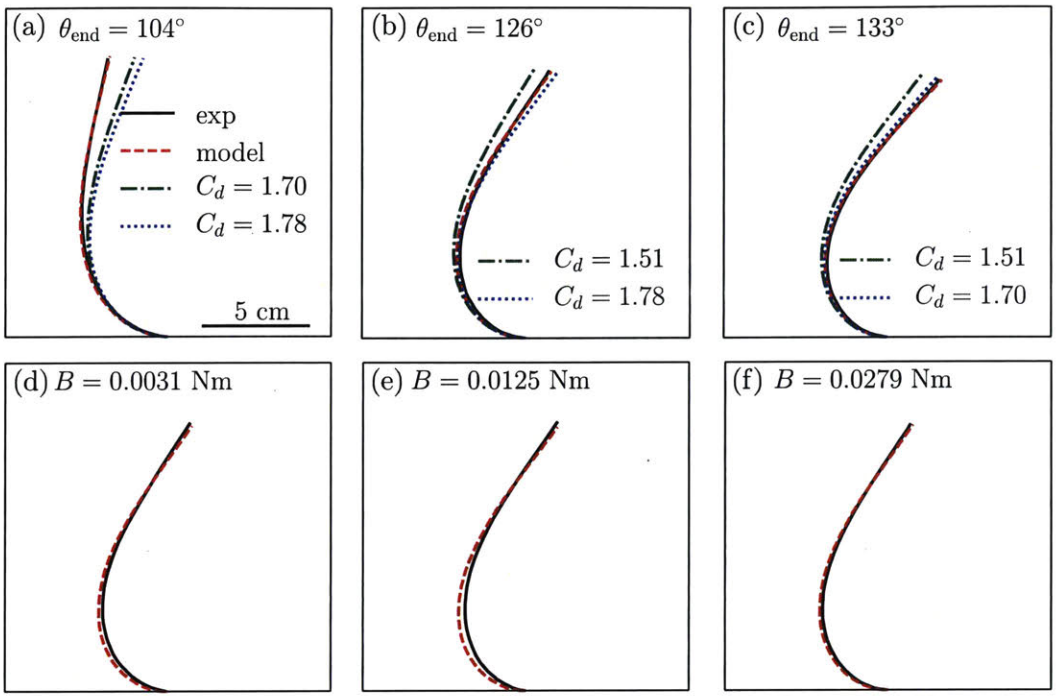


Figure 5-4: Examples of fitting drag coefficient, C_{d}, in the model to the experiments. (a)–(c) For the same strip of bending stiffness $B = 0.0279$ Nm, the wind tunnel is set to exhaust air at velocities $U = 10.3$, 12.7 and 14.0 m/s, respectively and fitted values for the drag coefficient are, respectively, $C_{\text{d}} = 1.51$, 1.70 and 1.78. The degree of deformation, given by the angle at the free end, is shown above each profile. For each tip deflection, profiles calculated with other values of C_{d} are also shown (dotted and dashed-dotted curves). (d)–(f) For similar end deflections, $\theta_{\text{end}} \approx 126°$, the bending stiffnesses are displayed for each material while exposed to wind velocities $U = 4.5$, 8.3 and 12.7 m/s respectively, and the corresponding fitted values of C_{d} =1.71, 1.84 and 1.70.

$-(\theta(s)+\pi/2)$ will be applied in the vertical configuration so that boundary conditions remain unchanged and positive angles θ represent deformation in the flow direction.

5.4 Validation of the numerical model against experiments

Different strip profiles can be obtained for different values of the flow velocity, U, by numerically solving Eqs. (5.2) and (5.3), with some initial guess for C_d. Towards validating our numerical simulations, these computed profiles can then be compared to those obtained from the experiments presented in Section 5.2, for samples with varying thicknesses tested at different values of U.

One way to compare the experimental and numerical profiles is to minimize the error per unit of arc-length, γ, between the two curves (experimental and numerical) for each strip at a given velocity; *i.e.*, the square root of the area between the two curves along the arc-length normalized by the length L of the strip, as shown in Fig. 5-5(a). To minimize this error, Powell's optimization scheme is invoked to best adjust C_d. The results are visually inspected to verify that the outputs are valid, as shown in Fig. 5-3. Alternatively, one could have considered the objective of minimizing the difference in $\theta(s)$ generated from the computational procedure with that obtained by processing experimental profiles. However, by minimizing a function related to the area between numerical and experimental profiles, the error in C_d may be interpreted more directly as it leads to different computed values of θ_end in comparison to observations. As such, we chose to focus on γ.

The precision of the fitting procedure may be quantitatively evaluated by considering the change in γ as a function of other parameters. Having obtained the optimal fit of C_d for each experiment by minimizing γ of a given strip at fixed U, we then consider how deviations from the optimal C_d change the objective function, γ, to quantify the sensitivity of the fit. The corresponding differences in the objective function, $\Delta\gamma$, are found by solving Eqs. (5.2)–(5.3) with a 10% increase and decrease in C_d. The

average $\Delta\gamma$ from these two modified drag coefficients are plotted in Fig. 5-5(b) for each experiment, from which it appears that changes in C_d lead to a smaller change in $\Delta\gamma$ as the beam deformation increases. A way to easily quantify this deformation is to measure the angle at the free end of the strip, θ_end. We can see in Fig. 5-5(b) that $\Delta\gamma$ decreases as θ_end increases. A physical interpretation can be drawn from the data shown in Fig. 5-5(c): changing C_d leads to a change in tip deflection angle, $\Delta\theta_\mathrm{end}$. By modifying C_d to be 5% and 10% above and below the optimal fit, and taking the average of the resulting difference in tip deflection from the two numerical solutions to Eqs. (5.2)–(5.3), we plot the predicted change $\Delta\theta_\mathrm{end}$ as a function of θ_end obtained from the optimal fit of C_d to experiments. Visually, Figs. 5-4(a–c) show this same effect. In the figure, the red dashed line corresponds to the profile calculated with the optimal C_d, whereas the blue dotted and green dashed-dotted lines represent the profiles calculated with sub-optimal C_d values (we used values corresponding the optimal C_d for the other two tip deflections shown in the figure). The profiles calculated by setting C_d slightly away from the optimal value, lead to more pronounced differences from the optimal profiles at smaller tip deflections than at larger tip deflections, which is in agreement with the results shown in Figs. 5-5(b) and (c).

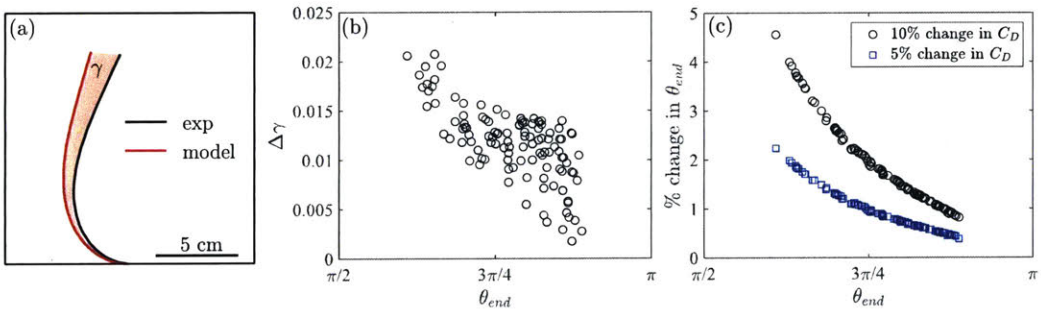


Figure 5-5: Difference between the experimental, and numerical results. (a) Experimental and numerical curves for $U = 12.7$ m/s and $B = 0.0279$ Nm with the area between the two curves shaded pink. The square root of the area between the two curves normalized by the beam length, γ, is minimized to find the best fit for C_d. (b) $\Delta\gamma$ as a function of the the tip angle with respect to the horizontal θ_end for different porosity ϕ when the optimal C_d is changed by 10%. (c) θ_end percentage change as a function of θ_end for 5% (□) and 10% (○) change in C_d.

Taking the results of Fig. 5-5(b) and (c) in aggregate, it then becomes apparent that a clear systematic bias exists in favor of fitting C_d at lower deflections, where the drag coefficient can be fitted more accurately. In other words, the computed profiles and the associated fitted values of C_d are less accurate for beams that are highly deformed. We speculate that this observation may be rationalized by considering the effects of aerodynamic shear drag on the elastic beam. Note that Eq. (5.3) accounts solely for drag normal to the surface of the beam and neglects the tangential components of drag. In the regime of strong aerodynamic loading, as the static beam profile approaches the horizontal, enhanced skin friction is expected to act, in addition to the normal component of drag (due to a a larger surface being aligned closer to the flow direction). Thus, the normal component of the drag may no longer be dominant and tangential stresses must also be taken into account. Since a modification of the aerodynamic loading model that accounts for shear is beyond the scope of our work, we restrict our analysis to bending profiles with a maximum tip deflection angle $\theta_\mathrm{end}^{(\mathrm{max})} = 135°$ (i.e. 45° from the vertical). We recognize that our specific choice for the value $\theta_\mathrm{end}^{(\mathrm{max})}$ is not based on a formal argument but, instead, on our expectation that, below that threshold, normal aerodynamic forcing dominates and Eq. (5.3) is appropriate. For situations beyond $\theta_\mathrm{end} > 135°$, when the strip is highly deformed, we found that Eq. (5.3) was not a satisfactory model to describe our experimental data.

Next, we illustrate our procedure of computing the shape of the aerodynamically loaded profiles and determining the associated C_d by fitting a series of experiments with various parameters. In Fig. 5-4(a–c), the experimental and computed profiles correspond to the same elastic strip (zero porosity) at increasing values of the flow velocity: $U = \{10.3,\ 12.7,\ 14.0\}$ m/s, respectively. The black lines show the profiles extracted from experiments, and the dotted red lines are results of the optimized numerical fit. The corresponding drag coefficients (computed through fitting), $C_\mathrm{d} = \{1.51,\ 1.70,\ 1.78\}$ appear to vary slightly with overall curvature, increasing with deformation. Along the bottom row in Fig. 5-4, continuous strips (no porosity) of three different bending stiffnesses are exposed to wind velocities

($U = \{4.5, 8.3, 12.7\}$ m/s, respectively) such that the end deflections is kept nearly constant at $\theta_{\text{end}} \sim 126°$, *i.e.* to target three similar final configurations. The corresponding values of drag coefficient for these nearly identical deformed configurations are, respectively, $C_{\text{d}} = \{1.71, 1.84, 1.70\}$, only showing relatively small variations. On the other hand, for fixed strip properties or fixed velocities, variations in C_{d} are dominated by variations in θ_{end}. This issue of relating the fitted drag coefficient, C_{d}, and deformation (in terms of the Cauchy number, C_y, the non-dimensional loading parameter) will be discussed further in Section 5.4.

Taking the mean and standard deviation of the fitted drag coefficient over a set of 9 experiments ranging in bending stiffness $B = \{0.0031, 0.0125, 0.0279\}$ Nm and velocities $3.9 < U[\text{m/s}] < 14.0$ m/s, we have found that our continuous strips (without any performations) have $C_{\text{d}} = 1.68 \pm 0.21$, in agreement with Ref. [110], who found a value of $C_{\text{d}} = 1.76$.

5.5 Design and characterization of the strips

The central emphasis of the current study is to quantify how the level of porosity of a slender flexible strip affects its aerodynamic loading and, consequently, its extent of deformation. The cross-section of the porous strips ($\phi > 0$) is naturally non-uniform due to the perforations. However, the choice of the array of the pores can affect this level of non-uniformity. To examine effect of the array on the non-uniformity we studied two different arrays: the hexagonal array used in the experiments and also a rectangular array, on which no experiments were performed. The unit cell of each array is shown in Figs. 5-6(a) and (b), respectively. Both the length of the unit cell and the number of holes is set to be identical for both cases. By varying the radius of the holes, the level of porosity can be controlled. To quantify the non-uniformity in the cross section, we calculated the normalized cross-sectional area, $\bar{A}$, along the unit cell. We define $\bar{A}$ as the ratio between the portion of solid material ligament (shown as the total length of the blue line in Figs. 5-6(a) and (b) at a given position in the unit cell) to the total width of the strip (shown as the combined length of the red and

blue lines at a given position in the unit cell). With this definition, a value of $\bar{A} = 1$ corresponds to a position in the unit cell where there are no holes across the width.

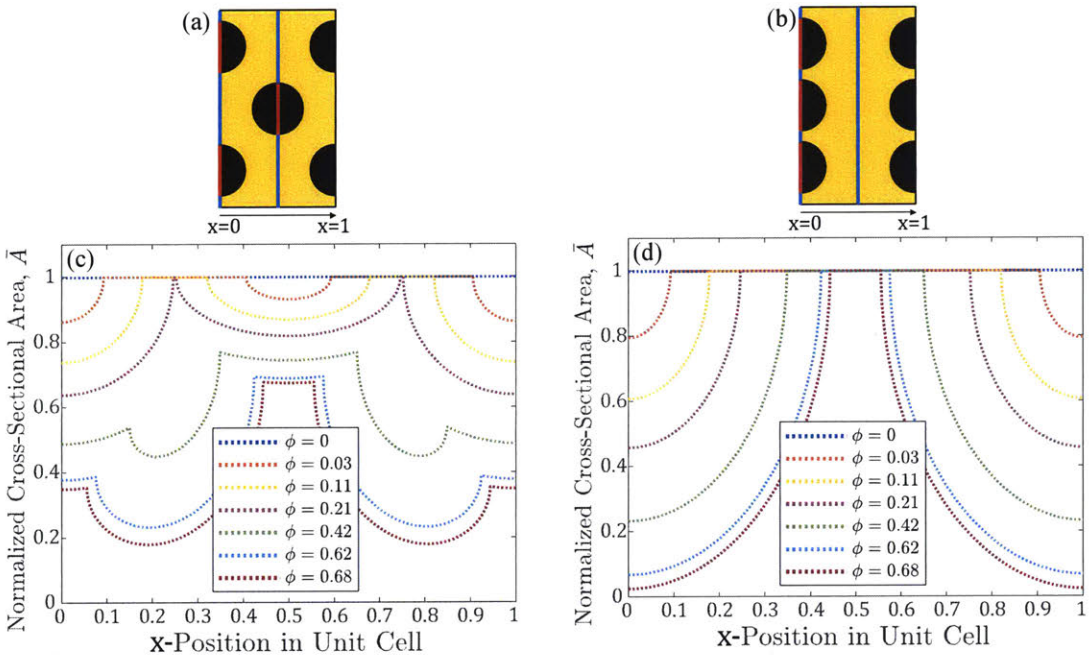


Figure 5-6: Variation in the cross-sectional area of two different arrays of perforations in the elastic strips. (a) Schematic of a unit cell in the hexagonal array used in the experiments (the black circles represent the void perforations). (b) Schematic of a rectangular array, with the same length unit cell and hole size as the hexagonal array. (c) and (d) Normalized cross-sectional area, $\bar{A}$, as a function of the position in the unit cell for the hexagonal and rectangular arrays respectively.

In Figs. 5-6(c) and (d), we present the variation of $\bar{A}$ along the unit cell, for both the hexagonal and rectangular arrays, respectively, with different levels of porosity. By definition, $\bar{A} = 1$ in solid strips with zero porosity. For perforated strips, $\bar{A}$ varies along the unit cell. In Fig. 5-7, we present the variation of $\bar{A}$ (defined as the standard deviation of $\bar{A}$ over the full unit cell) as a function of the level of porosity for each array. For all cases with $\phi > 0$, the variation of $\bar{A}$ is smaller for the hexagonal array than for the rectangular array. Therefore, the selection of a hexagonal array reduces the non-uniformity in the cross section when compared to a rectangular array.

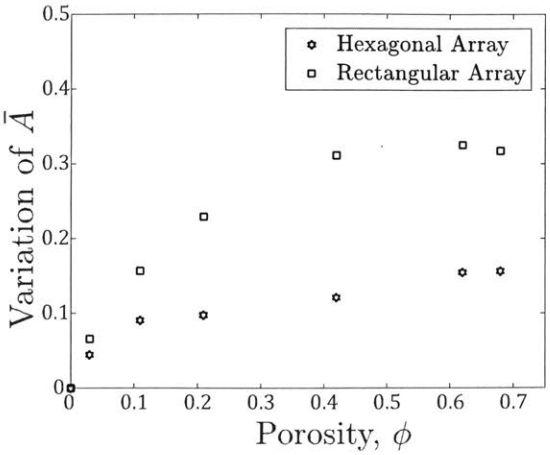


Figure 5-7: Comparison of the variation in $\bar{A}$ for the two arrays with various porosities.

To systematically study porosity as a parameter, we laser-cut the hexagonal array of circles of radius r on either solid PETG or acetate strips, as described in Section 5.2. Care was taken during the cutting procedure to avoid warping of the strip due to excessive heating, which may induce local volume changes near the edges of the cut thus changing the homogeneity of the thickness of the strip and modifying its flexural properties. The distance between the centers of the circles in the hexagonal lattice was 5.1 mm, which was fixed for all samples. A representative design of the laser-cut layout is shown in Fig. 5-8(a). This hexagonal arrangement of holes is identical to that of Ref. [121]. The porosity, ϕ, is defined as the ratio between the area of all the holes to the total bounding area of the strip. The explored levels of porosity were in the range $0 \leq \phi \leq 0.68$, and was changed by modifying r while keeping all other parameters of the layout constant. Examples of samples with different levels of ϕ are shown in Fig. 5-8(b).

5.5.1 Mechanical characterization of the strips: bending stiffness versus porosity

The bending stiffness for each strip (with different levels of porosity) was measured by horizontally clamping it as a cantilever beam, and quantifying the deformation that ensues due to self-weight, as shown in Fig. 5-9. Images of the deformed strips

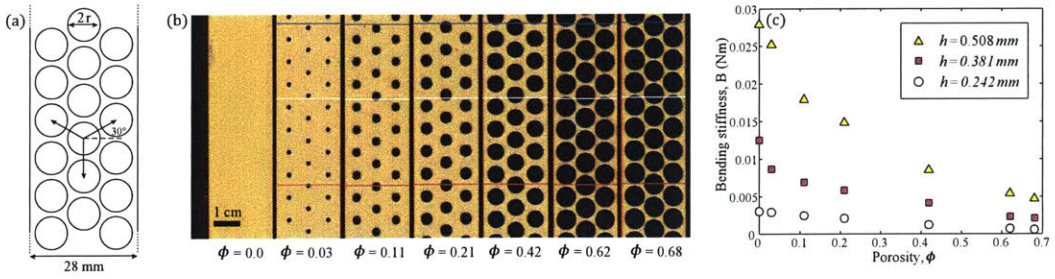


Figure 5-8: (a) Schematic of the strips containing an hexagonal arrangement of voids, with a level of porosity of $\phi = 0.62$. (b) Strips samples of PETG ($h = 0.508$ mm) for increasing porosity ϕ from 0 to 0.68. (c) Bending stiffness B as a function of ϕ for ($\circ$) $h = 0.242\,\text{mm}$, ($\square$) $0.381\,\text{mm}$, and ($\triangle$) $0.508\,\text{mm}$.

were acquired and processed using the same procedure described in Section 5.2. The cantilever ('hanging') length of the strip was set to $L = \{15.24,\ 20,\ 25\}\,\text{cm}$, shown in Figs. 5-9(a–c), respectively. For $L = 15.24\,\text{cm}$ the strip secured such that the clamp bisected a hole in the center column of the strips, as shown by the red line in Fig. 5-8(b). This is the same position where the strips were clamped in during the wind tunnel experiments. For $L = 20\,\text{cm}$ and $L = 25\,\text{cm}$, the strips were clamped through different regions of the unit cell, as indicated by the white and blue lines, respectively, in Fig. 5-8(b). For each value of L, a bending stiffness B was found following a procedure similar to the one used to compute C_d, above. With only gravity acting as an external force, Eq. (5.2) reduces to

$$B\frac{\text{d}^2\theta}{\text{d}s^2} - \rho_s g h(1-\phi)(L-s)\cos\theta = 0, \tag{5.7}$$

where the parameters ρ_s, h, L and ϕ are known *a priori*, and B is the only unknown. This classic model is well known to work for solid continuous beams ($\phi = 0$) and when the mass of the strip is evenly distributed as a uniform density, ρ_s.

To extend the above model to the perforated strips, the same assumption was made. However, since the mass of the strips is reduced due to the addition of the holes, an effective density with value of $\rho_s(1-\phi)$ was also assumed to be uniform throughout the strip. With this effective density, the strips are then treated as if they were otherwise continuous. Solving Eq. (5.7) for some initial guess of B, the resulting

deflection is first compared to experimental measurements. The area between the experimental and numerical curves is then minimized with respect to the bending stiffness, B.

In Fig. 5-8(c), we present results for the obtained values of B as a function of ϕ, for different thickness values ($h = \{0.242, 0.382, 0.508\}$ mm). For each strip, we found that the measurements of the resulting bending stiffness varied at most by 3.4%, regardless of the length and the specifics of the clamping position. As expected, the bending stiffness is larger for larger values of h, since $B \propto h^3$, and decreases with ϕ for every thickness h. Below, we shall use these above results as a look-up table when requiring knowledge on the relation of B as a function of ϕ.

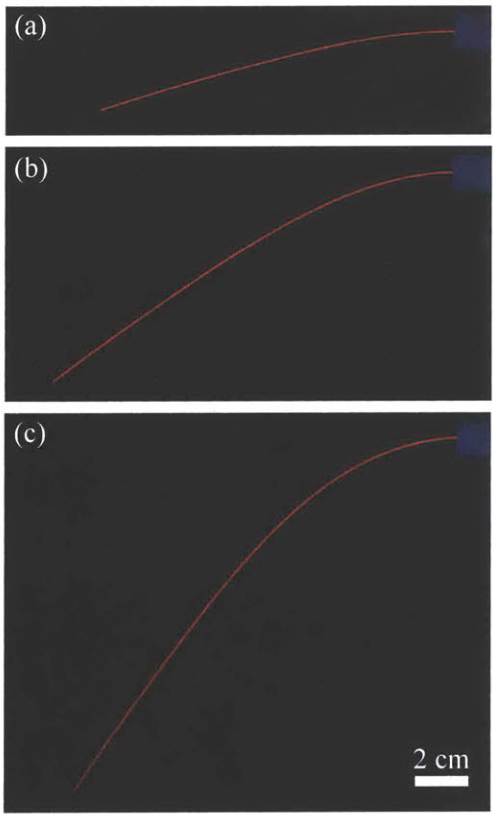


Figure 5-9: Photos of cantilever experiments on flexible strips to determine the bending stiffness. Strips were clamped with lengths of $L = \{15.24, 20, 25\}$ cm, shown in (a), (b), and (c), respectively.

5.6 Drag coefficient of the perforated elastic strips

Wind tunnel experiments were performed using the perforated strips described above (Section 5.5), following a protocol identical to that for continuous strips (Section 5.4), in both the horizontally and vertically clamped configurations. By fitting the experimental and the numerical profiles (Section 5.4), the drag coefficient, C_d, was then computed for different values of porosity ϕ, bending stiffness B, and flow speed U. An important point here is the assumption that the same treatment used for continuous strips can be applied to the loading of perforated strips, following Eq. (5.1). This means that the perforated strips are treated as if they are solid strips with an area equal to $L \times w$, and with a value for the bending stiffness, B, that was measured in Section 5.5.

For each specimen, experiments were run at several different values of the flow speed, U, and the experimental data were used to numerically compute the corresponding values of the drag coefficient, C_d. These individual C_d values calculated for each level of porosity were then averaged over the range of U, to yield a single C_d for each level of porosity, ϕ. In Fig. 5-10, we plot the averaged drag coefficient as a function of the porosity obtained from our experiments on flexible perforated strips in both configurations (horizontally and vertically clamped). Previous results from the literature for *rigid* perforated plates are also superposed on the plot [120, 121].

First, let us focus on the horizontally clamped configuration. We find that the average C_d decreases monotonically with increasing ϕ from $C_d = 1.68 \pm 0.21$ (the value found in Section 5.4 for continuous strips) down to $C_d = 0.71 \pm 0.10$ for $\phi = 0.68$. This trend is supported by the literature, specifically for rigid wire gauzes and screens [119, 124, 126]. In Fig. 5-10, the red squares are our experimental results of the horizontally clamped configuration, and the solid triangles are results using the vertically clamped configuration. Each point represents the average of 5 to 10 experiments. The error bars of both experimental data sets are the standard deviation of the averaging over velocity. The open circles are experimental measurements of C_d previously reported by Ref. [121] on wind tunnel experiments using the drag

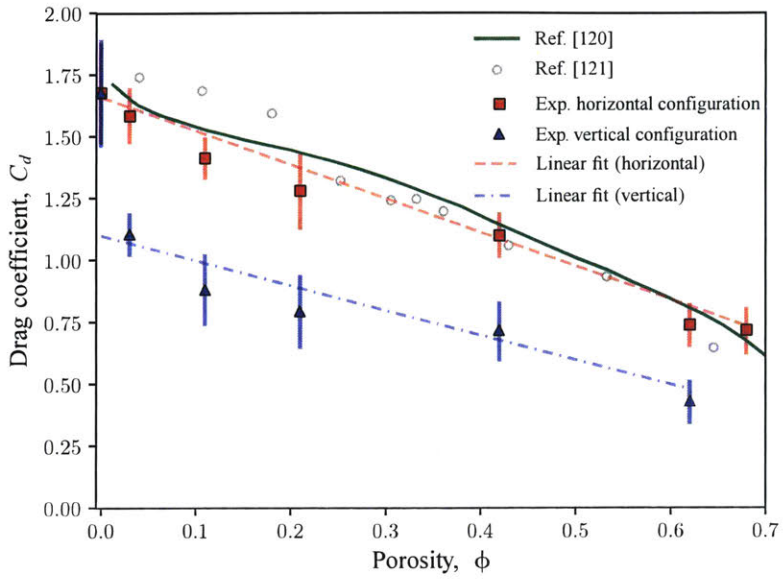


Figure 5-10: Drag coefficient C_d as a function of porosity ϕ. The solid line green line are experimental measurements extracted from Ref. [120] and open circles are experimental measurements extracted from Ref. [121], both for rigid perforated plates. Solid red squares (and solid blue triangles) are the fitted C_d in the horizontally (and vertically, respectively) clamped strip configurations obtained from our experimental data. The dashed red line is a linear fit to all of the experimental data in the horizontal configuration, and the dotted-dashed blue line is the linear fit for the experimental data in the vertical configuration, excluding the case of $\phi = 0$.

balance method for rigid perforated plates, with the same arrangement of holes as our samples. The green line is results from Ref. [120]. Interestingly, and surprisingly to us, there is good agreement between the results for rigid plates from the existing literature [119, 120, 121, 123, 126, 127] and our experimental data for flexible strips in the horizontal configuration, especially for large ϕ. There is some disagreement when $\phi < 20\%$: our experimental values of C_d are 12-15% lower than the data of Ref. [121] and 2-5% the prediction of Ref. [120] for rigid plates.

For the vertically clamped configuration, C_d also decreases with ϕ. However, we were surprised to find that, and have not yet been able to rationalize why, these results differ significantly from those for the horizontally clamped cased discussed above, as well as from the previous data for perforated *rigid* plates [121] and the associated

prediction [120]. We shall discuss the vertically clamped configuration in more detail below (Section 5.7).

In order to quantify the effect of the wind loading on the extent of deformation of the flexible perforated strips, we first study the dependence on the computed (fitted) C_{d} on the free-stream velocity in the horizontal configuration, for different values of ϕ, B and h, as shown in Fig. 5-11. Each symbol in the plot represents a different level of porosity (in the range $0 \leq \phi \leq 0.68$). As shown above, the average C_{d} decreases with the porosity. However, there is no trend of the drag coefficient with the velocity. Due to the highly deformable nature of these structures, the characteristic length that would generally be used to define a Reynolds number is not trivial to determine. Given that in the figure each curve is made up of experimental points with the same ϕ, but various B, a dimensionless quantity that normalizes the fluid loading by a quantity that relates to the bending is appropriate to examine. Therefore, we proceed by non-dimensionalizing the fluid loading by using the Cauchy number $C_y = \rho_a U^2 L^3 / B$.

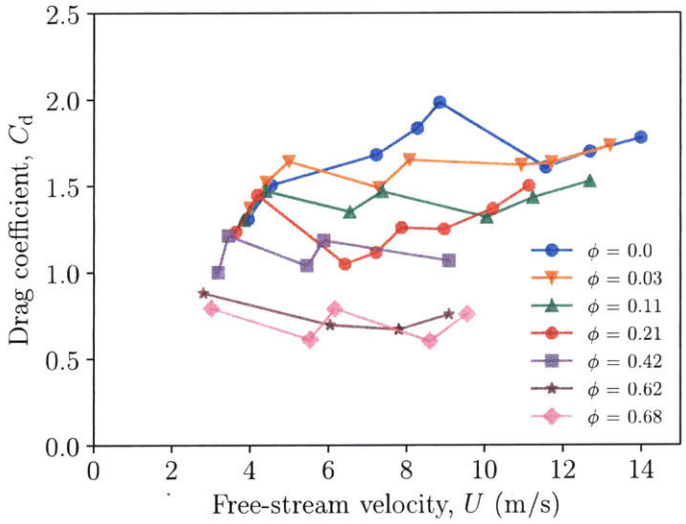


Figure 5-11: Drag coefficient, C_{d}, as a function of the free-stream velocity, U, for different different levels of porosity, $0 \leq \phi \leq 0.68$, in the horizontal configuration.

In Fig. 5-12a, we present a plot for C_{d} as a function of C_y, for different values of ϕ, B and h. The colors represent different wind velocities during the experiments. The

black line of open symbols represents the average value of C_d over different values of the flow speed and bending stiffnesses, for a given porosity ϕ. As shown in Fig. 5-10 and in Fig. 5-12(a), the velocity-averaged value of C_d decreases with porosity ϕ. Fluctuations from these average values are below 10% and decreasing for increasing porosity. Then, for a given value of ϕ, the drag coefficient does not change as the perforated strips deform due to wind loading.

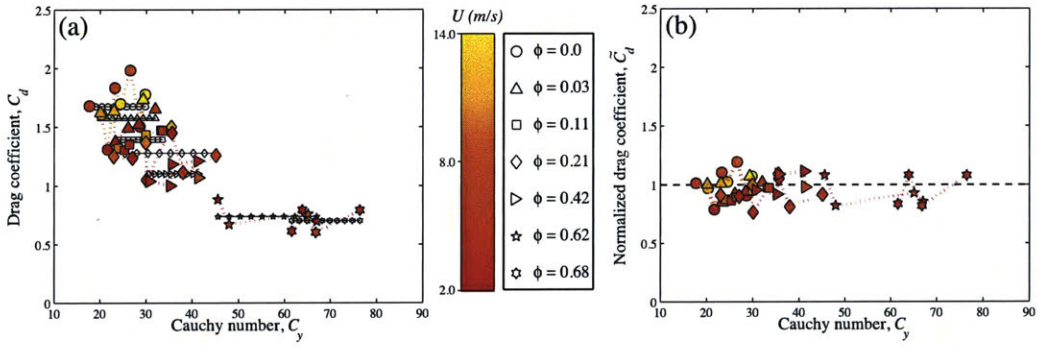


Figure 5-12: Dependence of the drag coefficient on the Cauchy number for the horizontal configuration. (a) Drag coefficient C_d as a function of the Cauchy number $C_y = \rho_a U^2 L^3/B$ for different porosity ϕ in the horizontal configuration. Horizontal symbols lines display average values of C_d for a given ϕ. (b) Normalized drag coefficient $\tilde{C}_\mathrm{d} = C_\mathrm{d}/C_\mathrm{o}(1-\alpha\phi)$ as a function of the Cauchy number $C_y = \rho_a U^2 L^3/B$ for the same values of porosity ϕ in the horizontal configuration. The fitted parameters are $C_\mathrm{o} = 1.68$ and $\alpha = 0.82$. The colorbar displays U in m/s.

Next, leveraging the monotonic decrease of C_d as a function of ϕ that we obtained in Fig. 5-10, we empiracally fit C_d to the linear function $C_\mathrm{d}^{fit} = C_\mathrm{o}(1-\alpha\phi)$, with $C_\mathrm{o} = 1.68 \pm 0.21$ (the value of C_d at $\phi = 0$) and $\alpha = 0.82 \pm 0.02$ where $C_\mathrm{o}\alpha$ is the slope of the linear fit. It should be noted that other dependences of C_d on ϕ have been formulated. For example, the theory for screens in Ref. [126] (which diverges at $\phi = 0$) or its refinement by Ref. [123] (which saturates at $\phi = 0$), both yield a nonlinear dependence of C_d on ϕ. Here, for simplicity, we have decided to use a simple linear fit, which we then use to plot, in Fig. 5-12(b), the normalized drag coefficient $\tilde{C}_\mathrm{d} = C_\mathrm{d}/C_\mathrm{d}^{fit}$ as a function of C_y for different values of porosity, ϕ. The dashed line corresponds to $C_\mathrm{d} \equiv C_\mathrm{d}^{fit}$. We find a very good collapse of our data around $\tilde{C}_\mathrm{d} = 1$

for all values of C_y. The variations of the data about $\tilde{C}_d = 1$ are below 10% for all perforated flexible strips and within 20% for the continuous strips.

Thus, in this configuration of horizontal clamping, the drag coefficient for flexible perforated strips decreases with porosity, in a very similar fashion as the one known and predicted for rigid plates by Refs. [120, 121]. Using this observation, the drag coefficient can be rescaled to show that when sorted by porosity, the drag coefficient is independent of the Cauchy number. Our empirical treatment of the data still leaves the fitted quantity α unexplained, but we hope that these results will instigate future theoretical work on this topic to help rationalize the physical nature of this prefactor.

5.7 Results of experiments in the vertical configuration

We now turn our attention to a more detailed discussion of the case where the elastic strip is clamped vertically, which was already introduced in Figs. 5-1(d–f). As described above, presuming the loading assumptions of Eq. (5.3), the modifications from the previous horizontal clamped cased to the current vertical case are purely trigonometric, $\theta(s) \to -[\theta(s) + \pi/2]$, such that the external aerodynamic loading can be written as

$$\boldsymbol{P} = \frac{Bw}{L^3}\left\{\frac{1}{2}C_{\mathrm{d}}C_y\cos^2\theta - \frac{\pi}{4}\frac{w}{L}C_y\sin^2\theta\frac{\mathrm{d}\theta}{\mathrm{d}s}\right\}\hat{\mathbf{n}}, \tag{5.8}$$

where θ now measures the beam angle from the vertical; see Fig. 5-13. Our imposed restriction at the free-end now reads $\theta_{\mathrm{end}} < 45°$ and it is enforced to avoid scenarios in which tangential forces become increasingly important, following the same arguments used in the horizontal configuration (see Section 5.4).

Repeating the experimental and numerical procedures outlined above, the effects of porosity for this vertically clamped configuration are summarized in Fig. 5-10. The measured drag coefficient in this configuration decreases with porosity, in a way that is *qualitatively* similar to the one measured in the horizontal configuration. The fluctuations (errorbars) around the mean values of C_{d} for every value of ϕ are of

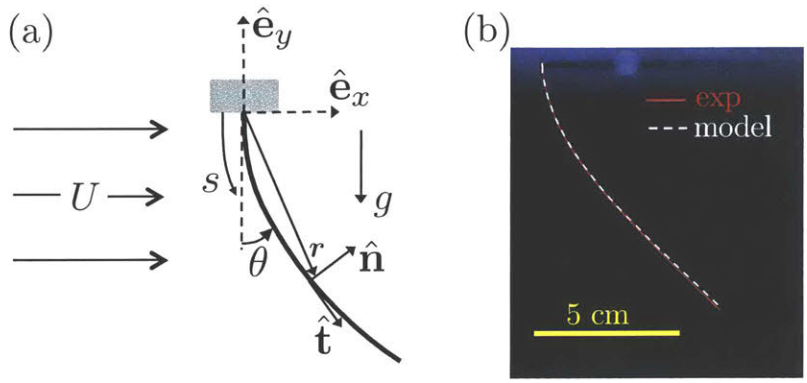


Figure 5-13: Setup of the vertical configuration. (a) Diagram of the beam deformation hanging vertically. The local deflection angle $\theta(s)$, now measured from the vertical, behaves according to Eq. (5.2). (b) Numerical solution to forcing model Eq. (5.8) (dashed-white line) overlaid atop a typical experimental observation (solid-red line).

the same order as those of the horizontal case. However, the measured values of the drag coefficient for strips with porosity are significantly lower (by 30-35%) than the horizontally clamped results. This is not the case for the continuous strips, where they do arrive at the same value C_o of the horizontally clamped case.

The fact that there is a *quantitative* difference between the values of C_d as a function of ϕ for both configurations is striking and unexpected. These simple experimental configurations rely on the same type of loading, material/geometric properties for the strips and levels of porosity; the only difference is in the way that they are clamped. Therefore, there is strong dependence on boundary conditions for drag (and therefore on reconfiguration) when applied to flexible porous bodies. The effects of clamping configuration, appear to have been overlooked in the past, and should be regarded in more detail in the future.

When C_d is computed as a function of C_y, shown in Fig. 5-14(a), the data for the vertically clamped case follows a trend similar to the horiziontal case presented above. This means that C_d remains constant for different values of C_y when sorted by porosity. Following the same procedure as in Section 5.6, we linearly fit C_d as a function of ϕ (excluding the case of $\phi = 0$): $C_d^{fit} = C_o(1 - \alpha\phi)$. The fitted parameters are $C_o = 1.10 \pm 0.1$ and $\alpha = 0.93 \pm 0.03$ where $C_o\alpha$ is the slope of the linear fit. Using

this fit, we plot in Fig. 5-14(b) the normalized drag coefficient $\tilde{C}_\mathrm{d} = C_\mathrm{d}/C_\mathrm{d}^{fit}$ as a function of C_y for $\phi > 0$. The dashed line corresponds to $C_\mathrm{d} \equiv C_\mathrm{d}^{fit}$. As in the case of the horizontally clamped perforated strips, we find a good collapse of all our data around $\tilde{C}_\mathrm{d} = 1$, for all values of C_y, with variations below 15% for all values of $\phi > 0$.

There is a significant difference in the value of C_d between the case of continuous strips ($\phi = 0$) and the porous strips ($\phi > 0$) in this vertically clamped configuration. At $\phi = 0$, the mean value of the experimental data agrees well with the horizontally clamped configuration (within error bars) but it is 50% larger than the C_o obtained from the linear fit for the vertical configuration, *i.e.* there is a sharp change as soon as some perforation is included ($\phi = 0.03$). Such a steep drop in the value C_d as a function of ϕ in the limit of small porosity is surprising and deserves further attention in future studies.

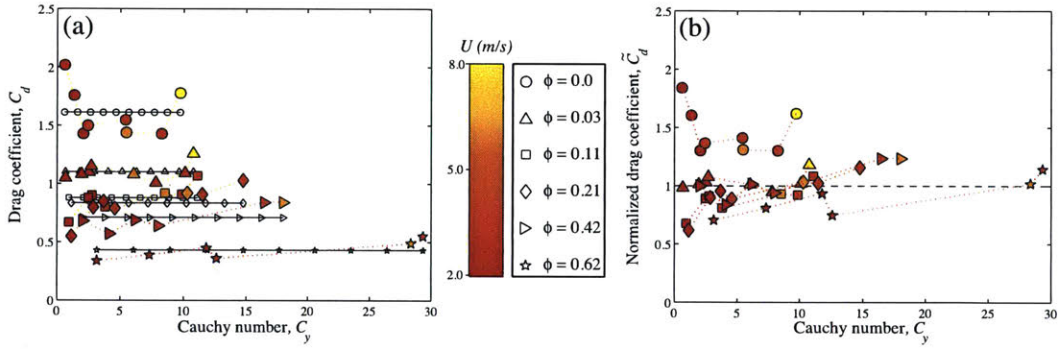


Figure 5-14: Dependence of the drag coefficient on the Cauchy number for the vertical configuration. (a) Drag coefficient C_d as a function of the Cauchy number $C_y = \rho_a U^2 L^3/B$ for different porosity ϕ in the vertical configuration. Horizontal symbols lines display average values of C_d for a given ϕ. (b) Normalized drag coefficient $\tilde{C}_\mathrm{d} = C_\mathrm{d}/C_\mathrm{o}(1 - \alpha\phi)$ as a function of the Cauchy number $C_y = \rho_a U^2 L^3/B$ for the same values of porosity ϕ in the vertical configuration. Here $C_\mathrm{o} = 1.10$ and $\alpha = 0.93$. The adjacent colorbar displays U in m/s.

5.8 Discussion of results

To the best of our knowledge, no previous study had investigated the effect of flexibility on the drag force acting on perforated structures. It is widely known that an aeroelastic coupling between flow and structure leads to reconfiguration [13, 107, 108, 110], which on its own presents challenges in their understanding. One of these challenges is to describe the degree of deformation of elastic structures using reduced models which account for the complex fluid-structure interactions in different configurations.

In our current study we acquired and analyzed experimental data for the deformed shapes of porous elastic strips, for different values of U, ϕ and B using the reduced model presented in Ref. [110] where C_{d} is the only global fitting parameter. We have found that C_{d} monotonically decreases with ϕ in both configurations. This tendency can be fitted accurately by a linear function on both the horizontal and vertical configurations for $\phi > 0$, as shown in Fig. 5-10, with different slopes and values at $\phi = 0$.

The observed decreasing trend of C_{d} as a function of ϕ for flexible perforated strips on both configurations resembles *qualitatively* what has been found for rigid perforated plates or screens for both clamping configurations. In these rigid counterparts, the dependence of C_{d} on ϕ has been an extensive subject of study in the literature via the pressure drop coefficient K. Since Refs. [126, 127], several functional forms for K (and thus C_{d}) as a function of ϕ have been proposed and experimentally tested on rigid perforated screens and plates for large values of Re [121, 124]. The main commonality across all these various studies is that the aerodynamic loading on these rigid structures can be tailored by increasing their porosity. This is also the case for our experimental study of perforated flexible structures in both configurations. In the case of the horizontal configuration, the drag coefficient for flexible perforated structures follows *quantitavely* the theoretical prediction for rigid plates (within error bars) [121]. We have also found that C_{d} is constant as a function of the Cauchy number C_y, which is the ratio between the force due to fluid loading on the elastic strip to its bending rigidity, for a given value of ϕ as displayed in Fig. 5-12(a) and

Fig. 5-14(a). This relation is found for all our experimental values of flow speeds, material properties and levels of porosity. Thus, we can argue that drag forces, when rescaled by porosity, are independent of the degree of reconfiguration of the flexible perforated strips, which we believe is an important finding from our work. As such, we have quantified the effect of porosity on the drag force on flexible structures upon wind-loading.

It is important to highlight the fact that we have made use of a particular reduced model to describe our experimental data (and to compute C_{d} as a function of ϕ). While using our chosen model, we determined a value of C_{d}, which was defined as the local drag coefficient of an infinitesimal element of the strip. In doing so, it was implicitly assumed that this C_{d} is constant over the extent of the strip. This local drag coefficient is different from that of other reduced models, which often employ a more global definition of C_{d}, thereby allowing for claims about the Vogel exponent. In our work, we cannot comment on the appropriate Vogel exponent, because we do not measure nor do we calculate the x-component of the drag forces that would be required to determine the classical drag coefficient defined as $C_{\mathrm{d}} = 2F/(\rho U^2 A)$. Reduced models such as the ones presented in Refs. [109,109,110,114,114,115,144,145] are used to describe the aeroelastically induced reconfiguration of elastic materials. The choice of each of these particular models depends strongly on the loading configuration of the system under study, and that affects the way some of its properties are computed or measured. This poses a great challenge on the prediction and control of the shape of these flexible structures as they reconfigure when aerodynamically loaded. A more thorough study on the way reduced models are used on different configurations is needed. For instance, a first step could be the usage of different models on the same configuration, where a comparison on their predictive capabilities and differences can be made.

5.9 Conclusion

In this Chapter, we have presented results of an experimental and numerical study on the dependence of the drag coefficient, C_{d}, on porosity, ϕ, of flexible reconfigurable structures subjected to an aerodynamic loading. We performed wind tunnel experiments in two different configurations (termed horizontal and vertical), in which we measured the deformed profile of the strips at various wind speeds (Section 5.2). Using the reduced loading model presented in Section 5.3, we were able to numerically predict the deformation of aerodynamically loaded strips with given bending and mass properties (calculated in Section 5.5). We compared experimental and numerical results to determine the drag coefficient of strips with various porosities.

We found that, in both the horizontal and vertical configurations, C_{d} was independent of the Cauchy number, and only a function of the porosity. Additionally, both configurations exhibited a monotonic decrease in the drag coefficient with increasing porosity. The drag coefficient determined in the horizontal configuration, showed excellent quantitative agreement with drag coefficient of previous results for rigid perforated plates [120, 121]. However, the perforated strips in the vertical configuration demonstrated a consistently lower C_{d} than our results in the horizontal configuration. This was a surprising result that we hope inspires further investigation.

THIS PAGE INTENTIONALLY LEFT BLANK

Chapter 6

Conclusion

In this chapter, we summarize our work, discuss some limitations, and suggest future research directions.

6.1 Summary of Findings

This thesis examined the aerodynamic performance of deformable structures exposed to a high Reynolds number air flow. We harnessed the flexible nature of membranes to create a system that allowed us, through pneumatic actuation, to modify the surface topography of cylindrical bodies to control the aerodynamic drag when exposed to changing flow conditions. In one part of our study, the fluid forces had a small effect on the deformation of the bodies. In another part, we studied a situation in which the fluid flow provided the primary load controlling the shape of a flexible structure. To properly understand these systems, we used experiments and simulations to conduct a thorough exploration of both their mechanics of deformation and their aerodynamic performance.

In Chapter 1, we presented a literature review and introduced a number of concepts relevant to the rest of this thesis, including the drag coefficient, C_{d}, the Reynolds number, Re, and the rapid change in drag known as the drag crisis. We discussed the flow mechanisms that cause the drag crisis to occur for bluff bodies. We also presented the current state of the art on the effect of the surface topography of bluff

bodies on drag at high Reynolds numbers. Additionally, we discussed related work on reconfiguration in flexible structures exposed to flow, and the effect of porosity on the drag of rigid bodies.

In Chapter 2, we studied axially grooved cylinders. We first presented a novel system, in which the depth of grooves on cylindrical specimens could be tuned with pneumatic actuation. The specimens comprised a flexible latex membrane stretched over a rigid acrylic skeleton with radial spokes. We used both mechanical experiments and FEM simulations to determine the dependence of the groove depth, d, on the applied pressure, Δp. For our specimens, we found a linear relationship between the two. Additionally, we found that when we normalized the depth ($\bar{d}$) and pressure ($\Delta\bar{p}$), the data collapsed onto a single linear curve. Having characterized the deformation of the specimens, we proceeded to perform wind tunnel experiments. The experiments were executed with a custom built apparatus that could control Δp, and simultaneously measure the wind speed and drag force on the specimens. With this setup, we performed both fixed and active wind tunnel experiments. In the fixed tests, we maintained a constant groove depth as the wind speed was increased, and measured the drag force. As we made the grooves deeper, the drag crisis occurred at lower Reynolds numbers, and the minimum drag coefficient increased. We then used the results of the fixed groove experiments to develop an active control loop system, in which the groove depth was automatically adjusted based on the wind speed. We demonstrated that, with a single actively morphable specimen, we could achieve a drag coefficient that was consistently and significantly lower than that of the fixed specimen counterparts.

In Chapter 3, we presented the results of work inspired by the dimples on golf balls. We used cylindrical specimens, that were constructed using the same technique used to construct the grooved cylinders in Chapter. 2. The skeleton of the dimpled specimens, were made of an acrylic tube with an array of circular holes in the surface. We performed mechanical experiments on specimens with different dimple diameters, and found that the dimple depth increased nearly linearly with the applied pressure. Based on an analytical solution from Cao *et al.* [143], we also found a scaling rela-

tion that enabled us to non-dimensionalize and collapse the data for specimens with different dimple diameters. Having determined the relationship between the applied pressure and the deformation of the dimples, we proceeded to perform wind tunnel experiments on specimens with various uniform distributions of dimples. We found that for a given layout of the dimples, the dependence of the drag coefficient on the Reynolds number, $C_{\mathrm{d}}(Re)$, was independent of the dimple diameter but varied with the dimple depth. We also studied various non-uniform distributions, by systematically removing rows of dimples from the uniform array. We found that when we removed the row of dimples near the stagnation point, at $\theta = 0°$ and $\pm 30°$, the aerodynamic performance was similar to that of a uniform array. However, removing the rows of dimples at $\theta = \pm 60°$, caused a significant change in $C_{\mathrm{d}}(Re)$.

In Chapter 4, we presented the results of active dimple experiments, in which the dimple depth was tuned as the wind speed changed. We first set out to minimize the drag on a specimen as the Reynolds number increased. The results of the fixed dimple experiments were used to determine, for each Re, which dimple depth produced the lowest C_{d}. We fitted a continuous function (an exponential) to this optimal dimple depth versus Reynolds number data. This empirical description of the data was used in a control loop that automatically changed the dimple depth based on the wind speed. With this control system, we were able to produce a $C_{\mathrm{d}}(Re)$ behavior that was consistently below that of any individual fixed specimen. We also demonstrated that a similar strategy could be employed to alter the drag coefficient to have other functional dependences on the Reynolds number; specifically constant, rapidly decreasing, and rapidly increasing. We were only able to achieve these particular forms of $C_{\mathrm{d}}(Re)$ for specimens with relatively small dimple diameters. This difficulty was caused by the sensitivity of dimple depth (and therefore C_{d}) to small variations in the pressure applied to specimens with larger dimple diameters.

In Chapter 5, we explored the effect of porosity on the deformation of flexible perforated strips. We manufactured flexible strips with various levels of porosity, which we achieved with a hexagonal array of holes. The bending stiffness was determined based on static cantilever tests, in which the shape of the hanging strip was mea-

sured. We performed wind tunnel experiments on the strips in two configurations, vertical and horizontal, at various wind speeds. The deformed shape of the strip was determined, and using a reduced loading model, we determined the drag coefficient of the strips. We found that the drag coefficient was independent of the Cauchy number, and was a decreasing function of the porosity. Additionally, we found that the dependence of the drag coefficient on the porosity in the horizontal configuration was nearly identical to that of a rigid porous plate. In the vertical configuration, however, the porous strips had a consistently lower C_{d} than in the horizontal configuration and the rigid porous plates.

6.2 Limitations and Future Work

The work presented here has a number of limitations, and raises some exciting new questions that deserve further attention. Here, we suggest future work that would build on the results already presented.

6.2.1 Aerodynamic drag on deformable structures

In Chapters 2 – 4, we studied the effect of a small subset of the infinite number of possible surface topographies. When studying the non-uniform arrays, we found that removing the rows of dimples near the natural separation point, led to a significant change in the aerodynamic drag performance compared to the uniform arrays. We did not, however, explore the impact of localized tunable surfaces. We suggest that further experiments should be performed on specimens with a focus on *localized*, tunable surface topography, particularly near the separation point. We propose that perhaps the whole body may not need to have a patterned surface; patterning only a small region might be sufficient to significantly effect the drag.

Additionally, these studies were limited in scope to cylindrical specimens. Programming the drag with tunable surface topography could be applied to other systems. However, the dependence of the drag profile on the magnitude of the surface modifications (*i.e.*, groove or dimple depth), will likely be different for other

geometries. We propose experiments on other bluff bodies, with tunable surface topographies near the separation point. In particular, thinking about applying the ideas of this work to automobiles, we suggest these experiments be performed on non-symmetric bodies, so the effect of lift can also be investigated.

While our system for tuning the surface topography has proven to successfully control the drag, it is not be practical in many applications. Pneumatically actuating a flexible membrane on a rigid skeleton to modify the surface topography works well in the laboratory setting. However, it is cumbersome and, once punctured, the specimens can no longer be controlled. We propose that other, more robust, methods of actuating surfaces be explored. Possibilities include particle-enhanced soft composites [136], shape memory polymers [137], and electroactive materials [138].

6.2.2 Flexible perforated strips

As discussed in Chapter 5, we found a significant difference between the drag coefficient calculated in the vertical and horizontal configuration. The clamping near the wall could affect the results, since the wall prevents the flow from traveling around the clamped end. We hope that our results will motivate future experiments, in both the horizontal and vertical configurations, where the strips are clamped across the center of the wind tunnel, away from the walls, similar to those experiments performed by Kim *et al.*. [148]. These results could illuminate the reasons for the different results in our vertical and horizontal configurations, which we find intriguing, puzzling, and certainly worthy of further investigation. Additionally, in this work, we used only one reduced loading model, and we suggest implementing other loading models to further investigate the difference between the two configurations.

Finally, we focused our study on flexible perforated strips that were quasi-statically deformed. However, when the wind speed is sufficiently high, the strips can begin to flutter. While fluttering of solid sheets has been extensively studied [91, 101, 102, 103, 111, 112, 116, 117], very little work has been done to investigate the effect of porosity on the fluttering dynamics. We propose that studies similar to those done with solid sheets, be performed on perforated strips to further the understanding of

the combined effects of flexibility and porosity in structures.

6.3 Final Remarks

In closing, the work performed throughout this thesis, demonstrates the potential utility of actively controlling surface topography to reduce aerodynamic drag under varying conditions. Drag reducing surfaces, could be incorporated into systems that are used to address many modern day problems. For example, actively reducing the drag on automobiles as the speed changes, could improve fuel efficiency, and thus reduce carbon emissions. Additionally, a reduction in drag forces could increase mechanical robustness of structures, by leading to lighter weight systems that can withstand the same loading conditions. While our mechanism used to control surface topography is not yet suitable outside of the laboratory, many of our findings (*e.g.*, that dimple size is not important but dimple depth is) should be widely applicable. There is still lots of work to be done, but we believe that the results of this thesis represent an important first step down an exciting path of aerodynamic exploration.

Bibliography

[1] R Nathan, GG G Katul, HS S Horn, SM M Thomas, R Oren, R Avissar, S W Pacala, and S A Levin. Mechanisms of long-distance dispersal of seeds by wind. *Nature*, 418(July):409–413, 2002.

[2] Michael L. Cain, Brook G. Milligan, and Allan E. Strand. Long-Distance Seed Dispersal in Plant Populations. *Am. J. Bot.*, 87(9):1217, sep 2000.

[3] Henry Nicholas Ridley. *The dispersal of plants throughout the world, by Henry N. Ridley.* L. Reeve & Co., Ltd Ashford, Kent, 1930.

[4] A.K. Shukla, M.R. Vijayaraghavan, and B. Chaudhry. *Bioilogy of Pollen.* APH Publishing, 1998.

[5] Juan José Robledo-Arnuncio. Wind pollination over mesoscale distances: an investigation with Scots pine. *New Phytol.*, 190(1):222–233, apr 2011.

[6] James B. Harrington and Kurt Metzger. Ragweed pollen density. *Am. J. Bot.*, 50(6):532–539, 1963.

[7] J Grace. The turbulent boundary layer over a flapping Populus leaf. *Plant Cell Environ.*, 1(1):35–38, 1978.

[8] Emmanuel de Langre. Effects of Wind on Plants. *Annu. Rev. Fluid Mech.*, 40(1):141–168, 2008.

[9] John S Roden. Modeling the light interception and carbon gain of individual fluttering aspen (Populus tremuloides Michx) leaves. *Trees-Struct. and Funct.*, 17(2):117–126, 2003.

[10] Hongliang Tong and Lawrence E Hipps. The effect of turbulence on the light environment of alfalfa. *Agric. For. Meteorol.*, 80(2-4):249–261, 1996.

[11] The influence of gravity and wind on land plant evolution. *Rev. Palaeobot. Palynol*, 102(1):1 – 14, 1998.

[12] S. Talley and G. Mungal. Flow around cactus-shaped cylinders. *Center for Turbulence Research Annual Research Briefs*, pages 363 – 376, 2002.

[13] S Vogel. Drag and flexiility in sessile organisms. *Am. Zool.*, 24(December 1982):37–44, 1984.

[14] Mordecai J Jaffe. Thigmomorphogenesis: the response of plant growth and development to mechanical stimulation. *Planta*, 114(2):143–157, 1973.

[15] C. Coutand and B. Moulia. Biomechanical study of the effect of a controlled bending on tomato stem elongation: local strain sensing and spatial integration of the signal. *J. Exp. Bot.*, 51(352):1825–1842, 2000.

[16] M S Watt, J R Moore, and B McKinlay. The influence of wind on branch characteristics of Pinus radiata. *Trees*, 19(1):58–65, 2005.

[17] Michael H Dickinson, Fritz-Olaf Lehmann, and Sanjay P Sane. Wing rotation and the aerodynamic basis of insect flight. *Science*, 284(5422):1954–1960, 1999.

[18] Sanjay P Sane. The aerodynamics of insect flight. *J. Exp. Biol.*, 206(23):4191–4208, 2003.

[19] Crawford H Greenewalt. The flight of birds: the significant dimensions, their departure from the requirements for dimensional similarity, and the effect on flight aerodynamics of that departure. *Trans. Am. Phil.*, 65(4):1–67, 1975.

[20] C.P. Ellington. Limitations on animal flight performance. *J. Exp. Biol.*, 160(1):71–91, 1991.

[21] C. Peterson. The Fluid Dynamics of Parachute Inflation. *Annu. Rev. Fluid Mech.*, 28(1):361–387, 1996.

[22] W-H Hucho. The Aerodynamic Drag of Cars Current Understanding, Unresolved Problems, and Future Prospects. In *Aerodynamic drag mechanisms of bluff bodies and road vehicles*, pages 7–44. Springer, 1978.

[23] Jeff Howell and Geoff Le Good. The influence of aerodynamic lift on high speed stability. Technical report, 1999.

[24] Joseph Katz. Aerodynamics of Race Cars. *Annu. Rev. Fluid Mech.*, 38(1):27–63, 2006.

[25] K. Yusuf Billah and Robert H. Scanlan. Resonance, Tacoma Narrows bridge failure, and undergraduate physics textbooks. *Am. J. Phys.*, 59(2):118–124, 1991.

[26] Peter A. Irwin. Wind engineering challenges of the new generation of super-tall buildings. *J. Wind Eng. Ind. Aerodyn.*, 97(7-8):328–334, 2009.

[27] William F. Baker, D. Stanton Korista, and Lawrence C. Novak. Burj Dubai: Engineering the world's tallest building. *Struct. Des. Tall Spec. Build.*, 16(4):361–375, 2007.

[28] Jesus Diaz. The tallest apartment building in America sways 4 to 5 feet, 2014.

[29] Ronald L. Panton. *Incompressible Flow.* John Wiley & Sons, Hoboken, New Jersey, 4 edition, 2013.

[30] P. Bearman. *Bluff Body Hydrodynamics.* The National Academies Press, Washington, DC, 1997.

[31] Frank M. White. *Fluid Mechanics.* McGraw-Hill, New York, NY, sixth edition, 2008.

[32] Haecheon Choi, Woo-Pyung Jeon, and Jinsung Kim. Control of Flow Over a Bluff Body. *Annu. Rev. Fluid Mech.*, 40:113–139, 2008.

[33] Timothy N. Crouch, David Burton, Zach A. LaBry, and Kim B. Blair. Riding against the wind: a review of competition cycling aerodynamics. *Sports Eng.*, 20(2):81–110, 2017.

[34] C. Wieselsberger. Neuere Feststellungen uber die Gesetze des Flussigkeitsund Luftwiderstandes. *Physikalische Zeitschrift*, 22:321–328, 1921.

[35] Noel K Delany and Norman E Sorensen. Low-speed drag of cylinders of various shapes. 1953.

[36] RK Finn. Determination of the drag on a cylinder at low reynolds numbers. *Journal of Applied Physics*, 24(6):771–773, 1953.

[37] D_J Tritton. Experiments on the flow past a circular cylinder at low reynolds numbers. *Journal of Fluid Mechanics*, 6(4):547–567, 1959.

[38] A. Roshko. Experiments on the flow past a circular cylinder at very high Reynolds number. *J. Fluid Mech.*, 10(3):345–356, 1961.

[39] C H K Williamson. Vortex Dynamics in the Cylinder Wake. *Annu.l Rev. Fluid Mech.*, 28(1):477–539, 1996.

[40] S.P. Singh and S. Mittal. Flow past a cylinder: Shear layer stability and drag crisis. *Int. J. Numer. Methods Fluids*, 47:75–98, 2005.

[41] E. Achenbach. Influence of surface roughness on the cross-flow around a circular cylinder. *J. Fluid Mech.*, 46(Part 2):321–335, 1971.

[42] G K Suryanarayana and A Prabhu. Effect of natural ventilation on the boundary layer separation and near-wake vortex shedding characteristics of a sphere. *Exp. Fluids*, 29(6):582–591, 2000.

[43] P T Tokumaru and P E Dimotakis. Rotary oscillation control of a cylinder wake. *J. Fluid Mech.*, 224:77–90, 1991.

[44] D. Shiels and a. Leonard. Investigation of a drag reduction on a circular cylinder in rotary oscillation. *J. Fluid Mech.*, 431:297–322, 2001.

[45] Sejeong Jeon, Jin Choi, Woo-Pyung Jeon, Haecheon Choi, and Jinil Park. Active control of flow over a sphere for drag reduction at a subcritical Reynolds number. *J. Fluid Mech.*, 517:113–129, 2004.

[46] Jinsung Kim and Haecheon Choi. Distributed forcing of flow over a circular cylinder. *Phys. Fluids*, 17(3), 2005.

[47] P W Bearman. The effect of base bleed on the flow behind a two-dimensional model with a blunt trailing edge. *Aeronaut. Quart.*, 18(03):207–224, 1967.

[48] P.W. Bearman and J.K. Harvey. Golf Ball Aerodynamics. *Aeronaut. Quart.*, 27(2):112–122, 1976.

[49] J-W He, R Glowinski, R Metcalfe, A Nordlander, and J Periaux. Active control and drag optimization for flow past a circular cylinder: I. Oscillatory cylinder rotation. *J. Comput. Phys.*, 163(1):83–117, 2000.

[50] Robert D Blevins. *Flow-induced vibration.* Van Nostrand Reinhold Co., Inc., New York, NY, 2nd edition, 1990.

[51] R. E. D. Bishop and A. Y. Hassan. The Lift and Drag Forces on a Circular Cylinder in a Flowing Fluid. *Proc. Royal Soc. A*, 277(1368):51–75, 1964.

[52] Jeonglae Kim, Seonghyeon Hahn, Jinsung Kim, Dong-kon Lee, Jin Choi, Woo-Pyung Jeon, and Haecheon Choi. Active control of turbulent flow over a model vehicle for drag reduction. *J. Turbul.*, 5(October), 2004.

[53] C.J. Wood. The effect of base bleed on a periodic wake. *J. Royal Aero. Soc.*, 68(643):477–482, 1964.

[54] D R Arcas and L G Redekopp. Aspects of wake vortex control through base blowing/suction. *Phys. Fluids*, 16(2):452–456, 2004.

[55] P W Bearman. Investigation of the flow behind a two-dimensional model with a blunt trailing edge and fitted with splitter plates. *J. Fluid Mech.*, 21(02):241–255, 1965.

[56] Anatol Roshko. On the wake and drag of bluff bodies. *J. Aeronaut. Sci.*, 22(2):124–132, 1955.

[57] Jong-Yeon Hwang, Kyung-Soo Yang, and Seung-Han Sun. Reduction of flow-induced forces on a circular cylinder using a detached splitter plate. *Phys. Fluids*, 15(8):2433–2436, 2003.

[58] Huseyin Akilli, Cuma Karakus, Atakan Akar, Besir Sahin, and N. Filiz Tumen. Control of Vortex Shedding of Circular Cylinder in Shallow Water Flow Using an Attached Splitter Plate. *J. Fluids Eng.*, 130(4):041401, 2008.

[59] E. Achenbach. The effects of surface roughness and tunnel blockage on the flow past spheres. *J. Fluid Mech*, 65(1):113–125, 1974.

[60] O Güven, C Farell, and V C Patel. Surface-roughness effects on the mean flow past circular cylinders. *J. Fluid Mech.*, 98(04):673–701, 1980.

[61] J. Choi. *Mechanism of drag reduction by surface modification on a sphere: Dimples, roughness and trip wire.* Phd, Seoul Natl. Univ., Korea, 2006.

[62] JoséLuis Duarte Ribeiro. Effects of surface roughness on the two-dimensional flow past circular cylinders I: mean forces and pressures. *J. Wing Eng. Ind. Aerod.*, 37(3):299–309, 1991.

[63] Y. Nakamura and Y. Tomonari. The effects of surface roughness on the flow past circular cylinders at high Reynolds numbers. *J. Fluid Mech.*, 123:363–378, 1982.

[64] T Hojo. Control of flow around a circular cylinder using a patterned surface. *WIT Trans. Model. Sim.*, 59:245–256, 2015.

[65] John C. Lin. Review of research on low-profile vortex generators to control boundary-layer separation. *Prog. Aerosp. Sci.*, 38(4-5):389–420, 2002.

[66] Harold D Taylor. The elimination of diffuser separation by vortex generators. *United Aircraft Corporation, East Hartford, CT, Technical Report No*, 4012:3, 1947.

[67] Jin Choi, Woo Pyung Jeon, and Haecheon Choi. Mechanism of drag reduction by dimples on a sphere. *Phys. Fluids*, 18(4), 2006.

[68] P.W. Bearman and J.K. Harvey. Control of circular cylinder flow by the use of dimples. *AIAA J.*, 31(10):1753–1756, oct 1993.

[69] William Taylor. Golf-ball., 1908.

[70] John M Davies. The aerodynamics of golf balls. *J. App. Phys.*, 20(9):821–828, 1949.

[71] Rabindra D Mehta. Aerodynamics of sports balls. *Annu. Rev. Fluid Mech.*, 17(1):151–189, 1985.

[72] Firoz Alam, Tom Steiner, Harun Chowdhury, Hazim Moria, Iftekhar Khan, Fayez Aldawi, and Aleksandar Subic. A study of golf ball aerodynamic drag. *Procedia Engineer.*, 13:226–231, 2011.

[73] Elmar Achenbach. Experiments on the flow past spheres at very high Reynolds numbers. *J. Fluid Mech.*, 54(03):565, 1972.

[74] Katsumi Aoki, Koji Muto, and Hiroo Okanaga. Mechanism of Drag Reduction by Dimple Structures on a Sphere. *JFST*, 7(1):1–10, 2012.

[75] D. Terwagne, M. Brojan, and P.M. Reis. Smart Morphable Surfaces for Aerodynamic Drag Control. *Adv. Mater.*, 26(38):6659–6659, oct 2014.

[76] U. Butt and C. Egbers. Aerodynamic Characteristics of Flow over Circular Cylinders with Patterned Surface. *IJMMM*, 1(2):121–125, 2013.

[77] Bo Zhou, Xikun Wang, Wei Guo, Wie Min Gho, and Soon Keat Tan. Control of flow past a dimpled circular cylinder. *Exp. Therm. Fluid Sci.*, 69:19–26, 2015.

[78] S. Talley, G. Iaccarino, G. Mungal, and N. Mansour. An experimental and computational investigation of flow past cacti. *Center for Turbulence Research Annual Research Briefs*, pages 51 – 63, 2001.

[79] P. Babu and K. Mahesh. Aerodynamic loads on cactus-shaped cylinders at low reynolds numbers. *Phys. Fluids*, 20(3):035112, 2008.

[80] J.E. Abboud, W.S. Karaki, and G.F. Oweis. Particle Image Velocimetry Measurements in the Wake of a Cactus-Shaped Cylinder. *J. Fluid Eng.*, 133(9):094502, 2011.

[81] A.M. El-Makdah and G.F. Oweis. The flow past a cactus-inspired grooved cylinder. *Exp. Fluids*, 54(2):1464, 2013.

[82] T. Kimura and M. Tsutahara. Fluid dynamic effects of grooves on circular cylinder surface. *AIAA J.*, 29(12):2062–2068, 1991.

[83] Y. Yamagishi and M. Oki. Effect of Groove Shape on Flow Characteristics around a Circular Cylinder with Grooves. *J. Vis.*, 7(3):209–216, 2004.

[84] Y. Yamagishi and M. Oki. Effect of the number of grooves on flow characteristics around a circular cylinder with triangular grooves. *J. Vis.*, 8(1):57–64, 2005.

[85] S.J. Quintavalla, A.J. Angilella, and A.J. Smits. Drag reduction on grooved cylinders in the critical Reynolds number regime. *Exp. Therm. Fluid Sci.*, 48:15–18, 2013.

[86] H.C. Bulk. The maximum daily wind gust speed climatology at Sky Harbor Airport, Phoenix, Arizona. *Laboratory of Climatology, Arizona State Univ. Report 18,*. 1984.

[87] Wikimedia Commons/Public Domain: https://commons.wikimedia.org/wiki/File:Saguaro3.jpg.

[88] Hans-Joachim Bungartz and Michael Schäfer. *Fluid-structure interaction: modelling, simulation, optimisation*, volume 53. Springer Science & Business Media, 2006.

[89] Price S. J. Païdoussis, M. P. and E. de Langre. *Fluid-Structure Interactions: Cross-Flow-Induced Instabilities.* Cambridge University Press, 1 edition, 2014.

[90] DS Barrett, MS Triantafyllou, DKP Yue, MA Grosenbaugh, and MJ Wolfgang. Drag reduction in fish-like locomotion. *J. Fluid Mech.*, 392:183–212, 1999.

[91] Y. Watanabe, S. Suzuki, M. Sugihara, and Y. Sueoka. An Experimental Study of Paper Flutter. *J. Fluids. Struct.*, 16(4):529–542, 2002.

[92] R. H. Scanlan and J. J. Tomko. Airfoil and bridge deck flutter derivative. *J. Eng. Mech*, 97:1717–1737, 1971.

[93] R. H. Scanlan. The action of flexible bridges under wind, i: Flutter theory. *J. Sound Vib.*, 60:187–199, 1977.

[94] R. H. Scanlan. On the state of stability considerations for suspended bridges under wind. *Proc. IUTAM-IAHR Symposium, Karlsruhe, Germany, Paper FI*, pages 595–618, 1979.

[95] F. Bleich. Lessons in bridge design taught by aerodynamic studies. *Proc. Am. Soc. Civil Eng.*, 16:1269–1314, 1948.

[96] Y. Rocard. *Dynamic Instability.* Crossby Lockwood, London, 1 edition, 1957.

[97] Elvin N. Akaydin, H. D. and Y. Andreopoulos. Flapping States of a Flag in an Inviscid Fluid: Bistability and the Transition to Chaos. *J. Intell. Mater. Syst. Struct.*, 21(13):1263–1278, 2010.

[98] S. C.; Mann B. P.; Dunnmon, J. A.; Stanton and E. H. Dowell. Power extraction from aeroelastic limit cycles. *J. Fluid Struc.*, 27:1182–1198, 2011.

[99] L. Zhao and Y. Yang. Enhanced aeroelastic energy harvesting with a beam stiffener. *Smart Mater. Struct.*, 24(3):032001, 2015.

[100] Yongsam Kim and Charles S Peskin. 2-D parachute simulation by the immersed boundary method. *SIAM J. Sci. Comput.*, 28(6):2294–2312, 2006.

[101] Christophe Eloy, Claire Souilliez, and Lionel Schouveiler. Flutter of a rectangular plate. *J. Fluids Struct.*, 23(6):904–919, 2007.

[102] Christophe Eloy, Romain Lagrange, Claire Souilliez, and Lionel Schouveiler. Aeroelastic instability of cantilevered flexible plates in uniform flow. *J. Fluid Mech.*, 611:97–106, 2008.

[103] Sadatoshi Taneda. Waving motions of flags. *J. Phys. Soc. Jpn.*, 24(2):392–401, 1968.

[104] W. Shyy, H. Aono, S. K. Chimakurthi, P. Trizila, C. K. Kang, C. E. S. Cesnik, and H. Liu. Recent progress in flapping wing aerodynamics and aeroelasticity. *Prog. Aerosp. Sci.*, 26(7):284–327, 2010.

[105] E. H. Dowell and K. C. Hall. Modeling of fluid-structure interaction. *Annu. Rev. Fluid Mech.*, 33:445–490, 2001.

[106] Reinhall P. G. Eberle, A. L. and Daniel T. L. Fluid-structure interaction in compliant insect wings. *Bioinspir. Biomim.*, 9:025005, 2014.

[107] Emmanuel De Langre, Alvaro Gutierrez, and Julia Cossé. On the scaling of drag reduction by reconfiguration in plants. *C. R. Mecanique*, 340(1-2):35–40, 2012.

[108] Steven Vogel. Drag and reconfiguration of broad leaves in high winds. *J. Exp. Bot.*, 40(8):941–948, 1989.

[109] F. Gosselin, E. de Langre, and B. Machado-Almeida. Drag reduction of flexible plates by reconfiguration. *J. Fluid Mech.*, 650:319–341, 2010.

[110] Peter Buchak, Christophe Eloy, and Pedro M Reis. The clapping book: wind-driven oscillations in a stack of elastic sheets. *Phys. Rev. Lett.*, 105(19):194301, 2010.

[111] Eloy Christophe Schouveiler, Lionel and Patrice Le Gal. Flow-induced vibrations of high mass ratio flexible filaments freely hanging in a flow. *Phys. Fluids*, 17(4):047104, apr 2005.

[112] S. Alben and M. J. Shelley. Flapping States of a Flag in an Inviscid Fluid: Bistability and the Transition to Chaos. *Phys. Rev. Lett.*, 100(7):074301, feb 2008.

[113] M. J. Lighthill. Note on the swimming of slender fish. *J. Fluid Mech.*, 9:305, 1960.

[114] Silas Alben, Michael Shelley, and Jun Zhang. Drag reduction through self-similar bending of a flexible body. *Nature*, 420(6915):479–481, 2002.

[115] Silas Alben, Michael Shelley, and Jun Zhang. How flexibility induces streamlining in a two-dimensional flow. *Phys. Fluids*, 16(5):1694–1713, 2004.

[116] Antonio Filippone. On the Flutter and Drag Forces on Flexible Rectangular Canopies in Normal Flow. *J. Fluids Eng.*, 130(6):061203, 2008.

[117] Michael J. Shelley and Jun Zhang. Flapping and Bending Bodies Interacting with Fluid Flows. *Annu. Rev. Fluid Mech.*, 43(September):449–465, 2011.

[118] Michael Shelley, Nicolas Vandenberghe, and Jun Zhang. Heavy flags undergo spontaneous oscillations in flowing water. *Phys. Rev. Lett.*, 94(9), 2005.

[119] E. M. Laws and Livesey J. L. Flow through screens. *Ann. Rev. Fluid Mech.*, 10:247– 266, 1978.

[120] R. H. Blockley. *M.Sc. Thesis.* University of London, 1 edition, 1968.

[121] IP Castro. Wake characteristics of two-dimensional perforated plates normal to an air-stream. *J. Fluid Mech.*, 46(03):599–609, 1971.

[122] JMR Graham. Turbulent flow past a porous plate. *J. Fluid Mech.*, 73(03):565–591, 1976.

[123] J-K Koo and David F James. Fluid flow around and through a screen. *J. Fluid Mech.*, 60(03):513–538, 1973.

[124] R. A. Pinker and M. V. Herbert. Pressure loss associated with compressible flow through square-mesh wire gauzes. *J. Mech. Eng. Sci.*, 9:11–23, 1978.

[125] A. J. Reynolds. Flow deflection by gauze screens. *J. Mech. Eng. Sci.*, 11:290–294, 1969.

[126] G.I. Taylor. Air resistance of a flat plate of very porous material. *R&M of the Aeronautical Research Council*, (2236), 1944.

[127] G.I. Taylor and R. M. Davies. The aerodynamics of porous sheets. *R&M of the Aeronautical Research Council*, (2237), 1944.

[128] C. Hodge. *All about Saguaros.* Arizona Highways, Phoenix, 1991.

[129] L. Benson. *The Cacti of Arizona.* University of Arizona Press, Tucson, 1981.

[130] G.N. Geller and P.S. Nobel. Cactus ribs: influence on PAR interception and CO2 uptake. *Photosynthetica*, 18(4):482–494, 1984.

[131] S. Govindjee and J. Simo. A Micro-Mechanically Based Continuum Damage Model for Carbon Black-Filled Rubbers Incorporating Mullins' Effect. *J. Mech. Phys. Solids*, 39(1):87–112, 1991.

[132] F. López Jiménez and S. Pellegrino. Folding of fiber composites with a hyperelastic matrix. *International Journal of Solids and Structures*, 49(3-4):395–407, 2012.

[133] J. Anthoine, D. Olivari, and D. Portugaels. Wind-tunnel blockage effect on drag coefficient of circular cylinders. *Wind Struct.*, 12(6):541–551, nov 2009.

[134] E.C. Maskell. A Theory of the Blockage Effects on Bluff Bodies and Stalled Wings in a Closed Wind Tunnel. *Aeronautical Research Council (Great Britain), R&M Report No. 3400*, 1965.

[135] The MathWorks, Inc. *Matlab Global Optimization Toolbox User's Guide*, 3.4.1 edition, 2016.

[136] M. Guttag and M.C. Boyce. Locally and Dynamically Controllable Surface Topography Through the Use of Particle-Enhanced Soft Composites. *Adv. Funct. Mater.*, 25(24):3641–3647, 2015.

[137] H. Meng and G. Li. A review of stimuli-responsive shape memory polymer composites. *Polymer*, 54(9):2199–2221, 2013.

[138] Y. Liu, H. Lv, X. Lan, J. Leng, and S. Du. Review of electro-active shape-memory polymer composite. *Compos. Sci. Techol.*, 69(13):2064–2068, 2009.

[139] Brian Hill. The Evolution of Golf Balls, 2008.

[140] Francis Moran, Heiner Gillmeister, and John Ross Goodner. Golf, 2017.

[141] SFIA. Wholesale Sales of Golf Equipment in The U.S. from 2007 to 2016 (in Million U.S. Dollars)*, 2017.

[142] T.C. Hodges and K.A. Seffen. Drag Manipulation Through Reversible Surface Dimpling and Ruffling. Technical report, University of Cambridge Department of Engineering, Cambridge, UK, 2015.

[143] Z Cao, P Wang, W Gao, L Tao, J W Suk, R S Ruoff, D Akinwande, R Huang, and K M Liechti. A blister test for interfacial adhesion of large-scale transferred graphene. *Carbon*, 69(Supplement C):390–400, 2014.

[144] Frédérick P Gosselin and Emmanuel De Langre. Drag reduction by reconfiguration of a poroelastic system. *J. Fluids Struct.*, 27(7):1111–1123, 2011.

[145] Damiano Natali, Jan O Pralits, Andrea Mazzino, and Shervin Bagheri. Stabilizing effect of porosity on a flapping filament. *J. Fluids Struct.*, 61:362–375, 2016.

[146] B. Audoly and Y. Pomeau. *Elasticity and Geometry.* Oxford University Press, 1 edition, 2010.

[147] L. D. Landau, L. P. Pitaevskii, A. M. Kosevich, and E. M. Lifshitz. *Theory of Elasticity, Third Edition: Volume 7 (Course of Theoretical Physics).* Pergamon Press, 3 edition, 1986.

[148] Daegyoum Kim, Julia Coss, Cecilia Huertas Cerdeira, and Morteza Gharib. Flapping dynamics of an inverted flag. *J. Fluid Mech.*, 736, 2013.